Dissertation

Pyramid Dimension of Histological Images of the Heart

submitted by

Dipl.-Ing. Dr.techn.

Michael

MAYRHOFER-REINHARTSHUBER

for the Academic Degree of

Doctor of Medical Science

Dr.scient.med.

at the

Medical University of Graz

Institute of Biophysics

under the supervision of

Ao.Univ.-Prof. Mag. Dr.rer.nat. Helmut AHAMMER

Graz, August 2015

Eidesstattliche Erklärung

Ich erkläre ehrenwörtlich, dass ich die vorliegende Arbeit selbstständig angefertigt und abgefasst, und jene Personen und Institutionen, die am Zustandekommen der Forschungsdaten beteiligt waren, namentlich genannt habe. Andere als die angegebenen Quellen habe ich nicht verwendet und die den benutzten Quellen wörtlich oder inhaltlich entnommenen Stellen habe ich als solche kenntlich gemacht. Die Arbeit an der Dissertation und daraus entstandener Publikationen wurde gemäß den Regeln der „Good Scientific Practice“ durchgeführt.

Statutory Declaration

I hereby declare that this thesis is my own original work and that I have fully acknowledged by name all of those individuals and organisations that have contributed to the research for this thesis. Due acknowledgement has been made in the text to all other material used. Throughout this thesis and in all related publications I followed the guidelines of ‘Good Scientific Practice’.

Graz, _____ _____

Date Signature

Abstract

Myocardial fibrosis is associated with cardiac arrhythmias, its texture influences their incidence. An automated classification system could act as a supporting system for pathologists and help them diagnosing different fibrotic patterns. For that reason an image analysis method for an automated classification of different types of fibrosis in histological images is highly desirable. Fractal analysis quantifies the morphology in images, hence it is a promising approach for the development of such a system. Since medical, especially histological images often have very high resolutions, it is of high relevance to improve existing fractal methods and to develop new approaches for providing fast and accurate results based on these large amounts of data.

For fractal dimension estimation of grey value images, three new pyramidal approaches were developed, namely the *Pyramid Triangular Prism Method* (PTPM), the *Pyramid Gradient Method* (PGM), and the *Pyramid Differences Method* (PDM). By using artificially created images the new methods were compared to five standard, non-pyramidal approaches. All new pyramidal methods yielded reasonable values for the fractal dimension D in rather fast computational times. Best results were obtained with the PDM, having a high agreement with theoretical D values and fastest computational times.

Based on the new methods, classification algorithms were developed to automatically assign images to five different types of fibrosis. Tests on different image sets showed that the proposed methods resulted in up to 73% correctly (in accordance with human experts) classified images. Although the accordance between the experts was better (up to 90%), utilizing fractal analysis for classification of myocardial fibrosis in digital pathology is definitely a promising approach, should be considered in subsequent developments and may support pathologists in the future.

Kurzfassung

Myokardiale Fibrose und deren unterschiedliche Struktur wird mit Auftreten und Verlauf von Herzarrhythmien in Verbindung gebracht. Durch eine automatische Klassifizierung von unterschiedlichen Typen von Fibrose könnten Pathologen wertvolle Unterstützung zur Befundung des von ihnen untersuchten Gewebes erhalten. Die fraktale Analyse stellt einen vielversprechenden Ansatz in diese Richtung dar, da es mit ihr möglich ist, die in Bildern auftretenden Muster zu quantifizieren. Medizinische Bilder, insbesondere digitalisierte histologische Schnitte, weisen meist eine sehr hohe Auflösung auf. Um diese großen Mengen an Daten in kurzer Zeit möglichst exakt auszuwerten, sind Verbesserungen und Neuentwicklungen fraktaler Methoden notwendig.
Zur Berechnung der fraktalen Dimension D von Grauwertbildern wurden drei neue fraktale Methoden entwickelt, die *Pyramid Triangular Prism Method* (PTPM), die *Pyramid Gradient Method* (PGM) und die *Pyramid Differences Method* (PDM). Zusammen mit fünf weiteren Standardmethoden wurden diese Pyramidenmethoden auf künstlich erzeugte Bilder mit bekannter fraktaler Dimension angewandt. Die Resultate der neu entwickelten Methoden befinden sich im Bereich der besten Ergebnisse der getesteten Standardmethoden. Von den neu entwickelten Methoden zeigte die PDM die beste Übereinstimmung mit den theoretischen Werten und erwies sich als schnellste aller getesteten Methoden.
Eine darauf aufbauende Methode zur automatischen Klassifizierung von fünf unterschiedlichen Typen von Fibrose resultierte in bis zu 73% korrekt, d.h. in Übereinstimmung mit Experten klassifizierten Bildern. Obwohl die Übereinstimmung zwischen den Experten untereinander bis zu 90% betrug, kann daraus geschlossen werden, dass die fraktale Analyse einen vielversprechenden Ansatz für die digitale Pathologie im Bereich der myokardialen Fibrose darstellt und auch bei zukünftigen Anwendungen eine Rolle spielen sollte.

Contents

Nomenclature

Abbreviations

ANOVA	Analysis of Variance
BCM	Box-Counting Method
DBCM	Differential Box-Counting Method
DLA	Diffusion-Limited Aggregate
FFT	Fast Fourier Transformation
HM	Higuchi Method (2D)
IFR	Inverse Fourier Reconstruction
LSD	Least Significant Difference
MD	Midpoint Displacement
PDM	Pyramid Differences Method
PGM	Pyramid Gradient Method
PM	Pyramid Method
PTPM	Pyramid Triangular Prism Method
RMD	Random Midpoint Displacement
SD	Standard Deviation
SRA	Successive Random Addition
S-W	Shapiro-Wilk
TPM	Triangular Prsim Method

Symbols

D	Fractal Dimension
D_{BC}	Box-Counting Dimension
$D_{\mathrm{Blanket}}^{\mathrm{Peleg}}$	Minkowski Blanket Dimension (Peleg)
$D_{\mathrm{Blanket}}^{\mathrm{Dubuc}}$	Minkowski Blanket Dimension (Dubuc)

$D_{\text{creation,MD}}$	Theoretical Fractal Dimension, Midpoint Displacement Generator
$D_{\text{creation,FFT}}$	Theoretical Fractal Dimension, FFT Generator
$D_{\text{creation,Takagi}}$	Theoretical Fractal Dimension, Takagi Surface
D_{DBC}	Differential Box-Counting Dimension
$D_{\text{DBC}}^{\text{improved}}$	Improved Differential Box-Counting Dimension
D_{F}	Fourier Dimension
D_{HB}	Hausdorff-Besicovitch Dimension
D_{H}	Higuchi Dimension
D_{P}	Pyramid Dimension
D_{PD}	Pyramid Differences Dimension
$D_{\text{PD}}^{\text{bicubic}}$	Pyramid Differences Dimension, bicubic interpolation
$D_{\text{PD}}^{\text{bilinear}}$	Pyramid Differences Dimension, bilinear interpolation
$D_{\text{PD}}^{\text{nearest}}$	Pyramid Differences Dimension, nearest neighbour interpolation
D_{PG}	Pyramid Gradient Dimension
$D_{\text{PG}}^{\text{simple}}$	Pyramid Gradient Dimension, simple kernel
$D_{\text{PG}}^{\text{simple,bicubic}}$	Pyramid Gradient Dimension, simple kernel, bicubic interpolation
$D_{\text{PG}}^{\text{simple,bilinear}}$	Pyramid Gradient Dimension, simple kernel, bilinear interpolation
$D_{\text{PG}}^{\text{simple,nearest}}$	Pyramid Gradient Dimension, simple kernel, nearest neighbour interpolation
$D_{\text{PG}}^{\text{sobel}}$	Pyramid Gradient Dimension, Sobel kernel
$D_{\text{PG}}^{\text{sobel,bicubic}}$	Pyramid Gradient Dimension, Sobel kernel, bicubic interpolation
$D_{\text{PG}}^{\text{sobel,bilinear}}$	Pyramid Gradient Dimension, Sobel kernel, bilinear interpolation
$D_{\text{PG}}^{\text{sobel,nearest}}$	Pyramid Gradient Dimension, Sobel kernel, nearest neighbour interpolation
D_{PTP}	Pyramid Triangular Prism Dimension
$D_{\text{PTP}}^{\text{bicubic}}$	Pyramid Triangular Prism Dimension, bicubic interpolation
$D_{\text{PTP}}^{\text{bilinear}}$	Pyramid Triangular Prism Dimension, bilinear interpolation
$D_{\text{PTP}}^{\text{nearest}}$	Pyramid Triangular Prism Dimension, nearest neighbour interpolation
D_{SS}	Self-Similarity Dimension
D_{TP}	Triangular Prism Dimension
E	Embedding Dimension
$\mathbb{N}$	natural numbers (positive integers)
$\mathbb{N}_0$	natural numbers including 0 (non-negative integers)
T	Topological Dimension

List of Figures

List of Tables

1. Introduction

In medicine images and imaging techniques have always played an important role to distinguish between healthy and pathological cases.

Fractal methods use non-Euclidean geometry and have successively been applied to medical images, solving many medical image diagnoses issues[1]. Commonly, an algorithm called *Box-Counting Method* (BCM) is applied to determine relevant diagnostic parameters. In 2012 our group showed that there exists also a pyramidal approach for calculating the Box-Counting Dimension of binary images[2]. For artificially created images the results of this so-called *Pyramid Method* (PM) are identical to results gained with the Box-Counting algorithm. The outstanding advantage of this new method is its much faster computational time with equal high quality of the results. Therefore, this new approach is an important step towards one main aim of digital pathology: (In-vivo) real-time tissue analysis.

1.1. Motivation

Several groups at the Institute of Biophysics, Medical University of Graz study the excitation spread in the heart. The experimental group around Ernst Hofer has its main focus on electrical measurements and a characterization of the region around the inferior right atrial isthmus[3–5]. A modeling group around Gernot Plank creates different types of 2D- and 3D-models and helps to understand and interpret the measured data[6,7]. Further research projects should connect the influences of different types and amounts of fibrosis with electrophysiological parameters. This is of recent interest since fibrosis is associated with cardiac arrhythmias[8] and the texture of fibrosis influences their incidence[8,9]. Particularly, the investigation of local differences at microscopic scales would be of high interest for the scientific community. Assessing the vulnerability for

arrhythmias could be possible with a local detection and characterization of fibrosis in the heart. For that reason an image analysis method for an automated classification of different types of fibrosis in histological images is highly desirable. Furthermore, an automated classification system could act as a supporting system for pathologists and help them diagnosing different fibrotic patterns. Since fractal analysis quantifies the morphology in images, it is a promising approach for the development of such a system.

Besides the application of fractal methods it is of high relevance to improve existing methods and to develop new approaches to tackle new challenges in image analysis. The most important reason for the need of new fractal algorithms is the fact, that images, especially in medicine, often have a very high resolution. On one hand this improves the gainable output of image analysis but on the other hand large amounts of data have to be handled by the implemented methods.

For the goal of real-time tissue analysis the development of the binary PM was an important step. However, histological images are usually colour or grey value images. Hence it is necessary to find an equivalent fast and reliable method suitable for the task of classifying myocardial fibrosis. As the development of the binary PM showed and already an early work on fractals[10] suggested, a pyramidal approach could act as an efficient implementation of such a multiscale method.

1.2. Aim of this Work

The main aims of this work are the finding of the most qualified and fastest methods for fractal characterization of grey value images and their application on high-resolution histological images showing myocardial fibrosis.

Based on the results obtained with the binary Pyramid Method it is expected that also for grey value images pyramidal approaches for determining fractal properties in digital images fast and reliably exist. The analysis of images having a high pixel count should be feasible with significantly faster computational times.

Hypothesis

1. Fractal dimensions of grey value images can be reliably estimated by a pyramidal approach. This pyramidal approach has shorter computational times than standard approaches.
2. The estimated fractal dimension of histological images can be used as a parameter for a classification of different types of myocardial fibrosis.

1.3. Organisation of this Thesis

This thesis is organized in two main parts.

Part I aims to verify the first hypothesis of this thesis, i.e. to prove that fractal dimensions of grey value images can be reliably estimated by a fast pyramidal approach. Chapter 2 gives a brief introduction into the field of digital images and digital image processing. The theoretical background of fractals is presented in chapter 3, including the definition of the Hausdorff-Besicovitch and the Box-Counting Dimension. In chapter 4, five well-established algorithms for fractal dimension estimation are presented together with three new pyramidal methods. Chapter 5 deals with the generation of artificially created fractal images used for this work. The setup for the chosen empirical study, the results and the conclusion are presented in the chapters 6, 7, and 8.

In part II the application of image analysis, especially fractal methods to histological images showing myocardial fibrosis is presented. It aims to verify the second hypothesis of this thesis, i.e. to prove that the fractal dimension of histological images can be used as a parameter for a classification of different types of myocardial fibrosis. Chapter 9 shows the medical background together with techniques for the imaging of myocardial fibrosis. The histological image sets to which the fractal analysis methods were applied are described in chapter 10. In chapter 11 the methods for an automated classification of different types of fibrosis are outlined together with the experimental setup for a comparison with an inter-observer study. The obtained results as well as the conclusion are presented in chapters 12 and 13.

In the end, this thesis is concluded in chapter 14 and a brief outlook of possible future work is given in chapter 15.

Part I.

Fractal Image Analysis

2. Digital Image Analysis

This chapter gives a brief introduction into image acquisition and describes compositions (pixel values, colour spaces, file formats) of digital images. Details can be found in fundamental image analysis handbooks, e.g. Burger and Burge[11].

2.1. Image Acquisition

As a prerequisite for all types of image analysis, the image to be analysed has to be recorded. Most methods for image recording are variations of classical optical cameras, i.e. pinhole or lens cameras. In pathology often a *whole-slide imaging technique* (e.g. a whole slide scanner) is used to scan histological sections at high resolutions. Usually the so-called *perspective transformation* is included in this process, i.e. a 3D object or scene is transformed to 2D coordinates on the *image plane*. The projected image on the camera's image plane is a continuous, time-dependent distribution of energy originating from the incoming electromagnetic wave (light).

Before an image can be analysed, it has to be brought into an adequate format. When nowadays computer-assisted algorithms are included, a *digital image format* is mandatory. Hence a *digital snapshot* of the projection on the image plane has to be taken. This procedure consists of three main steps:

1. **spatial sampling** of the light distribution to obtain a *spatially discrete function*
2. **temporal sampling** of the discrete function to create a single, temporally constant image
3. **quantization** of the resulting values to a finite set which is representable with a computer

Spatial sampling is dictated by the geometry of the acquisition device, usually sensor elements with rectangular shapes are used, but also other shapes (e.g. hexagonal or circular) exist. Temporal sampling is achieved by measuring the energy of the incident light at regular intervals, e.g. with a CCD (charge-coupled device) chip in a digital camera. The obtained analog values are quantized (e.g. with an analog-to-digital converter) by using a defined range of values (usually integer) and stored as a *digital image* for further usage. The extent of this scale is chosen with having in mind the accuracy necessary for further processing.

2.2. Digital Images

As an outcome of the image acquisition described above, a standard digital image has the form of an ordered, two-dimensional matrix $I(x, y)$ of integer values. $(x, y) \in \mathbb{N} \times \mathbb{N}$ are the coordinates of the pixel values p, $p \in \mathbb{P}$ where $\mathbb{P}$ is the range of pixel values. Mathematically, a digital image I is a mapping

$$I : \mathbb{N} \times \mathbb{N} \to \mathbb{P}, (x, y) \mapsto p. \tag{2.1}$$

Due to the finite size of images, x and y have upper borders, where the maximum value of x is denoted as *image width*, the maximum value of y as *image height*. Attention has to be paid to the orientation of the y-coordinate: The origin of an image is in the upper left corner, i.e. in contrast to standard mathematical conventions the y-coordinate runs from top to bottom[11].

2.2.1. Pixel Values

Pixel values of digital images are typically binary words of length k. Hence a pixel can possess 2^k different values. k is also referred to as *bit depth* of an image. The following image types are common in digital image analysis[11]:

- **Binary Images** are a special case of intensity images with $k = 1$. Each pixel can have a value of 0 (black) and 1 (white).
- **Intensity or Greyscale (Grey Value) Images** have typical bit depths of $k = 8 - 16$ bits, hence from 256 up to 65536 different values for the intensity of each pixel.

- **Colour Images** have typical bit depths of 24-42 bits. Usually three (RGB = red, green, blue) or four (CMYK = cyan, magenta, yellow, black) *channels* are used for each pixel, representing intensity values for the different channels of the underlying colour model (see section 2.2.2).

In image analysis, the starting point is mostly a colour image, which is often converted into a grey value image or a binary image (e.g. by using segmentation algorithms) before further analysis. The conversion of a colour image to a grey value image can be done in different ways. The most common way is to use the *luminance*, e.g. for an RGB image using the mean of the three colour values as a new single grey value for each pixel. However, the human perception is different for red, green and blue. So another way is to use a weighted sum of the colour components as the new grey value Y:

$$Y = w_{\mathrm{R}}R + w_{\mathrm{G}}G + w_{\mathrm{B}}B \tag{2.2}$$

The most popular weights used have their origin in television and are $w_{\mathrm{R}} = 0.299$, $w_{\mathrm{G}} = 0.587$ and $w_{\mathrm{B}} = 0.114$, for digital colour encoding $w_{\mathrm{R}} = 0.2125$, $w_{\mathrm{G}} = 0.7154$ and $w_{\mathrm{B}} = 0.072$ are recommended[11].

2.2.2. Colour Model

An abstract mathematical *colour model* describes how colours can be represented (e.g. by tuples of numbers). Together with a mapping function it gives a *colour space*, which describes a specific organization of colours and is used for reproducible representations of colours. Due to its occurrence in most imaging devices of electronic systems, the most popular is the *RGB* model, in which the colours red (R), green (G) and blue (B) are added together in variable amounts to obtain different colours. A colour space of high importance is *CIE L*a*b** (*CIE LAB*). It is based on all colours visible by the human eye and acts as a device-independent reference model. CIE L*a*b* describes colours based on lightness (L*), values for nuances between green and magenta (a*), and between blue and yellow (b*).

2.2.3. Image File Formats

In image analysis, images are usually considered as two-dimensional arrays, which are ready to be accessed by a program. They are handled in digital form, typically as files,

which are essential for storing, archiving and exchanging. A wide range of file formats for images exist and usually the developer or user decides which one is the best for a specific application.

Throughout this work only *raster images* were used, which consist of pixel values arranged in a regular matrix, in which the row and column of the pixel value give the pixel coordinates. Raster images are in contrast to *vector images*, which use data of geometric objects to store information and are only rasterized once they need to be displayed[11].

2.2.3.1. JPEG File Interchange Format (JFIF)

Although often the term *JPEG file* is used, JPEG (Joint Photographic Experts Group)[12] is actually just a compression method for image data. In most of the cases the term *JPEG file* refers to the JPEG File Interchange Format (JFIF), which was developed by Eric Hamilton and the Independent JPEG Group (IJG)[13]. In the most important part of the JPEG codec, the image is split into blocks of 8×8 pixels. Thereafter, the *discrete cosine* transformation is used to convert the image to frequency space, in which the 64 spectral coefficients of each block are quantized by using a pre-defined table. The size of this table determines the ratio of compression. Disadvantages of this lossy compression are the artifacts caused by the pixel blocks, the presentation of abrupt changes within the image (e.g. in images showing line art) and its limitation to 8-bit (per channel) images[11].

2.2.3.2. JPEG-2000

To get rid of the known disadvantages of the traditional JPEG codec, as an improvement the JPEG-2000 codec was established. The most valuable innovations are the use of 64×64 pixel blocks instead of 8×8 pixel blocks and the usage of the *wavelet* transform instead of the discrete cosine transform[11]. The digital slide scanners of *Aperio*, which were used to record histological sections for this work, are able to save the scans with this JPEG-2000 compression (see *SVS-Files* below).

2.2.3.3. Tagged Image File Format (TIFF)

An often used file format during the work for this project was the Tagged Image File Format (TIFF), which is known to be a very flexible, widely used format. A range of true colour, indexed, grayscale images or even more specialized image types (e.g. images with floating-point elements) are supported by this format. Different colour spaces and compression methods as e.g. JPEG, LZW (the lossless Lempel-Ziv-Welch algorithm) or others can be used within this format. A number of variations of an image (e.g. different sizes) can be stored in a single TIFF-file. The contained images are described by a header and specific tags within this file[11].

2.2.3.4. SVS-Files (Aperio)

The proprietary SVS file format was created and is used by the digital pathology company *Aperio*. Their products, e.g. the whole-slide-imaging scanner at the Institute of Pathology in Graz (see section 10.1.2), create single-file pyramidal tiled TIFF files, with non-standard metadata and variable compression. Typically Aperios *type code 2* or *type code 3* are used, which create TIFF files with JPEG compression or JPEG-2000 compression, respectively.

Since a variety of file formats from different companies exist, the *OpenSlide* project[14] provides a C library (including Python and Java bindings, for Matlab see Forsberg[15]) to make these formats easily accessible also from non-proprietary software.

2.3. Digital Image Processing

2.3.1. Histogram Modification

Histograms of images describe, how many times each pixel intensity value occur, i.e. they are frequency distributions of the intensity values of images. From a histogram, statistical information (contrast, dynamic range, etc.) but no spatial information can be extracted. Furthermore, histograms can be systematically modified to change the appearance of images, to improve the quality, and to make it easier to analyse. For instance, *histogram equalization* can be used to obtain images having the same intensity distributions. This procedure is an important preliminary step, when different images

are compared. A variety of different, more advanced algorithm for histogram equalization exist, e.g. *adaptive histogram equalization* to improve local contrast or *contrast limited adaptive histogram equalization* to reduce overamplification of noise. Other techniques exist, e.g. *histogram normalization* is used to change the range of pixel intensity values[11].

2.3.2. Interpolation

Several geometric image operations use geometric transformations to link the coordinates of source and destination image points. Pyramidal approaches for fractal dimension estimation use such operations, especially scaling methods, to create the required image pyramids. Usually the destination image points do not lie exactly at a source image point location or at integer coordinates. For instance, when a grey value image (100×100 grey values) with an original size of 100×100 pixels is reduced by the factor of 2, there are grey values also at positions halfway in between the integer pixel positions (100×100 grey values on a $[0, 0.5, 1, 1.5, ..., 49.5] \times [0, 0.5, 1, 1.5, ..., 49.5]$ grid). But the resulting image should have a size of 50×50 pixels. Different procedures exist to obtain the desired size without neglecting too much information. Typically not only single but also the neighbouring pixels of the source image are included in the calculation of the values of the new image. This procedure is called *image resampling* or *interpolation*. The resulting value for the new image point is obtained by a function of the pixels in its neighbourhood. From a mathematical point of view the ideal resampling function has to include an infinite number of surrounding image points. However, in practice there are three common, non-ideal but useful and hence popular techniques:

- *Nearest-neighbour resampling* or *zero-order interpolation* is the simplest and fastest method. It uses the value of the nearest lattice point for the new pixel value.
- *Bilinear interpolation* or *first-order interpolation* uses the four closest points to interpolate linearly (first rows, then columns) between them.
- *Bicubic interpolation* uses a 4×4 neighbourhood of points and applies a piecewise polynomial function to them. The bicubic interpolation algorithm used by Matlab was published by Keys[16], the function used by *Java Advanced Imaging* (JAI) can be found in the JAI manual[17].

Bicubic interpolation produces the least artifacts of these techniques, however it is not clear how the different methods influence fractal dimension estimation algorithms.

2.3.3. Segmentation

For a successful classification of different types of fibrosis, in a preliminary step fibrosis in the obtained images has to be detected. Hence it was necessary to quantify the in the case of fibrosis increased amount of connective tissue in the analysed images. Therefore, each pixel of an image has to be classified as *fibrotic* or *non-fibrotic*. Such a classification can be achieved by an image segmentation. A broad variety of different algorithms for segmentation exists.

Often they are based on the fact that image-regions, which belong to the same class, have related colour values. For instance connective tissue, depending on the staining technique, may have a major red (*Picrosirius Red*) or blue (*Trichrome*) component in the image. Hence, one aims to separate regions, e.g. by introducing thresholds and assigning the classes *connective/fibrotic tissue* or *other/non-fibrotic tissue* to these regions. The following techniques were tested during the work of this thesis. Their procedures are briefly described below, details on the more advanced algorithms can be found in the cited literature.

- The simplest segmentation algorithm is **Colour Thresholding**. Thresholds for each colour channel can be set individually to define ranges. Each image pixel is assigned to one of the two classes: In or out of the given range. For instance, all pixels having red values between 100 and 200 and blue values between 50 and 100 are assigned to class 1, all others are assigned to class 2.

- The **RGB Relative** segmentation algorithm uses the intensity values of the three bands (R, G, B) of an RGB image to calculate a ratio r, e.g. $r = R/(R+G+B)$. This ratio is used as a new value for each pixel and a *ratio threshold* r_{th}, e.g. $r_{\mathrm{th}} = 0.5$ is used to segment an image into two classes.

- **k-means Clustering** is a popular algorithm that partitions an image into k clusters. Each pixel belongs to the cluster with the nearest mean value. The problem of finding the clusters by minimizing within-cluster distances is computationally difficult but there are efficient algorithms that can find a local optimum rather quickly. The underlying details were published e.g. by Lloyd[18].

- The more advanced **Colour Deconvolution** algorithm tries to deconvolute histological images into the parts/tissues that were stained with different dyes. The colour vectors (defining the individual dyes), which had to be found or guessed

previously to the application of this procedure, are the most important parameters for this method. The underlying quite mathematical details can be found in corresponding literature[19].

All these procedures can be applied to images given in different colour models (RGB, CIE L*a*b*, ...).

3. Fractals

In the first part of this chapter the question why fractals are useful in biology and especially in medical image or signal analysis is answered. Furthermore, fractal properties are outlined and the term *Fractal Dimension* (D) is introduced from a mathematical point of view. Since it is one of the most carefully studied definitions, the Hausdorff-Besicovitch Dimension is presented. Its value is very hard or even impossible to calculate in practice, hence the easier accessible and often used Box-Counting Dimension is described subsequently. While the approach within this chapter is very theoretical and mathematical, an application-oriented description of the methods implemented and used during this work is given in the following chapter 4.

3.1. Why Fractals?

In large parts of the mathematical world everything is describable with the traditional Euclidean geometry. The objects, which inhabit these parts, can be characterized with a dimension having an integer value. However, there are these other parts, where this is not possible anymore. Especially if one looks at objects existing in nature it is quite hard or nearly impossible to find objects having strictly Euclidean geometry. There had been times when scientists were afraid of these structures. They had been described as monstrous, pathological and even psychopathic[20]. However, there had been unterrified pioneers, which investigated these monsters.

In 1981 Paumgartner et al.[21] showed in a pioneering study that the results obtained from image analysis of subcellular membrane systems seemed to depend on the resolution scale used. Their estimations for the surface density of inner mitochondrial membranes and endoplasmic reticulum increased significantly as the magnification of their images was increased. This behaviour was explained by a *resolution effect*, using

a concept proposed by Benoit B. Mandelbrot[20]: The concept of *fractals*. If fractals are investigated, similar patterns and structures are gained at different scales because finer shapes are revealed every time the resolution is increased. Together with a non-integer value for the dimension this is one of the main characteristics of fractals. In his most popular publication titled *The Fractal Geometry of Nature* Mandelbrot showed that a lot of objects with natural origin have fractal characteristics[22].

Based on these findings also artificial fractals have been designed. As an example the performance of fractal antennas for mobile phones has been enhanced during the last years[23–25]. Further, challenges in bioengineering are often solved by using fractal geometry. For instance, the design and production of scaffolds for artificial blood vessels is a burning issue considering the need of the development of artificial cardiovascular implants[26] or supports for neovessel formation and stabilization[27]. Nevertheless, investigations of fractal objects of natural origin are highly relevant to understand fractal characteristics and their role in nature. In most studies dealing with images taken in a medical context a concept based on non-fractal geometry cannot yield comparable results, as for example Losa et al.[28] stated in their discussion of a publication concerning pyramidal cells in the rat somatosensory cortex[29]. The importance of scaling laws and network structures for the understanding of processes of health and disease in medical research has been outlined very recently[30]. In addition, fundamental concepts of fractal geometry applied to microscopy problems were reviewed by Landini[31].

However, the application of fractal methods has certain requirements on the images under investigation. The resolution needed when calculating fractal properties as well as influences of edge detection algorithms were determined and discussed by Ahammer et al.[32,33]. Therefore, it can be stated that there is a demand for new approaches and methods in fractal analysis which are able to handle images with a high number of pixels in acceptable computational times. Improvement of computational times is also necessary since one future goal of digital pathology is to achieve an in-vivo real-time characterization of tissue.

3.2. Application of Fractals in Medicine

Inspired by the success of calculus in physics in the last centuries, researchers tried to make predictions based on differential equations and smooth continuous functions also in the field of medicine. Despite important findings through this approach they

realized that the majority of the complex phenomena could not be explained with analytic functions. Hence it was necessary to establish a *calculus of medicine* that was able to describe the ever present complexity and nonlinearity in the human body[34]. Weibel[35] investigated the efficiency of fractals in biology and suggested that they are a design principle of living organisms. Since then nonlinear and fractal approaches became standard tools for analysing phenomena in physiology and medicine[34].

3.2.1. Recent Findings

Lately, it has been shown that fractal analysis applied to the surface of human cervical epithelial cells yields results which can be used to distinguish between healthy and cancerous cells[36]. A quantification of the microvascularization of human brain tumours was obtained by checking fractal properties of images showing different angioarchitectures seen in samples of glioblastoma multiforme[37]. It has been shown that neuronal classification is possible by fractal techniques. Alpha ganglion cells in the rat retinae were classified by their dendritic branching complexity by applying fractal concepts to images of the dendritic branching pattern[38]. Branching pattern complexity of retinal vessels was determined with fractal analysis and associated with lacunar stroke subtypes[39]. Very recently, Di Giovanni et al.[40] showed that fractal based measurements are able to determine whether chemotherapy applied on patients with breast tumours is effective. Liver fibrosis is a disease which has been investigated by fractal methods very well[41–44]. Fractal based measurements were able to discriminate the different types of fibrosis. Furthermore, it was possible to detect changes in the structure of fibrosis when it had been treated pharmacologically[45].

3.3. Fractal Properties

Fractal objects have specific properties that distinguish them from non-fractal objects. These properties, namely

- Self-Similarity,
- Scaling Relationship,
- Fractal Dimension, and
- Statistical Properties

are briefly described below. More details can be found in the literature[22,34,46,47].

3.3.1. Self-Similarity

A fractal object is similar to itself at different scales, i.e. it can be split into parts which look like reduced size copies of the whole object. In contrast to non-fractal objects, where no new features are revealed when they are magnified, fractal objects reveal ever finer structures when they are magnified[22,34]. Two different types of self-similarity are distinguished. The term *geometrical self-similarity* is used when the smaller parts of the object are really exact smaller versions of the whole object.
Typically this is only true for mathematical objects. In nature the smaller pieces of fractal objects are usually not exact copies, but their statistical properties are geometrically similar, i.e. a quantity N measured at a certain resolution r_1 is proportional to the same quantity measured at an other resolution r_2:

$$N(r_2) = cN(r_1) \tag{3.1}$$

with c as a constant of proportionality. This is called *statistical self-similarity*[47].

3.3.2. Scaling Relationship

Measured properties of a fractal object depend on the resolution used because of the self-similarity and the ever finer structures revealed with increasing resolution[34,46]. The relationship between a measured quantity N (e.g. length, surface area, etc.) and the resolution r is called *scaling relationship*. The so-called *power law* is the simplest form of the scaling relationship, which reads

$$N(r) = c_1 r^{c_2} \tag{3.2}$$

with the constants c_1 and c_2. A more advanced full form of the scaling relationship is

$$N(r) = c_1 r^{c_2} f\left(\frac{\log(r)}{\log(c_3)}\right) \tag{3.3}$$

where c_3 denotes a constant and $f(x)$ is a periodic function satisfying $f(1+x) = f(x)$[47]. A popular example for a scaling relationship is the measurement of the length of a coastline with finer and finer scales. Richardson[48] found increasing lengths with

decreasing scales for the coastline of Britain. He obtained an underlying power law which was used by Mandelbrot in his famous publication *How long is the coast of Britain*[49]. In practice the power law is used to estimate the fractal dimension of an object under investigation - see also chapter 4.1.

3.3.3. Fractal Dimension

The dimension of a fractal can be seen as a quantitative measure of the self-similarity and scaling relationship. It also describes how much of the space is filled up with the fractal objects. The value of this so-called *fractal dimension* (D) is usually a fraction but can also be an integer. There are also other types of dimensions, e.g. the *topological dimension* (T) or the *embedding dimension* (E). T describes how the points of objects are connected and always has integer values. E gives information about the space in which the objects are contained, its values are usually integers but can also be fractions. Compared to T the value of E is typically larger by one[22,47]. Summarizing, one can state that D is a value for how much an object (with a certain T) fills the surrounding space (with a certain E).

For a more mathematical introduction in the concepts of fractal dimensions see section 3.4 or fundamental literature (e.g. Mandelbrot[22] or Barnsley[46]).

3.3.4. Statistical Properties

Fractal objects have statistical properties that belong to *stable* distributions, which are a more general form of the usually used (asymptotically) *Gaussian* distributions for non-fractal objects. Hence some properties, e.g. the population mean does not exist for fractal objects since the sample means do not converge to a limiting value[47].

3.4. Fractal Dimensions

A variety of definitions for fractal dimensions exist and although all describe the space filling characteristics of an object they are slightly different and also yield different absolute values[47]. In the following the simple self-similarity dimension and the more general form of the Hausdorff-Besicovitch Dimension are described, followed by a mathematical introduction of the popular Box-Counting Dimension.

3.4.1. Self-Similarity Dimension

The Self-Similarity Dimension is the simplest fractal dimension but can be only used to study geometrically self-similar objects. If the simple form of the power law (see section 3.3.2)

$$N(r_1) = N(r_2)^{D_{\mathrm{SS}}} \tag{3.4}$$

with a measure N and different scales r_1 and r_2 holds, the Self-Similarity Dimension is given by the exponent D_{SS}[47]. However, non-mathematical real world objects typically are not geometrically but statistically self-similar. Therefore, a more general definition, e.g. the Hausdorff-Besicovitch Dimension is necessary.

3.4.2. Hausdorff-Besicovitch Measure

The first and most carefully studied definition of a dimension is the *Hausdorff-Besicovitch Dimension* D_{HB}. Thoughts of and correspondences between Cantor and Lebesgue triggered Carathéodory[50] to start first developments in the direction of fractal dimensions in 1914. Based on this work Hausdorff developed his definition of a fractal dimension in 1918[51]. In 1929 Besicovitch[52] extended the theory to its current used form. For its introduction in this thesis the definition of the Hausdorff measure is obligatory. Prior to this some definitions are necessary to implement this Hausdorff measure:

3.4.2.1. Diameter of a set

Given a subset U of the n-dimensional Euclidean space $\Re^n$, where U is not an empty set, the *diameter of* U is defined as

$$|U| = \mathrm{diam}(U) = \sup\{d(x,y) : x,y \in U\} \tag{3.5}$$

with a metric $d(x,y)$[53]. In this definition the Euclidean metric $d(x,y) = |x-y|$ is inserted:

$$|U| = \sup\{|x-y| : x,y \in U\} \tag{3.6}$$

3.4.2.2. Covering of a set

Let S be a subset of the n-dimensional Euclidean space $\Re^n$ and let $\{U_i\}$ be a finite or enumerable sequence of sets U_1, U_2, ... which consist of points in a way that their sum includes all points of S. If the diameter of these sets U_i is not exceeding δ, i.e. $S \subset \bigcup_{i=1}^{\infty} U_i$ with $0 < |U_i| \leq \delta$ for every i, the sequence $\{U_i\}$ is called a *δ-covering of S*[53].

3.4.2.3. Hausdorff Measure

With the previous definitions it is possible to construct a measure: Let k be a non-negative number. For every δ a test function

$$H_\delta^k(S) = \inf \left\{ \sum_{i=1}^{\infty} |U_i|^k : \{U_i\} \text{ is a } \delta\text{-covering of } S \right\} \tag{3.7}$$

is defined. Now δ is decreased which implicates that the test function $H_\delta^k(S)$ can only stay equal or increase since the class of valid coverings of S (see eq. (3.7)) is reduced. If δ is decreased further with $\delta \to 0$ the test function $H_\delta^k(S)$ has a limit

$$H^k(S) = \lim_{\delta \to 0} H_\delta^k(S). \tag{3.8}$$

This limit, which exists for every subset S of $\Re^n$, can be zero, finite and positive or infinite. This limiting value $H^k(S)$, which is defined in eq. (3.8) is called the *k-dimensional Hausdorff measure of S* or more briefly the *k-measure of S*.[22,51,52,54]
The proof for $H^k(S)$ being a measure is not part of this thesis and can be found for instance in the publications of Hausdorff[51] and Besicovitch[52]. Interesting to mention at this point is that for subsets of $\Re^n$ the n-dimensional Hausdorff measure differs from the n-dimensional Lebesgue measure (which is the common n-dimensional volume) just by a constant multiple. E.g. $H^0(S)$ is equal to the number of points in S, $H^1(S)$ is the length of a smooth curve in S, $H^2(S) = \frac{1}{4}\pi \cdot \text{area}(S)$ if S is a smooth surface and so forth[54].

3.4.2.4. Hausdorff-Besicovitch Dimension

Based on the Hausdorff measure introduced above the definition of the Hausdorff-Besicovitch Dimension is possible: For any set $S \subset \Re^n$, there exists a real number $D_{\mathrm{HB}} \geq 0$ in a way that the Hausdorff measure $H^k(S)$ disappears for $k > D_{\mathrm{HB}}$ and is infinite for $k < D_{\mathrm{HB}}$ respectively. This D_{HB} is called the *Hausdorff-Besicovitch Dimension of S*. D_{HB} is also denoted just as the *Hausdorff Dimension*, as the *dimensional number of S* and the set S is said to be an D_{HB}*-dimensional set* or briefly D_{HB}*-set*, respectively[51,52,54].
Note that the Similarity Dimension of a set equals the Hausdorff-Besicovitch Dimension if the set is geometrically self-similar[22].

In contrast to the mathematical point of view, where D_{HB} is easy to handle, in practice it is often impossible to calculate and also very hard to estimate D_{HB}. Nevertheless, it is the most important definition of a fractal dimension because of its well investigated and proofed mathematical foundation.

3.4.3. Box-Counting Dimension

As mentioned before the mathematical well established and proofed Hausdorff-Besicovitch dimension has the disadvantage of being very hard or even impossible to calculate in practice. A more practicable method for determining the dimension of a given set is the so-called Box-Counting method (BCM). This dimension has the advantage to be mathematically gainable or estimatable relatively simply. Therefore it is the dimension most often used.

May U be a non-empty and bounded subset of $\Re^n$. We have sets U_i of $\Re^n$ which cover U and have a maximum diameter of δ. May $N_\delta(U)$ denote the smallest number of these sets. The Box-Counting Dimension D_{BC} of U is equal to the limit

$$D_{\mathrm{BC}}(U) = \lim_{\delta \to 0} \frac{\log(N_\delta(U))}{-\log(\delta)} \tag{3.9}$$

if this limit exists. Its existence is given if the limit inferior (lower Box-Counting Dimension $\underline{D}_{\mathrm{BC}}(U)$) and the limit superior (upper Box-Counting Dimension $\overline{D}_{\mathrm{BC}}(U)$) exist and are equal[53].

Another mathematical definition of the Box-Counting Dimension of U is discussed below. It is equivalent to the definition above, but provides a clearer approach to the common application of the BCM: Again we have U as a non-empty and bounded subset of $\Re^n$. Now cubes in the n-dimensional space are considered which have the form

$$[k_1\delta, (k_1+1)\delta] \times [k_2\delta, (k_2+1)\delta] \times ... \times [k_n\delta, (k_n+1)\delta] \tag{3.10}$$

where k_1, k_2, ..., k_n denote integers. We have a number $N'_\delta(U)$ of cubes which intersect U. Every cube of them is a set of diameter $\delta\sqrt{n}$, therefore

$$N_{\delta\sqrt{n}}(U) \leq N'_\delta(U). \tag{3.11}$$

This can be expanded to

$$\frac{\log(N_{\delta\sqrt{n}}(U))}{-log(\delta\sqrt{n})} \leq \frac{\log(N'_\delta(U))}{-log(\sqrt{n}) - log(\delta)} \tag{3.12}$$

with the conditions that $\delta\sqrt{n} < 1$, $\delta > 0$ and sufficiently small to ensure a positive $-\log(\delta)$. Also the inequality

$$N'_\delta(U) \leq 3^n N_\delta(U) \tag{3.13}$$

is valid since 3^n cubes of side δ contain any sets with diameters of at most δ. By taking the lower and the upper limit $\delta \to 0$ of equation (3.12) the inequalities

$$\underline{D}_{\mathrm{BC}}(U) \leq \underline{\lim}_{\delta\to 0} \frac{\log(N'_\delta(U))}{-\log(\delta)} \tag{3.14}$$

$$\overline{D}_{\mathrm{BC}}(U) \leq \overline{\lim}_{\delta\to 0} \frac{\log(N'_\delta(U))}{-\log(\delta)} \tag{3.15}$$

can be derived. The same procedure with equation (3.13) yields the opposite inequalities:

$$\underline{D}_{\mathrm{BC}}(U) \geq \underline{\lim}_{\delta\to 0} \frac{\log(N'_\delta(U))}{-\log(\delta)} \tag{3.16}$$

$$\overline{D}_{\mathrm{BC}}(U) \geq \overline{\lim}_{\delta\to 0} \frac{\log(N'_\delta(U))}{-\log(\delta)} \tag{3.17}$$

Thus we have an equation for the upper and the lower Box-Counting Dimension:

$$\underline{D}_{\mathrm{BC}}(U) = \underline{\lim}_{\delta\to 0} \frac{\log(N'_\delta(U))}{-\log(\delta)} \tag{3.18}$$

$$\overline{D}_{\mathrm{BC}}(U) = \overline{\lim}_{\delta \to 0} \frac{\log(N'_\delta(U))}{-\log(\delta)} \tag{3.19}$$

Furthermore they are equal which means we have a definition for the Box-Counting Dimension

$$D_{\mathrm{BC}}(U) = \lim_{\delta \to 0} \frac{\log(N'_\delta(U))}{-\log(\delta)} \tag{3.20}$$

which is equivalent to the definition in equation (3.9) since $N_\delta(U)$ can be taken to be the number of cubes of side δ that intersect U. This derivation leads to the following conclusion: To determine the Box-Counting Dimension with equation (3.9), the number of cubes that intersect U can be inserted as N_δ[53].

In practice it is not always possible to evaluate the limit exactly, therefore an estimation for the Box-Counting Dimension D_{BC} of a set U has to be made: Boxes with side lengths δ may be drawn. Then it has to be determined, how many boxes are necessary to include all elements of the set U, which gives the number $N_\delta(U)$. This is done for different values of δ. Out of the graph of $\log(N_\delta(U))$ versus $-\log(\delta)$ the slope of a linear regression line can be calculated, which gives a value for $D_{\mathrm{BC}}(U)$. For further details see e.g. Keller et al.[55], who investigated the characteristics of the Box-Counting Dimension thoroughly. A more practical approach for an estimation of D_{BC} as well as other fractal dimensions is given in chapter 4.

3.5. Fractal Dimension Estimation in Life Sciences

When dealing with fractals in life sciences usually a non-strictly mathematical definition is used. Since digital images obtained from real life objects do not fulfill the conditions for mathematical fractals (the resolution of digital images is finite), methods for determining the fractal properties have to be adapted.

Different algorithms were developed during the years and although they differ in their details, they have basic steps in common for obtaining or estimating the fractal dimension[1,56]:

- Different quantities $N(r)$ of an image are calculated with varying scale size r.
- These quantities are plotted in a double-logarithmic plot versus the scale sizes: $\log(N(r))$ vs. $\log(r)$.

- A regression line (usually least-squares) is fitted through the plotted data. The slope of this regression line can be used to obtain an estimation of the fractal dimension of an image.

The quantities $N(r)$ differ from method to method and mostly act as eponyms for the different approaches. The most popular ones are Box-Counting Methods, fractional Brownian motion methods and area measurement methods. Some of these methods were reviewed by Lopes and Betrouni in 2009 [1]. All methods used for the work of this thesis are described in the following chapter 4 from a practical point of view.

"Doing the coastlines was always my favourite.
Used to have endless fun doing all the little fiddly bits round fjords."

SLARTIBARTFAST[57]

4. Estimation of Fractal Dimensions

Based on the theoretical background outlined above, this chapter introduces the methods which were used to verify the first hypothesis proposed in this thesis, which states that *fractal dimensions of grey value images can be reliably estimated by a pyramidal approach. This pyramidal approach has shorter computational times than standard approaches.* The goal is not to give a fully detailed mathematical, but a comprehensible description that can be used for an easy implementation of the algorithms in the favoured programming language. Nevertheless, of each method the basic concepts are outlined together with important properties and possible advantages and disadvantages, respectively. For the verification of the hypothesis an empirical approach was chosen, hence the introduced methods were tested on artificially created fractal images. The creation of these images, the setup for the empirical study and the results are presented in the following chapters.

In the first section, the terms *measure* and *scale* are introduced, which are used in every practical approach for the estimation of fractal dimensions D. The next section covers the fractal analysis of binary, i.e. black/white images by the popular Box-Counting and the recently developed Pyramid Method. Thereafter, the estimation of D for grey value images is discussed by summarizing current methods and introducing three new pyramidal algorithms.

4.1. Common Ground: Image Size, Measures and Scales

All algorithms in this and subsequent chapters are presented for the special case of an application to square images of size $2^n \times 2^n$ with $n \in \mathbb{N}$ and $n > 1$. This approach was chosen for several reasons: First, medical images, especially scans of histological sections, usually have very high resolutions. Hence subsections with sizes $2^n \times 2^n$ of these images can be cut out and used for fractal analysis with little effort. Second, the implementations of the algorithms were optimized for these image sizes. Hence differences in results or computational times due to influences from odd sizes were eliminated.

However, the methods can be adapted for an application to arbitrary rectangular image sizes, but the evaluation of their performance in this case is beyond the scope of this work and might be studied in the future.

As mentioned in section 3.5, all methods estimating fractal dimensions of images have some steps in common. Each method determines quantities $N(r)$, called the *measures* of the method, for varying *scales* r. Usually the methods depend on the construction of a power law, which reflects the nonlinear relationship of the measured quantities (see section 3.3). In general this power law reads

$$N(r) \propto c_1 r^{c_2 D} \tag{4.1}$$

with constants c_1 and c_2. The second variable in the exponent is the value one is usually looking for, the fractal dimension D. The constants c_1 and c_2 in equation (4.1) depend on the underlying topological dimension T of the object under investigation (e.g. 2D-image of a surface: $T = 2$) and the type of measure used by the method.

4.1.1. The log-log Plot

To obtain the fractal dimension D, measure-values $N(r)$ for at least two different scales r must be given. These values are plotted in a double-logarithmic plot (*log-log plot*) versus the scales: $y = \log(N(r))$ vs. $x = \log(r)$. Then a regression line (usually least-squares) $y_{\text{fit}} = k_{\text{fit}} \cdot x + c_{\text{fit}}$ is fitted through the plotted data. The slope of this regression line together with the constants of the underlying power law can be used to estimate

the fractal dimension of the investigated image. When objects with fractal properties, i.e. with (statistical) self-similarity are investigated, the log-log plot shows an approximately linear behaviour, at least in a subregion of the plot. Hence the minimal case of having measures at only two different scales is suboptimal, because no linear characteristic can be concluded from these two datapoints. Therefore, one aims to find a linear characteristic of three or more points in the plot. The goodness of the fit is usually given by the coefficient of determination R^2,

$$R^2 = 1 - \frac{\sum^N y_{\text{resid}}^2}{(N-1)\text{var}(y)} \tag{4.2}$$

with N the number of included data points y, $\text{var}(y)$ the variance of y, and y_{resid} the residual values ($y_{\text{resid}} = |y(x) - y_{\text{fit}}(x)|$).

4.2. Binary Images

Since the development of the binary Pyramid Method was a starting point for the work on this thesis, this section shows how to estimate fractal dimensions of binary images. Black and white images have a topological dimension $T = 1$, and therefore they exhibit fractal dimensions D of $1 < D < 2$. In the following two different methods for an estimation of D are described, namely the *Box-Counting* and the *Pyramid Method*.

4.2.1. Box-Counting Method

Based on the concepts of the Hausdorff definition of a dimension (see section 3.4.2), the *Box-Counting Method* (BCM) was defined by Russell et al.[58] and is the most popular algorithm in nowadays fractal analyses[1,22,51]. The standard approach for estimating the Box-Counting Dimension (D_{BC}) of a binary (black/white) two-dimensional image I uses squares with given side lengths s. Firstly, the image is covered with theses squares. Then it has to be determined how many of them are necessary to cover all elements with a specific value (black or white) of the image. This results in a number N_s, which is the measure of this method. The described procedure is repeated several times for different sizes of the squares, i.e. different values of s (as schematically depicted in Figure 4.1a). Out of the double logarithmic graph of $\log(N_s)$ vs. $\log(1/s)$, the slope of

the linear fit k_1 can be estimated, which provides a value for D_{BC} of the binary image with $D_{BC} = -k_1$[1,46].

The mathematical foundations and characteristics of the BCM are well investigated and its limitations (binarization, strictly valid only for statistically self-similar sets, box-size sensitivity) are known[55,59–61]. The BCM is easily implemented and it is used throughout scientific communities dealing for example with images or signals originating in diverse medical investigations (e.g. photographs, histological images, optical coherence tomography, ...)[38,62,63]. Nevertheless, there exist several disadvantages of BCMs, e.g. the high computational time needed for evaluating the fractal dimension of images with high pixel count. Further, BCMs have limitations regarding the choice of the box-sizes. First pointed out by Pickover and Khorasani[64] there were studies to find upper and lower limits for the box sizes and it was shown that the BCMs underestimate the true values of the fractal dimensions. Disturbance by noise which also leads to lower fractal dimension values was investigated[64–67].

4.2.2. Pyramid Method

Recently, the determination of the fractal dimension using a new method has been developed by our group[2,68]. The approach of the method is the origin of the introduced names *Pyramid Method* (PM) for the method itself and *Pyramid Dimension* D_P for the fractal dimension value obtained, respectively. It uses image pyramids which are in fact sequences of identical images but at different sizes. The original image having the biggest size represents the bottom of the pyramid. The size of this bottom image is then reduced successively until it is no more than one pixel, which can be thought of as the top of the pyramid (see Figure 4.1b for an illustration). For each image size s the number N_s of object pixels is counted, with N_0 as the number of object pixels in the original image. From the double logarithmic graph of $\log(N_s/N_0)$ vs. $\log(s)$, the slope of the linear fit k_1 can be estimated, which provides a value for the fractal dimension of the binary image with $D_P = k_1$ Hence, the PM is derived from the BCM described above, but uses different images sizes instead of different box sizes[2].

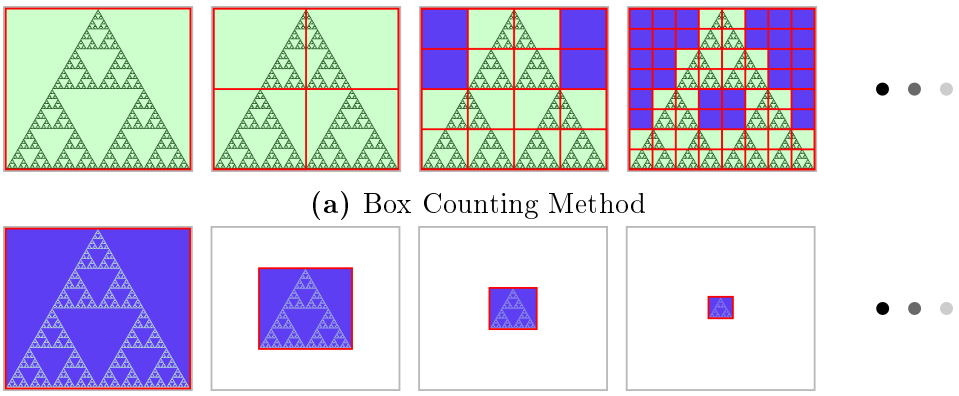

(a) Box Counting Method

(b) Pyramid Method

Figure 4.1.: Principles of the binary Box-Counting (a) and Pyramid Method (b). Different iteration steps (box sizes (a), image sizes (b)) of the methods are shown. In (a) the green regions indicate boxes contributing to the measure of the current scale (i.e. boxes that include at least one non-zero pixel), the blue regions indicate empty boxes (i.e. boxes in which all pixels are zero). In (b) the green regions indicate non-zero pixels that contribute to the measure of the current scale, the blue regions indicate pixels with a value of zero.

4.3. Grey Value Images

For the determination of fractal dimensions of grey value images the algorithms used for binary images have to be adapted or new methods have to be found. Usually the grey value of a pixel within a two-dimensional image having position (x, y) is taken as the z-coordinate. Thus, images are represented by a surface in three-dimensional space, actually having a topological dimension of $T = 2$ and a fractal dimension D fulfilling $2 < D < 3$. In the following, different methods for an estimation of D are described. In addition to already published methods based on Box-Counting (*Differential Box-Counting Method*, *Improved Differential Box-Counting Method*), frequency analysis (*Fourier Method*), direct differences (*Higuchi 2D Method*), and surface area estimation (*Minkowski Blanket Method*, *Triangular Prism Method*), three new pyramidal algorithms (*Pyramid Triangular Prism*, *Pyramid Gradient*, and *Pyramid Differences Method*) are presented.

4.3.1. Box-Counting Methods

Box-Counting Methods (BCMs) are the most widely used approaches for estimating the fractal dimension of images[22]. Hence they usually act as a baseline when new methods

are introduced or different methods are compared. Their mathematical background was outlined in section 3.4.3 of this work.

The most simple implementation of the BCM covers the three-dimensional space with boxes having a given side length. At every horizontal position the number of boxes containing the signal is counted and afterwards summed up over all positions, this is repeated for different box sizes. Based on these sums and the side lengths of the boxes, the fractal dimension can be estimated. Although this approach has the advantage of being really simple, different and better alternatives for calculating the Box-Counting Dimension exist. Two of the most often used and best performing approaches were implemented for this work and are outlined in the following.

Differential Box-Counting Method

The *Differential Box-Counting Method* (DBCM) has been proposed by Sarkar and Chaudhuri[69,70] and tested extensively[71,72]. For this method an image I of size $M \times M$ is partitioned into tiles of size $s \times s$. On every tile i there is a box-column with boxes of size $s \times s \times s'$, with s' fulfilling $G/s' = M/s$. G denotes the number of grey values in the image. Let the minimum grey value of the image in tile i fall in box number l and the maximum in k. The contribution $n_{s,i}$ of the ith tile is defined as

$$n_{s,i} = k - l + 1. \tag{4.3}$$

As a measure in this method, for every s the sum N_s is calculated by summing up over all tiles

$$N_s = \sum_i n_{s,i}. \tag{4.4}$$

For the scaling variable $r = s/M$ is used. Figure 4.2a illustrates the procedure of the DBCM.

The fractal dimension D_{DBC} is estimated from the slope k_l of the linear fit of $\log(N_s)$ versus $\log(1/r)$ with $D_{\mathrm{DBC}} = k_\mathrm{l}$[73].

Improved Differential Box-Counting Method

Several works suggested improvements of the DBCM[74,75], which were summarized, extended and tested by Li et al.[76] in 2009. They proposed three modifications of the

classical DBCM approach described above. The starting point is the same as above, an image of size $M \times M$ which is partitioned into tiles of size $s \times s$. In the first modification, the box height s' which is usually calculated with the relation $G/s' = M/s$, is replaced with a box height s'_{improved} given by

$$s'_{\text{improved}} = \frac{s}{1 + a\sigma} \tag{4.5}$$

with σ the standard deviation of all grey values the investigated image. a denotes a positive integer which can be optimized with artificially created fractal images with known fractal dimensions. $a = 3$ was found to be an appropriate choice[76]. For the second modification, the box number is now determined by calculating the difference between maximum grey value k and minimum grey value l in every tile i first. Then the number of boxes necessary to include this range is obtained with

$$n_{s,i}^{\text{improved}} = \begin{cases} \text{ceil}\left(\frac{k-l}{s'_{\text{improved}}}\right), & k \neq l \\ 1, & k = l \end{cases}. \tag{4.6}$$

This part of the improvement is also known as *Relative Differential Box-Counting Method*[75] (see Figure 4.2b). Again the sum over all tiles is taken as the measure N_s with

$$N_s^{\text{improved}} = \sum_i n_{s,i}^{\text{improved}}. \tag{4.7}$$

For the third modification, also known as *Scanning* or *Shifting* DBCM[74], spatially adjacent tiles overlap at their boundary by one row, i.e. the pixels at the boundary of the boxes may contribute to $n_{s,i}^{\text{improved}}$ of more than one tile i. An overlap of more than one pixel is possible, however, the overlap of one pixel was found to be the optimum choice[76]. Due to this overlap, $r = s - 1$ is used as the scaling variable of this method.

The fractal dimension $D_{\text{DBC}}^{\text{improved}}$ is estimated from the slope k_1 of the linear fit of $\log(N_s^{\text{improved}})$ versus $\log(1/r)$ with $D_{\text{DBC}}^{\text{improved}} = k_1$[76].

4.3.2. Fourier Method

A widely used approach for an estimation of D is frequency analysis[77–79]. Usually this is implemented computationally by transforming an image $I(\mathbf{x})$ into frequency space

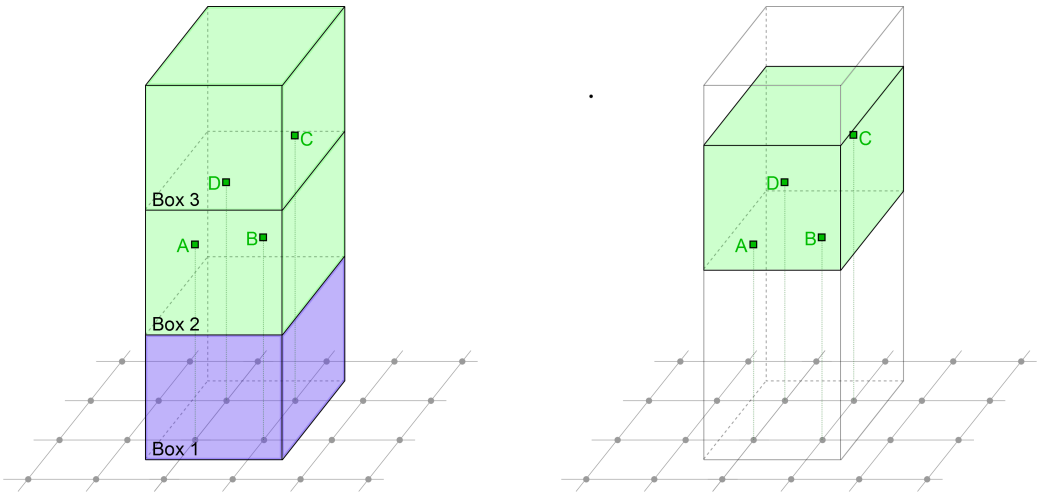

(a) Standard DBCM **(b)** Relative DBCM

Figure 4.2.: Principles of the standard Differential Box-Counting Method (DBCM) (a) and the Relative DBCM (b) which is a part of the Improved DBCM. The example shows one tile with a scale $s = 2$, i.e. four pixels values (points A,B,C,D) are included. In this example the standard DBCM counts two boxes (points A,B,D are in Box 2, point C is in Box 3) for this tile, while the Relative DBCM counts only one box, since all four grey values can be included in a single box.

(**k**-space) with the (discrete) Fast Fourier Transformation (FFT)

$$I(\mathbf{k}) = \mathcal{F}(I(\mathbf{x})), \tag{4.8}$$

$\mathbf{k} = (k_x, k_y)$. For that reason this method is often referred to as *Fourier Method* or *FFT Method*. The result in **k**-space $I(\mathbf{k})$ is used to calculate the power spectrum $P(\mathbf{k})$ with

$$P(\mathbf{k}) = |I(\mathbf{k})|^2. \tag{4.9}$$

The usual behaviour of the power spectrum is

$$P(\mathbf{k}) = c|\mathbf{k}|^{-\beta} \tag{4.10}$$

with a constant c. Hence the exponent β can be found by analysing the power spectrum (4.9) as a function of the distance in **k**-space $\Delta k = \sqrt{(k_x^2 + k_y^2)}$. The fractal dimension D_F is estimated from the slope k_l of the linear fit of $\log(P(\mathbf{k}))$ versus $\log(\Delta k)$ with[78,80]

$$D_\mathrm{F} = \frac{8 - |k_\mathrm{l}|}{2}. \tag{4.11}$$

4.3.3. 2D Higuchi Method

For the first time the principle of the Higuchi Method was proposed for an efficient estimation of D of one-dimensional data streams[81]. Recently, these ideas were extended to *pseudo* 2D[82] and *real* 2D[83,84] methods. Ahammer et al.[84] showed that several approaches for a 2D implementation yield satisfying results without significant differences. Hence one of them was chosen and implemented for the work of this thesis, namely the *K-fold Differences Method*, referred to as *2D Higuchi Method* (HM) throughout this work. This method is based on the calculation of so-called *difference areas*. Let I be a digital image with size $N \times N$ and grey values $z(x, y)$. A difference area is defined as the grey value difference multiplied with the distance of two neighbouring points. Contributions from areas created by pairs of four adjacent data points are summed up. These points are are given by

$$\begin{aligned} z^k_{i,j} &= z(n + ik, m + jk) \\ z^k_{i-1,j} &= z(n + [i-1]k, m + jk) \\ z^k_{i,j-1} &= z(n + ik, m + [j-1]k) \\ z^k_{i-1,j-1} &= z(n + [i-1]k, m + [j-1]k) \end{aligned} \tag{4.12}$$

where k is the step width (scale) and $n = [1, 2, ..., k], m = [1, 2, ..., k]$ denote the *offset*.

All four created areas are summed up with

$$\begin{aligned} A_{n,m}(k) = \frac{\Omega^k_{n,m}}{k^2} \sum_{i=1}^{\omega^k_n} \sum_{j=1}^{\omega^k_m} \frac{1}{4} (&|z^k_{i-1,j} - z^k_{i-1,j-1}|k + |z^k_{i,j} - z^k_{i-1,j}|k + \\ &+ |z^k_{i,j-1} - z^k_{i-1,j-1}|k + |z^k_{i,j} - z^k_{i,j-1}|k) \end{aligned} \tag{4.13}$$

to obtain the whole area $A_{n,m}(k)$ for specific values of k, n and m with

$$\Omega^k_{n,m} = \frac{(N-1)^2}{\left\lfloor \frac{N-n}{k} \right\rfloor \left\lfloor \frac{N-m}{k} \right\rfloor k^2} \tag{4.14}$$

as the 2D normalization factor. $\lfloor \ \rfloor$ denotes the floor function. The upper boundaries

for the sums are given by

$$\begin{aligned} \omega_n^k &= \left\lfloor \frac{N-n}{k} \right\rfloor \\ \omega_m^k &= \left\lfloor \frac{N-m}{k} \right\rfloor \end{aligned} \tag{4.15}$$

As a measure the mean value of the results for different offsets n, m is determined with

$$A(k) = \frac{1}{k^2} \sum_{n=1}^{k} \sum_{m=1}^{k} A_{n,m}(k). \tag{4.16}$$

The procedure is repeated for different scales k.

The fractal dimension D_{H} is estimated from the slope k_{l} of the linear fit of $\log(A(k))$ versus $\log(k)$ with $D_{\mathrm{H}} = -k_{\mathrm{l}}$[84].

4.3.4. Minkowski Blanket Method

This technique for determining the surface area was introduced by Peleg[10] and based upon a method for calculating the length of a curve suggested by Mandelbrot[22]. Within this method a volume is introduced with which the surface is covered, the so-called *blanket*. This blanket has a given thickness. With dividing the volume by this thickness an estimation for the surface area is obtained:
The blanket around a grey value surface (given by a continuous function $g(x, y)$, $x, y \in [0, 1]$) is created out of an upper $u_\epsilon(x, y)$ and a lower surface $b_\epsilon(x, y)$ with $\epsilon \geq 1$. For every point $g(x, y)$ and all values of ϵ

$$b_\epsilon(x, y) \leq g(x, y) \leq u_\epsilon(x, y) \tag{4.17}$$

is fulfilled. Since both $u_\epsilon(x, y)$ and $b_\epsilon(x, y)$ are continuous the volume $V(\epsilon)$ of the blanket (volume between b_ϵ and u_ϵ) is computed with

$$V(\epsilon) = \int_0^1 \int_0^1 (u_\epsilon(x, y) - b_\epsilon(x, y)) \mathrm{d}x \mathrm{d}y \tag{4.18}$$

The data of grey value surfaces of digital images cannot be continuous, thus $u_\epsilon(x, y)$ and $b_\epsilon(x, y)$ are now replaced with discrete functions $(\hat{u}_\delta(k, l)$, $\hat{b}_\delta(k, l))$ with $(k, l) \in [N \times N], N \in \mathbb{N}$ and $\delta \in \mathbb{N}_0$. Starting with $\hat{u}_0(k, l) = \hat{b}_0(k, l) = g(k/N, l/N)$ the upper

and lower surface are defined by induction as

$$\hat{u}_\delta(k,l) = \max\left\{\hat{u}_{\delta-1}(k,l)+1,\ \underbrace{\max}_{|(p,q)-(k,l)|\leq 1}\ \hat{u}_{\delta-1}(p,q)\right\} \tag{4.19}$$

and

$$\hat{b}_\delta(k,l) = \min\left\{\hat{b}_{\delta-1}(k,l)-1,\ \underbrace{\min}_{|(p,q)-(k,l)|\leq 1}\ \hat{b}_{\delta-1}(p,q)\right\}, \tag{4.20}$$

an illustration is depicted in Figure 4.3. In equation (4.18) the integral can now be replaced by a sum which leads to

$$V(\delta) = \sum_{k=0,l=0}^{N} (\hat{u}_\delta(k,l) - \hat{b}_\delta(k,l)). \tag{4.21}$$

with the prefactor handling the normalization. Dividing the volume by 2δ results in the surface area:

$$A(\delta) = \frac{V(\delta)}{2\delta} \tag{4.22}$$

To isolate just features that change from scale $\delta - 1$ to scale δ another definition is preferred:

$$A(\delta) = \frac{V(\delta) - V(\delta-1)}{2} \tag{4.23}$$

In these equations the factor 2 in the denominator takes the influences of both the upper and the lower surface into account. Both definitions are identical for an object of mathematically fractal geometry because its properties does not change with scale. However, for objects of not strictly mathematically fractal geometry the isolation of features from smaller scales is mandatory, which is taken into account by the subtraction of $V(\delta-1)$. Hence definition (4.23) leads to reasonable values for both nonfractal and fractal objects. The fractal dimension $D^{\text{Peleg}}_{\text{Blanket}}$ is estimated from the slope k_l of the linear fit of $\log(A(\delta))$ versus $\log(\delta)$ with $D^{\text{Peleg}}_{\text{Blanket}} = 2 - k_\text{l}$ [10,85].

Deviations from the standard definition described above are possible: For instance the regions from which the maximum and minimum values for the upper and lower surfaces of the blanket are evaluated can be expanded: Definitions (4.24) and (4.25) show the minimal case where just the four direct neighbours are included[10].

A slightly different approach was chosen by Dubuc et al.[86] who calculated upper and

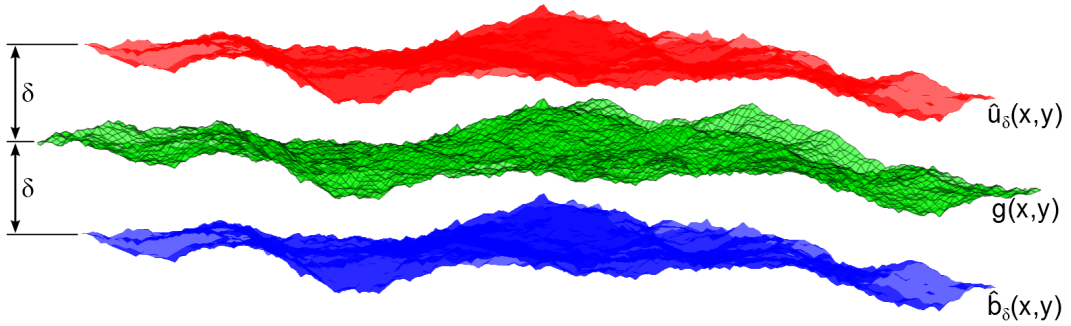

Figure 4.3.: Principle of the Minkowski Blanket Method. The grey value surface ($g(x,y)$, green) of the image is covered with an upper ($\hat{u}_\delta(x,y)$, red) and a lower ($\hat{b}_\delta(x,y)$, blue) *blanket* with a distance δ from the surface. $\hat{u}_\delta(x,y)$ and $\hat{b}_\delta(x,y)$ are given by equations (4.24) and (4.25).

lower surface with

$$\hat{u}_n^{\text{Dubuc}}(k,l) = \max\left\{\hat{u}_{n-1}^{\text{Dubuc}}(k,l) + \frac{1}{N}, \underbrace{\max}_{|(p,q)-(k,l)|\leq 1} \hat{u}_{n-1}^{\text{Dubuc}}(p,q)\right\} \tag{4.24}$$

and

$$\hat{b}_n^{\text{Dubuc}}(k,l) = \min\left\{\hat{b}_{n-1}^{\text{Dubuc}}(k,l) - \frac{1}{N}, \underbrace{\min}_{|(p,q)-(k,l)|\leq 1} \hat{b}_{n-1}^{\text{Dubuc}}(p,q)\right\} \tag{4.25}$$

where $n \in \mathbb{N}$. The volume between them is obtained with

$$V^{\text{Dubuc}}(n) = \frac{1}{(N+1)^2} \sum_{k=0,l=0}^{N} (\hat{u}_n^{\text{Dubuc}}(k,l) - \hat{b}_n^{\text{Dubuc}}(k,l)). \tag{4.26}$$

To circumvent possible problems due to numerical instabilities of this approach, the fractal dimension $D_{\text{Blanket}}^{\text{Dubuc}}$ is estimated from the slope k_1 of the linear fit of $\log(V^{\text{Dubuc}}(n)/\epsilon_n^3)$ versus $\log(1/\epsilon_n)$ with $D_{\text{Blanket}}^{\text{Dubuc}} = k_1$ where $\epsilon_n = n/N$[86].

An important parameter for the Minkowski Blanket Method is the number of blankets used in the algorithm, because the actual log-log plot is not a strictly linear curve. The optimum number of blankets depends on the size of the image under investigation. Hence it has to be found by evaluating results from artificially generated images or other images with a known fractal dimension. Novianto et al.[87] showed this procedure for a local fractal dimension estimation. They applied the Blanket Method to small parts of images from the Brodatz dataset[88] and compared them to results for the whole images[87].

4.3.5. Triangular Prism Method

The *triangular prism method* (TPM) was introduced by Clarke[89] for the computation of the fractal dimensions of topographic surfaces in 1986. Although it was used effectually for several years, e.g. to compute fractal dimensions of images created from remote-sensing data acquired by the NASA[90], Zhao[91] showed in 2001 that Clarke's algorithm underestimates the fractal dimension. Lam et al.[92] modified the algorithm and improved its outcomes by using the basic equations for the dimension of a fractal curve. Zhou and Lam[93] compared this *modified TPM* with four other fractal dimension estimators (Isarithm[94], Variogram[95], Probability[96], and Variation Method[97]) and showed that together with the Isarithm estimator it outperforms the other techniques. The algorithm, which uses a relationship between the step size s of a grid and the surface area of triangular prisms defined by the grey values of the image, works as follows: The investigated image I with size $N \times N$ is divided into squares of specific size $s \times s$. The grey values of the corner pixels of the square act as the z-coordinate of these points. Then a new point is created in the middle of each base square i, its z-coordinate is given by the mean grey value of the corner pixels of the square. Four triangles $t_{i,j=1,2,3,4}$ are created with this new middle point and the points at the corners of the prism, their area given by $A(t_{i,j})$. In Figure 4.4 the construction of the triangles is illustrated. The top surface area A_i of each of these prisms i is calculated by summing up the contributions of all four triangles $A_i = \sum_j A(t_{i,j})$. As a measure, the total surface area A is calculated by summing over all prisms $A = \sum_i A_i$. The fractal dimension D_{TP} is estimated from the slope k_1 of the linear fit of $\log(A)$ versus $\log(s)$ with $D_{\mathrm{TP}} = 2 - k_1$[92].

In 2009 Ju and Lam[98] presented an improved version of the TPM, namely the *Divisor-Step Method*, which was developed especially to calculate local fractal dimension values. In contrast to the standard implementation, in the divisor-step TPM only step sizes which are divisors of $(W - 1)$, with $W \times W$ the size of the window (subset) of the original $N \times M$-sized image, are taken into account. Its main advantage is that full coverage of the investigated window is guaranteed. Other developments of this method aimed for improved results, e.g. by using different approaches for the calculation of the surface area[99]. However, especially in the case of square images the results of the modified TPM are of equal quality compared to new approaches. Since the rather small advantages of these improvement, usually only having an effect when analysing non-square images, are bought by tolerating higher computational times, they were neglected for this work.

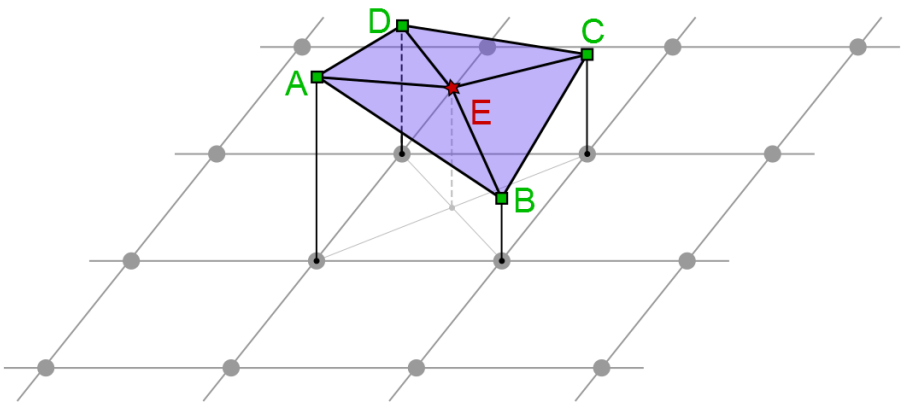

(a) TPM, Creation of the triangles for $s = 2$

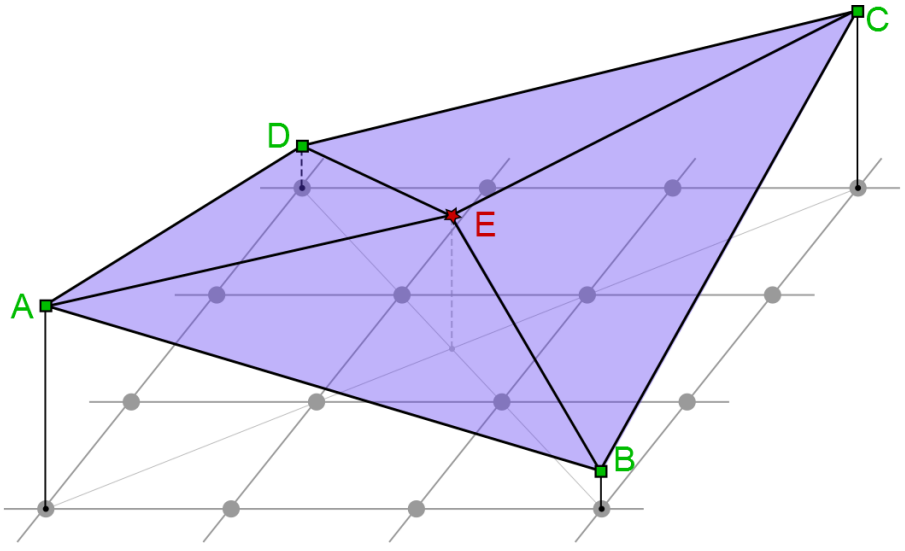

(b) TPM, Creation of the triangles for $s = 4$

Figure 4.4.: Concept of the Triangular Prism Method (TPM) for two different iteration steps, i.e. scales (step sizes) s ((a): $s = 2$, (b): $s = 4$). The areas of the four triangles (blue) created with points A,B,C,D (given) and point E (mean value of A,B,C,D) are calculated and contribute to the total area A.

4.3.6. Pyramid Triangular Prism Method

The good results of the TPM[93] triggered the development of an improved implementation of this method, namely the *Pyramid Triangular Prism Method* (PTPM). As in section 4.3.5 described, for every iteration step, i.e. for every scale s of the TPM, the image $I(\mathbf{x})$ has to be divided into squares of size $s \times s$. Only the pixel values at the corners of these squares are taken into account. An new pyramidal implementation based on this method is the following: An image pyramid is created out of the the original image I_0 with size $N_0 \times N_0$, where I_0 acts as the bottom image of the pyramid. The upper layers of the pyramid are created by decreasing the size of the bottom image. By using different scales s_n, the smaller images I_n for the upper layers have sizes $N_n \times N_n$ with $N_n = N_0/s_n$. The reduction of the image size can be carried out with different interpolation algorithms (e.g. bilinear, cubic, or nearest-neighbour interpolation). Since an image pyramid represents the investigated image at multiple spatial resolutions, it can be used to examine its fractal dimension. The surface area of each of these images is calculated by using the same method as used for the TPM. For every four neighbouring pixels (squares i), middle points are created, their z-coordinates given by the mean grey values of the corner pixels of the squares. Four triangles $t_{i,j=1,2,3,4}$ are created for each of these prisms with this new middle points and the points at the corners of the prisms, their areas given by $A(t_{i,j})$. As a measure, the total surface area A_n is calculated with $A_n = \sum_i A_i$.

Similar to the TPM, the fractal dimension D_{PTP} of the PTPM is estimated from the slope k_1 of the linear fit of $\log(A_n)$ versus $\log(s_n)$ with $D_{\mathrm{PTP}} = 2 - k_1$.

4.3.7. Pyramid Gradient Method

Both the TPM and the PTPM use the surface area as a measure to estimate the fractal dimension of grey value images. However, the area calculation of a surface can be achieved in a different manner, e.g. by using gradients. This approach was used by Chinga et al.[100] to investigate surfaces of supercalendered paper. The here introduced *Pyramid Gradient Method* (PGM) extends this application for estimating D. Let I_0 be the image under investigation with size $N_0 \times N_0$ and grey values $z(x_i, y_j)$ at positions (x_i, y_j). Hence z can be interpreted as a sampled version of a (continuous) height

function of the image, having values (samples) at positions

$$(x_i, y_j) = (ih, jh), \quad i = 1, ..., N_0, \quad j = 1, ..., N_0 \tag{4.27}$$

with h as the shortest lateral distance between the positions of two known values.

The surface area A_c of this function is given by

$$A_c = \int\int \sqrt{1 + \left(\frac{\partial z}{\partial x}\right)^2 + \left(\frac{\partial z}{\partial y}\right)^2} \mathrm{d}x\mathrm{d}y. \tag{4.28}$$

Since we have a sampled version of this function, the area A is calculated with

$$A = \sum_{i,j} \sqrt{1 + \left(\left.\frac{\partial z}{\partial x}\right|_{(x_i,y_j)}\right)^2 + \left(\left.\frac{\partial z}{\partial y}\right|_{(x_i,y_j)}\right)^2}. \tag{4.29}$$

The partial derivatives can be approximated with centered finite difference approximations

$$\begin{aligned} \left.\frac{\partial z}{\partial x}\right|_{(x_i,y_j)} &\approx \frac{z(x_{i+1}, y_j) - z(x_{i-1}, y_j)}{2h} \\ \left.\frac{\partial z}{\partial y}\right|_{(x_i,y_j)} &\approx \frac{z(x_i, y_{j+1}) - z(x_i, y_{j-1})}{2h} \end{aligned} \tag{4.30}$$

where $2h$ denotes the lateral distance of the two points used for these approximations, e.g. the distance between (x_{i+1}, y_j) and (x_{i-1}, y_j).

The derivatives have to be calculated at every image point and then summed up with equation (4.29) to obtain the surface area. In the field of image processing, this application to every image point is usually achieved by convolving the image with a kernel, e.g with size 3×3. The kernel k_x representing the derivative in x-direction of equation (4.30) is given by

$$k_x = \frac{1}{2h} \begin{bmatrix} 0 & 0 & 0 \\ -1 & 0 & 1 \\ 0 & 0 & 0 \end{bmatrix}, \tag{4.31}$$

the kernel k_y representing the derivative in y-direction by

$$k_y = \frac{1}{2h} \begin{bmatrix} 0 & -1 & 0 \\ 0 & 0 & 0 \\ 0 & 1 & 0 \end{bmatrix}. \tag{4.32}$$

The derivatives are given with the convolutions

$$\begin{aligned} \frac{\partial z}{\partial x} &\approx k_x * I, \\ \frac{\partial z}{\partial y} &\approx k_y * I. \end{aligned} \tag{4.33}$$

In image analysis, often the slightly advanced *Sobel*[101] operator is used instead of the simple kernels k_x and k_y. The Sobel algorithm is common in edge detection and approximates the derivatives at each point (x_i, y_j) by including contributions of neighbouring points. For the x-derivative an average of the points (x_i, y_{j-1}), (x_i, y_j) and (x_i, y_{j+1}) with weights 1, 2 and 1 is used. The y-derivative is built from average of points $(x_{(i-1)}, y_j)$, (x_i, y_j) and $(x_{(i+1)}, y_j)$, again with weights 1, 2 and 1, respectively. Hence the Sobel kernels k_x^{Sobel} and k_y^{Sobel} are given by

$$k_x^{\text{Sobel}} = \frac{1}{8h} \begin{bmatrix} -1 & 0 & 1 \\ -2 & 0 & 2 \\ -1 & 0 & 1 \end{bmatrix} \tag{4.34}$$

and

$$k_y^{\text{Sobel}} = \frac{1}{8h} \begin{bmatrix} -1 & -2 & -1 \\ 0 & 0 & 0 \\ 1 & 2 & 1 \end{bmatrix}. \tag{4.35}$$

For an fractal dimension estimation algorithm, the surface areas at different scales has to be calculated. An image pyramid is created out of the the original image I_0 (size $N_0 \times N_0$) as described in section 4.3.6. Upper-layer images I_n with size $N_n \times N_n$ with $N_n = N_0/s_n$ are created by using different scales s_n. From each image of the pyramid, the surface area A_n is calculated with equation (4.29) by using convolutions of the described kernels with the image. Attention has to be paid to the coefficients in the formulas of the kernels. In this pyramidal approach, h has to be replaced with s_n of the current iteration step.

Independent of the used kernels, the fractal dimension D_{PG} of the PGM is estimated from the slope k_{l} of the linear fit of $\log(A_n)$ versus $\log(s_n)$ with $D_{\text{PG}} = -k_{\text{l}}$.

4.3.8. Pyramid Differences Method

Since the fractal dimension gives an estimation for the roughness of an image at different scales, a method based on a measure of this roughness was implemented. A quite simple method to obtain the roughness is to calculate the differences of neighbouring grey values. Let $z(x_i, x_j)$ denote the grey value of an image $I(\mathbf{x})$ at position (x_i, x_j). The differences of the grey values are obtained by summing up all horizontal and vertical contributions

$$\Delta = \sum_{i,j} |z(x_{i+1}, x_j) - z(x_i, x_j)| + |z(x_i, x_{j+1}) - z(x_i, x_j)|, \tag{4.36}$$

no diagonal contributions are taken into account. This method can also be seen as a simplified version of the *2D-Higuchi Method* (*Pseudo 2D Direct Differences*), which uses mean values of differences at different scales for an estimation of D[84]. For the pyramidal implementation of this approach an image pyramid is created out of the the original image I_0 (size $N_0 \times N_0$) as described in section 4.3.6. Upper-layer images with size $N_n \times N_n$ with $N_n = N_0/s_n$ are created by using different scales s_n. From the images I_n of the pyramid, the contributions Δ_n are calculated with equation (4.36).

The fractal dimension D_{PD} is estimated from the slope k_{l} of the linear fit of $\log(\Delta_n)$ versus $\log(s_n)$ with $D_{\mathrm{PD}} = 1 + k_{\mathrm{l}}$[92].

Due to the usage of direct grey value differences in this approach, the method is called *Pyramid Differences Method*.

4.3.9. Additional Methods

Several other methods for an estimation of fractal dimensions of grey value images exist, e.g. the *Isarithm*[94], *Probability*[96], *Variation*[97], or *Variogram Method*[95]. However, their performance is usually worse compared to the described methods above (see e.g. Zhou et al.[93] or Lopes and Betrouni[1]) or their field of application is very narrow, e.g. for determining D as a function of the direction[82,84].

During the work for this thesis, a variety of pyramidal approaches for estimating the fractal dimension of grey value images were implemented and tested, e.g. a method which used different scales of the grey values only (and not of the lateral distances, i.e. distances of pixels). However, only the three presented methods (*Pyramid Triangular*

Prism, *Pyramid Gradient*, and *Pyramid Differences Method*) yielded log-log plots with (at least partly) linear characteristics. None of the other implemented methods was found to be useful or practical for fractal dimension estimation, hence they are not presented in this thesis.

5. Generation of Fractal Images

For the verification of the first hypothesis of this thesis, an empirical approach was chosen. The methods introduced in the last chapter were tested on artificially created fractal images. This chapter covers the generation of these artificial images which have well-defined fractal dimensions. Since a broad variety of different methods exists, the main focus is on the algorithms used throughout this work.

5.1. Binary Images

Since the main aims of this work are based on the evaluation and extension of fractal methods for grey value surfaces, generators for binary fractal images are not outlined in detail and a brief overview is given for sake of completeness. Widely used methods for the creation of binary fractal images are the usage of a deterministic iterative function system (IFS)[46] (e.g. Fern, Sierpinski Carpet), Koch islands and derivations[22] or Diffusion-Limited Aggregates (DLA)[102]. These methods were also used for our publication regarding the PM for binary images[2], which acted as the starting point of this work. Further fractals, such as the Sierpinski triangle, the Koch snowflake, the Heighway Dragon and more exist. All of them have in common that after a high enough number of iteration steps, the created images become (statistically) self-similar and exhibit well-defined and known fractal dimensions D. In the case of a binary image, $1 < D < 2$ holds. As mentioned in the beginning of this paragraph, this list of methods is definitely not exhaustive, but more details would be beyond the scope of this work. A selection of binary fractal images created with IQM[103] is shown in Figure 5.1.

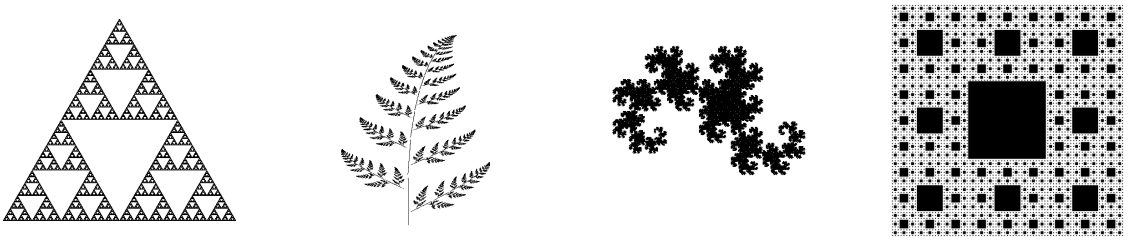

(a) Sierpinski triangle **(b)** Fern **(c)** Heighway dragon **(d)** Menger carpet

Figure 5.1.: Binary fractal images generated with a deterministic iterative function system (IFS) implemented in IQM[103].

5.2. Grey Value Images

In the following, methods used for the creation of artificial grey value images with specific fractal dimensions are described. Three main algorithms were used to obtain the images for the experimental setup of this work and to provide a basis for the evaluation of the implemented fractal dimension estimation algorithms: The *Midpoint Displacement* method, the *Fourier Filtering* method, and *Takagi Surfaces*.

5.2.1. Midpoint Displacement

The *(random) midpoint displacement* algorithm (RMD), which was introduced by Fournier et al.[104] in 1982, was discussed thoroughly by Voss[80,96], who further improved the algorithm (known as *successive random addition* (SRA)) and Saupe[105]. Zhou and Lam[93] revisited the algorithm in 2005 and used the generated surfaces to compare several fractal dimension estimators. As a start for the SRA version of the algorithm, an image with a size of 2×2 pixels is created. The starting pixels have random values obtained from a Gaussian distribution $N(\mu, \sigma^2)$ with arbitrary parameters μ and $\sigma > 0$ (typical starting values are $\mu = 0$ and $\sigma = 1$). Then the following steps are applied recursively (see also Figure 5.2 for clarification)[93,106]:
In the recursive step i, new pixels are created in the centers of all 2×2 squares of the image (figure 5.2, step III). These new pixels have the mean values of their four neighbouring pixels plus random values generated from a Gaussian distribution $N(\mu, \sigma_i^2)$ with

$$\sigma_i^2 = \frac{\sigma^2}{2^{2 \cdot h \cdot i}} \tag{5.1}$$

where h denotes the Hurst[22] exponent with $1 \leq h \leq 2$. Thereafter, the image is virtually rotated by 45° and again new pixels are created in the centers of all 2×2 squares of the image as described above (figure 5.2, step IV). In the last part of the recursive process, the pixels at the edges of the image are created. These pixels have three neighbours instead of four. Nevertheless, their values are the mean values of the three surrounding pixels plus random values determined as described above (figure 5.2, step II). In the end, the image, which is now of size $(2^i + 1) \times (2^i + 1)$, is virtually rotated back in its original orientation All these steps are repeated until the desired size of the image is achieved.

The fractal dimension D of the surface is given by[93]

$$D = 3 - h. \tag{5.2}$$

In Figure 5.3 images with different fractal dimensions created with this method are depicted.

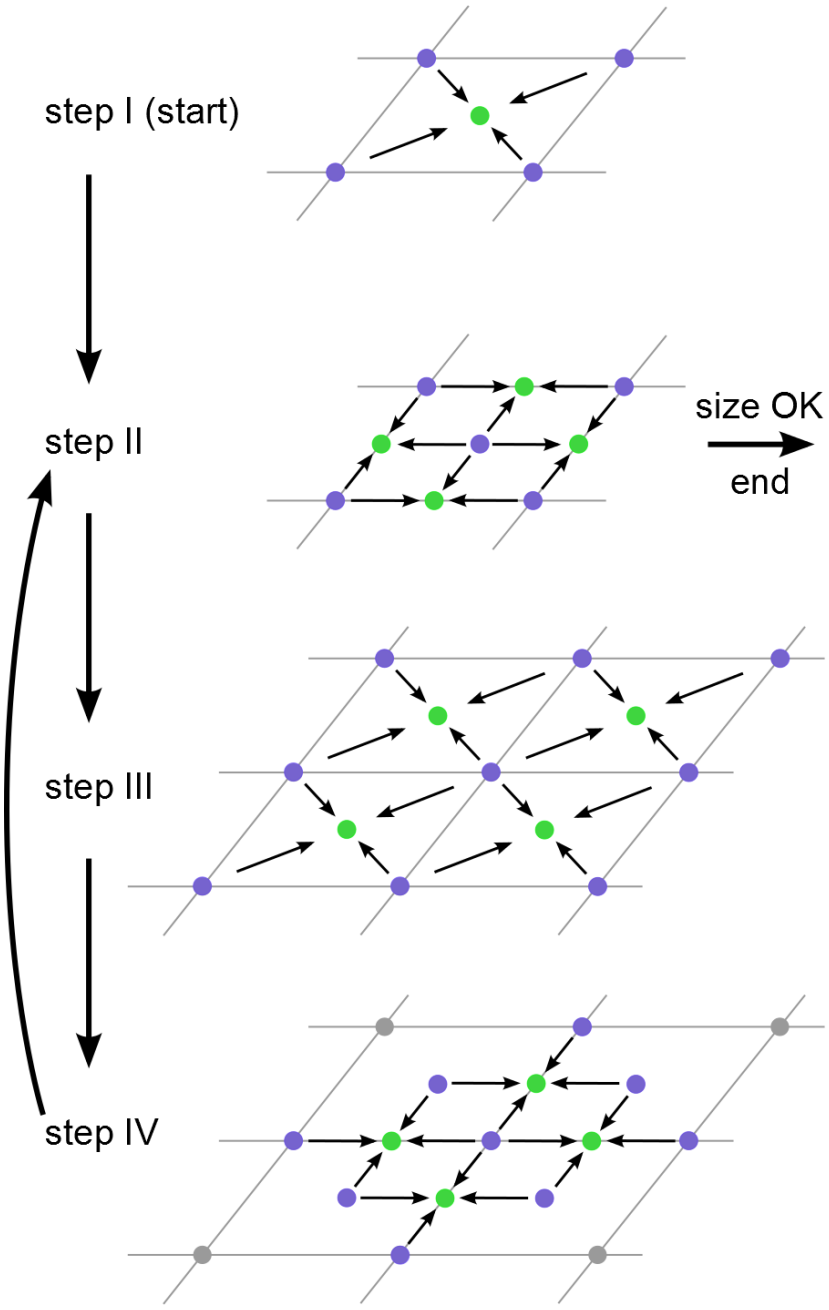

Figure 5.2.: Concept of the Midpoint Displacement Method. Starting from a 2×2 image with four random values (step I), new pixel values are obtained by using mean values of the neighbouring pixels and a random value dependent on the desired fractal dimension (step II - IV). The procedure can be stopped after step II when the desired image size is obtained.

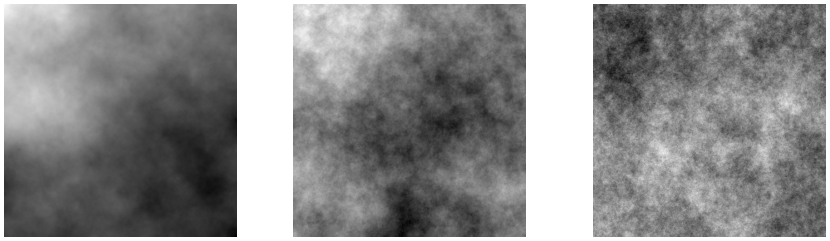

(a) D=2.2 (b) D=2.5 (c) D=2.8

Figure 5.3.: Generation of fractal images with the Midpoint Displacement Method. The depicted images are examples for images with different fractal dimensions D. Since random values are included in the creation process, different images having the same fractal dimension can be generated.

5.2.2. Fourier Filtering

Fractal surfaces can be also generated with the *Fourier Filtering* method[80,105], which is also called *Inverse Fourier Reconstruction* (IFR) algorithm[78]. This name is a good description for the procedure used to obtain images with specific fractal dimensions, which is based on the inverse FFT method for fractal dimension estimation described in section 4.3.2 of this thesis. In a first step an image $I(\mathbf{x})$ with random grey values is Fourier transformed $I(\mathbf{k}) = \mathcal{F}(I(\mathbf{x}))$. Then the power spectrum $P(\mathbf{k}) = |I(\mathbf{k})|^2$ is artificially modified to obtain a linear decay with a specific slope β. In the last step an image with fractal dimension D is obtained with an inverse Fourier transformation with random phases. The relation between D and β is given by[107]

$$\beta = 8 - 2D. \tag{5.3}$$

In Figure 5.4 images with different fractal dimensions created with this method are depicted.

5.2.3. Takagi Surfaces

Introduced by Dubuc et al.[86] these artificial fractal images are based on modified Takagi curves[108,109]. One can see them as a superposition of pyramids of different frequencies and heights. Mathematically they are constructed with

$$f(\mathbf{x} = (x, y)) = \sum_{n=1}^{\infty} b^n \Psi(2^{n-1}x, 2^{n-1}y) \tag{5.4}$$

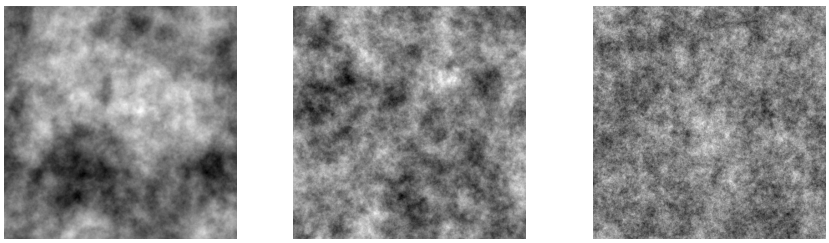

(a) D=2.2 **(b)** D=2.5 **(c)** D=2.8

Figure 5.4.: Generation of fractal images with Fourier Filtering. The depicted images are examples for images with different fractal dimensions D. Since random values are included in the creation process, different images having the same fractal dimension can be generated.

where b denotes an attenuation factor with $\frac{1}{2} < b < 1$ and $x, y \in [0, 0.5]$. The generating kernel Ψ is defined as

$$\Psi(x, y) = |2x - \text{int}(2x)||2y - \text{int}(2y)| \tag{5.5}$$

with int(x) the integer part of x[86,110]. The fractal dimension D of the surface is given by[86]

$$D = \frac{\log(8b)}{\log(2)}. \tag{5.6}$$

In computational practice the upper limit of the sum in eq. (5.4) is replaced by a sufficiently high number or the sum is stopped when the (discrete) pixel values do not change anymore. In Figure 5.5 images showing Takagi surfaces with different fractal dimensions at different iteration steps are shown.

5.2.4. Additional Generators

In addition to the generators described above, there exists further methods to create fractal grey value images, e.g. the *Shear Displacement* Method[95] or the *Weierstrass-Mandelbrot* functions[53,83]. However, the introduced methods performed very well when different fractal algorithms were compared previously[93]. For that reason they were chosen for creating the experimental setup for this work.

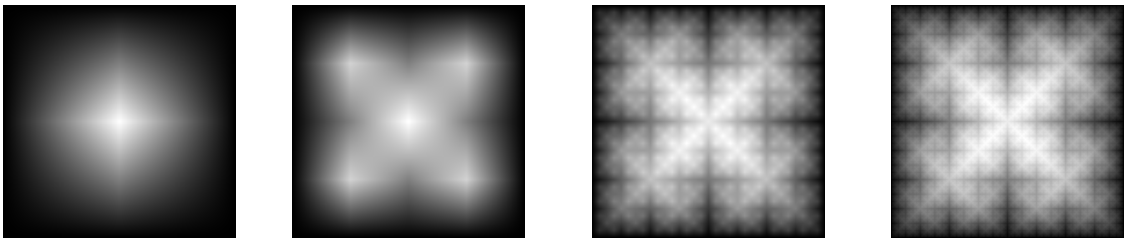

(a) D=2.2, n=1 **(b)** D=2.2, n=2 **(c)** D=2.2, n=5 **(d)** D=2.2, n=20

(e) D=2.8, n=1 **(f)** D=2.8, n=2 **(g)** D=2.8, n=5 **(h)** D=2.8, n=20

Figure 5.5.: Generation of Takagi Surfaces with fractal dimensions $D = 2.2$ (**(a)-(d)**) and $D = 2.8$ (**(e)-(h)**) at different steps n (see eq. (5.4)) in the creation procedure. Since no random values are included in the creation process, there is a unique image for a specific fractal dimension.

6. Experimental Setup

In the previous chapters, methods for estimating fractal dimensions of binary and grey value images and creating artificial images with known D-values were presented. To test the implementations of these methods an empirical study was used. The introduced methods were investigated and compared by applying them to artificially created fractal images. In this chapter the experimental setup for this study is given, i.e. the used hardware, software, and parameters for the algorithms are described in detail. The main focus is on grey value images, however, also the setup for the evaluation of the binary PM is described briefly since it was the starting point for the work on this thesis.

Performance tests of the distinct methods were carried out on a standard workstation of the institute (Intel Pentium G840, 2.80 GHz, 8GB RAM, Windows 7 Enterprise 64 Bit). For comparison all algorithms for fractal dimension estimation were implemented in Matlab (R2013a, 8.1.0.604, 64 bit) and optimized for image sizes $2^n \times 2^n$ with $n \in \mathbb{N}$ and $n > 1$ using the most effective syntax and routines available. D-values for the images were examined according to the individual methods by finding the measures and determining the slopes of the linear regressions of the log-log plots (see chapter 4).

6.1. Binary Images

6.1.1. Generation of Fractal Images

Four different artificial fractal image sets were created with an IFS (Sierpinski Carpet, Fern), a Koch island and a growing DLA - see section 5.1. Each image set included 14

images with increasing self-similarity (14 successive iteration steps of the generation algorithms). The 14^{th} images had the most detailed structures with single-pixel resolution, i.e. their D could be compared to the theoretically known value. All of the images had a pixel size of 4096×4096.

6.1.2. Estimation of Fractal Dimensions

For an estimation of D, the binary BCM and the binary PM were used. Both methods used a scale-range of $s = 2^n$, $n \in \mathbb{N}$, $0 \leq n \leq 12$. For a determination of the computational times, all calculations were repeated ten times to average over slightly varying results caused by varying processor load. Further details of the experimental setup for this study regarding binary images (influences from noise and non-quadratic images) can be found in Ahammer and Mayrhofer-R.[2].

6.2. Grey Value Images

6.2.1. Generation of Fractal Images

In a first step, the artificial fractal grey value images were created with the three methods described in section 5.2: The *Midpoint Displacement* method, the *Fourier Filtering* method, and *Takagi Surfaces*. Four different image sizes were used, namely 512×512, 1024×1024, 2048×2048, and 4096×4096 pixels. These image sizes covered the range of sizes usually used in tissue analysis in digital pathology. Each image pixel had a bit depth of 8, i.e. an integer grey value between 0 (black) and 255 (white). For every image size, images with D-values in the range from 2.1 to 2.9 with a step width of 0.1 were created. The Midpoint Displacement method and the Fourier Filtering method use random numbers, i.e. images having the same theoretical D may have different visual appearances. To eliminate influences due to these different appearances, 50 images were created for each size and each D-value with these two methods. This procedure resulted in 450 images per image size and method. The method of Takagi Surfaces does not use random numbers, hence two or more images having the same theoretical D are identical. Therefore only one image for each size and each D was created with this method, resulting in 9 images per image size. The algorithm was stopped when no more changes in grey values were obtained for further iteration steps (n in equation

(5.4)). All images were saved as TIFF files using lossless LZW compression (see section 2.2.3.3).

6.2.2. Estimation of Fractal Dimensions

To estimate the fractal dimensions D of the created images, the methods described in section 4.3 were used.

A scale-range of $s = 2^n$, $n \in \mathbb{N}$ was used for all but the Fourier Method, the Higuchi Method, and the Minkowski Blanket Methods. The actual range of n depended on the image size, started from $0 \leq n \leq 9$ for 512×512 pixels and went up to $0 \leq n \leq 12$ for 4096×4096 pixels. For the Fourier Method power spectrum values Δk of the lowest 1000 distance values in $\mathbf{k}$-space were used. For the Higuchi Method a scale-range of $k = 1 - 30$ was used. The number of blankets for both Minkowski Blanket Methods (Peleg, Dubuc) was set to $\delta, n = 1 - 100$.

Using these scales seems reasonable since it minimizes computational effort while still providing enough data points for the log-log plots. Furthermore, it was shown that this choice of scales results in accurate absolute D-values[84,111].

Optimization

Two main concepts exist for an optimization of fractal dimension estimation from the log-log plot. One approach scans for the most linear part by maximizing the coefficient of determination R^2, i.e. the quality of fit of the linear regression model (see section 4.1.1). The second approach uses the theoretically known D-values of the artificially created images and minimizes the *root-mean-square deviation* (RMSD) between theoretical and estimated values. The latter one was used throughout this work. As a precondition, at least four data points (four successive scales) were included.

Computational Time

The computational time for estimating D of an image was determined as a function of the image size and the used method. All calculations were carried out in serial computing, the obtained time includes the times for

- loading the file,

- calculating the measures as functions of the scales,
- creating and fitting the log-log plot,
- and obtaining D from the slope of the linear regression.

50 images were used in this evaluation to obtain mean values and standard errors of the means.

Fractal Dimension Variation Range

The fractal dimension variation range is defined as the difference between the estimated D of an image having the highest theoretical D (i.e. 2.9) and the estimated D of an image with the lowest theoretical D (i.e. 2.1). In this study the outcome for an ideal fractal dimension calculation/estimation method should be $2.9 - 2.1 = 0.8$. For an accurate estimation of D and especially for differentiation between images with different D-values, it is important that the used method yields results close to this optimum. Hence also the D *variation range*$= D(D_{\text{theoretical}} = 2.9) - D(D_{\text{theoretical}} = 2.1)$ was evaluated for all methods.

7. Results and Discussion

In this chapter the results of the empirical study described in the previous chapter 6 are presented. The first section briefly shows the advantages of the PM over the BCM when applied to binary images. Thereafter, the main part of this chapter shows the results obtained by applying the different fractal dimension estimation methods introduced in chapter 4 to the artificial images created by the methods described in chapter 5.

7.1. Binary Images

Figure 7.1 shows fractal dimension values obtained by the binary BCM (a) and the binary PM (b) for different standard fractals (Sierpinski Carpet, Fern, Koch Curve, DLA) constructed with a different number of iteration steps. At each iteration step of the images, both methods (BCM, PM) yielded the same value for the fractal dimension. Although standard BCM was optimized during the last years (e.g. by using Summed Area Tables[112,113] (SAT) instead of time-consuming loops), the new approach is about the factor ten faster without having higher memory requirements, which was demonstrated in Ahammer and Mayrhofer-R.[2]. In Figure 7.2 a comparison of computational times is depicted.

This behaviour was also proved in other programming languages, such as Matlab, which is in general optimized for matrix calculations as used by BCM with SAT. Since other binary fractal methods are usually more complex and slower than the optimized BCM, advantages of the PM method over other comparable methods are its simple implementation and a significant reduction of calculation time. Nevertheless, it should be mentioned that the interpolation method used when downscaling the images affects the results of the calculations. With binary images, linear and cubic convolution interpolation algorithms yielded trustable results whereas nearest neighbour resampling should

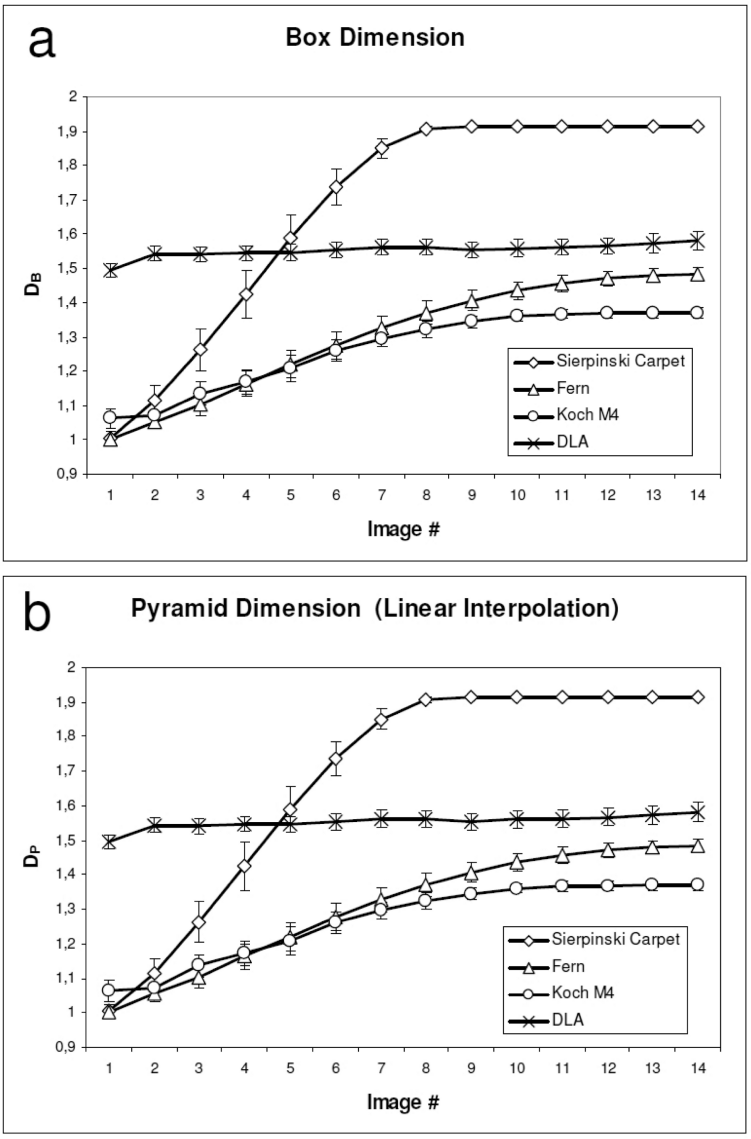

Figure 7.1.: Fractal dimensions for different standard fractals at different iteration steps (Image #) obtained by the BCM (D_B) (a) and the PM (D_P)(b). Figures taken from "*Image Pyramids for Calculation of the Box Counting Dimension*, H. Ahammer and M. Mayrhofer-Reinhartshuber, Fractals Vol **20**, Issue No. 03n04, p. 281-293, ©2012 World Scientific Publishing Company", where also the corresponding fractals are described[2].

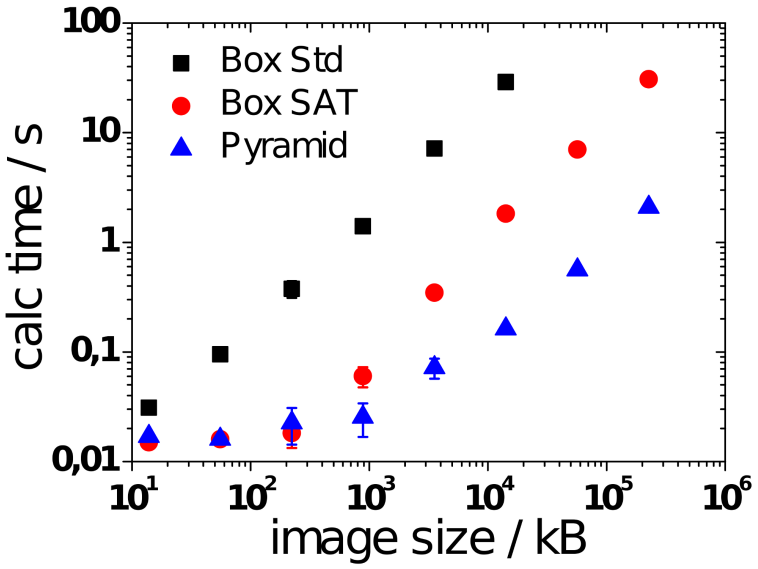

Figure 7.2.: Comparison of calculation times for BCM using loops (Box Std), BCM with Summed Area Tables (Box SAT) and PM (Pyramid) on a standard workstation: Intel Pentium G840, 2.80 GHz, 8GB, Microsoft Windows 7 Enterprise 64 Bit, IQM, JAVA, JAI.

be avoided. Detailed results of this study (influences from noise and non-quadratic images) can be found in Ahammer and Mayrhofer-R[2].

7.2. Grey Value Images

In this section the results of the empirical study described in chapter 6 are presented. The results of the already established methods are shown in the first subsections 7.2.1.1 - 7.2.1.5. Subsequently, the results obtained by the new pyramidal approaches are given in subsections 7.2.1.6 - 7.2.1.8. In the end of this section, the new and already known methods are compared by analysing the quality of their results as well as their computation times.

7.2.1. Estimated Fractal Dimensions

The following figures show the estimated D-values obtained with the different methods described in section 4.3. The optimum scale-range s_{opt} (for pyramidal methods: scale-down factor $s_{n,\text{opt}}$) was found by minimizing RMSD over all investigated generators and image sizes (see section 6.2.2). In the figures the diagonal dashed line represents the theoretical D-values. Results are shown individually for each generator used. While for the MD and the FFT method mean values and standard deviations (SD) for D-values are shown (based on 50 different images per theoretical D-value), the figures for the Takagi surfaces show the estimated D. For each method exemplary log-log plots are given in the appendix A.2, Figures A.1-A.19. They show measures and linear regressions based on the optimum scale-ranges for three different images (theoretical D-values: 2.1, 2.5, and 2.9, created with MD, 2048×2048 pixels). Furthermore, the three best scale-ranges individually optimized for each image size are given in the appendix A.2, Tables A.1-A.19.

7.2.1.1. Box-Counting Methods

The optimum scale-range for the standard DBCM over all image sizes and generators was found to be $s_{\mathrm{DBC,opt}} = 2^5 - 2^8$. Figure 7.3 shows the (mean) values of the estimated D-values ((a)-(c)) together with the standard deviation SD ((a),(b)). For all investigated generators and image sizes the slope of the obtained results is less compared to the theoretical values. While for the images created with MD and Takagi surfaces the absolute D-values are mainly below the theoretical values, the results for the FFT images start too high for small theoretical D-values and are too low for high theoretical D-values. Except for the smallest image size (512×512 pixels) the slopes and absolute values only marginally deviate from each other for images created by the same generator. SD values are higher for lower D-values, smaller image sizes and images created with MD. In the appendix A.2.1, Figure A.1 shows the linear characteristics of the measures throughout the whole scale-range in an exemplary log-log plot. In Table A.1 the three best scale-ranges for each image size are listed separately. The quality of the linear fit was high ($R^2 > 0.99$) for all image sizes and generators.

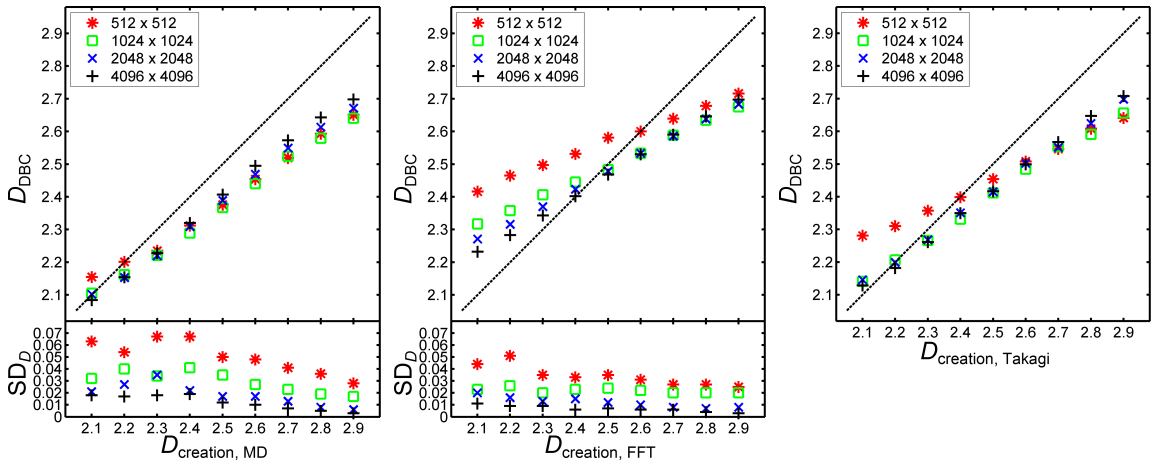

(a) MD **(b)** FFT **(c)** Takagi Surfaces

Figure 7.3.: Estimated D-values (D_{DBC}) obtained by applying the standard DBCM to grey value images created with MD (a), FFT (b) and Takagi Surfaces (c). For (a) and (b) D_{DBC} denotes the mean value, the standard deviation SD is also shown for these generators. For the standard DBCM an optimum scale-range of $s_{\mathrm{DBC,opt}} = 2^5 - 2^8$ was found and used to obtain the shown results. The diagonal line represents theoretical D-values.

The optimum scale-range for the improved DBCM over all image sizes and generators was found to be $s^{\text{improved}}_{\text{DBC,opt}} = 2^4 - 2^8$. Figure 7.4 shows the (mean) values of the estimated D-values ((a)-(c)) together with the standard deviation SD ((a),(b)). For all investigated generators and image sizes the slope of the obtained results is less compared to the theoretical values. For images created with MD and Takagi surfaces the estimated D-values fit well with the theoretical values for low D-values but show increasing deviation for higher D-values. The results for the FFT images start too high for small theoretical D-values and are too low for high theoretical D-values. While the slopes and absolute values of differently sized images only show insignificant differences for images based on MD, estimated D-values for images based on FFT and Takagi surfaces have higher deviations from the theoretical values for smaller image sizes. SD values are low in general (< 0.045) but higher for lower D-values, smaller image sizes and images created with MD. In the appendix A.2.1, Figure A.2 shows the linear characteristics of the measures throughout the whole scale-range in an exemplary log-log plot. In Table A.2 the three best scale-ranges for each image size are listed separately. The quality of the linear fit was high ($R^2 > 0.99$) for all image sizes and generators.

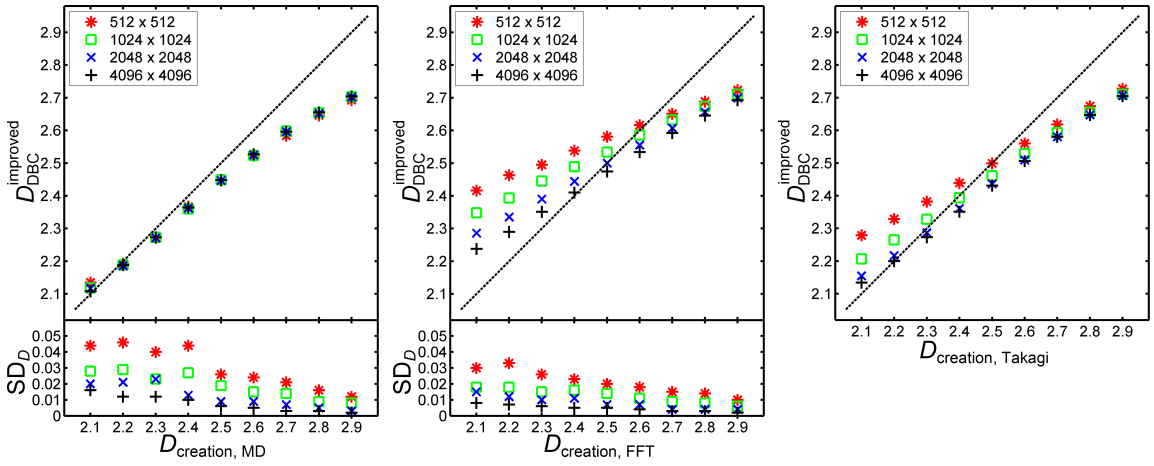

(a) MD **(b)** FFT **(c)** Takagi Surfaces

Figure 7.4.: Estimated D-values ($D^{\text{improved}}_{\text{DBC}}$) obtained by applying the improved DBCM to grey value images created with MD (a), FFT (b) and Takagi Surfaces (c). For (a) and (b) $D^{\text{improved}}_{\text{DBC}}$ denotes the mean value, the standard deviation SD is also shown for these generators. For the improved DBCM an optimum scale-range of $s^{\text{improved}}_{\text{DBC,opt}} = 2^4 - 2^8$ was found and used to obtain the shown results. The diagonal line represents theoretical D-values.

7.2.1.2. Fourier Method

Power spectrum values Δk of the lowest 1000 distance values in **k**-space were used for D-value estimation with the Fourier Method. Figure 7.5 shows the (mean) values of the estimated D-values ((a)-(c)) together with the standard deviations SD ((a),(b)). For images created with MD and FFT the slopes of the obtained results fit well with the theoretical values. The absolute values are too low for MD and too high for FFT, both with rather constant and high (up to 0.2) deviation from the theoretical values. The slopes and absolute values of differently sized images only show marginally differences. SD values are high in general ($0.04 - 0.10$), worse for images created with MD. The results for the Takagi surface images are completely erroneous. In the appendix A.2.2, Figure A.3 shows the rather scattered measures in an exemplary log-log plot. In Table A.3 RMSD and R^2 values are listed separately for each image size. The quality of the linear fit was very low ($R^2 = 0.26 - 0.54$) for all image sizes and generators.

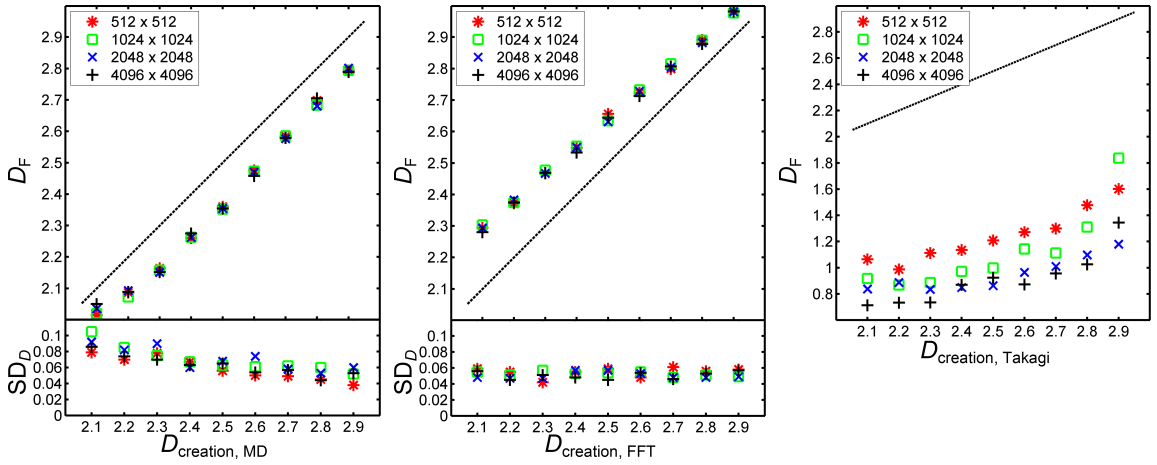

(a) MD **(b)** FFT **(c)** Takagi Surfaces

Figure 7.5.: Estimated D-values (D_F) obtained by applying the Fourier Method to grey value images created with MD (a), FFT (b) and Takagi Surfaces (c). For (a) and (b) D_F denotes the mean value, the standard deviation SD is also shown for these generators. Power spectrum values Δk of the lowest 1000 distance values in **k**-space were used for D-value estimation with the Fourier Method. The diagonal line represents theoretical D-values.

7.2.1.3. 2D Higuchi Method

For the Higuchi Method an optimum scale-range of $k = 1 - 30$ was found for D-value estimation over all images sizes and generators. Figure 7.6 shows the (mean) values of the estimated D-values ((a)-(c)) together with the standard deviations SD ((a),(b)). For images created with MD and Takagi surfaces the slopes of the obtained results fit well with the theoretical values, for images created with FFT the slope is less compared with theoretical values. Also the absolute values fit well for MD and Takagi surfaces. For FFT, the estimated D-values start too high and are too low for high theoretical D-values. The slopes and absolute values of differently sized images only show marginally differences. SD values are very low (< 0.03). In the appendix A.2.3, Figure A.4 shows the linear characteristics of the measures throughout the whole scale-range in an exemplary log-log plot. In Table A.4 the three best scale-ranges for each image size are listed separately. The quality of the linear fit was high ($R^2 > 0.99$) for all image sizes and generators.

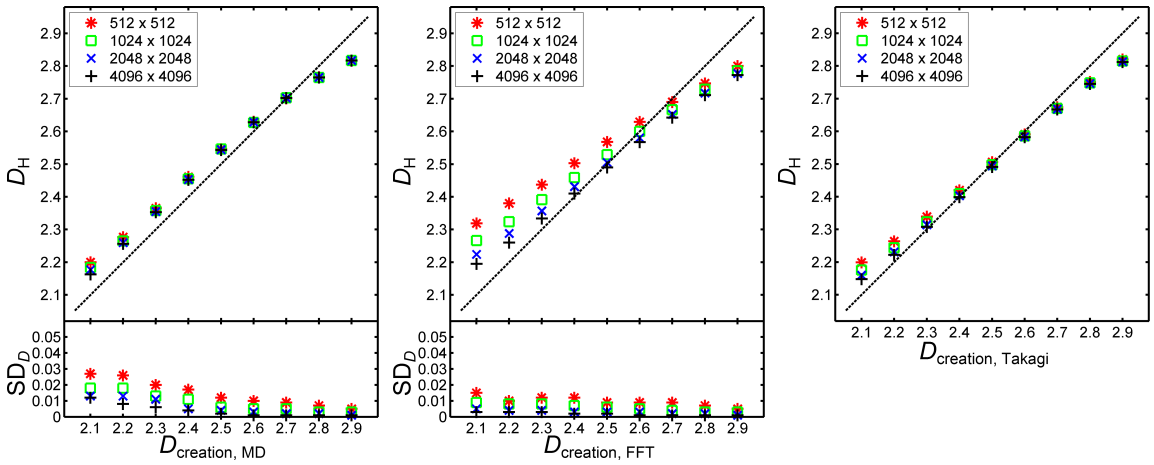

(a) MD **(b)** FFT **(c)** Takagi Surfaces

Figure 7.6.: Estimated D-values (D_H) obtained by applying the Higuchi Method to grey value images created with MD (a), FFT (b) and Takagi Surfaces (c). For (a) and (b) D_H denotes the mean value, the standard deviation SD is also shown for these generators. For the HM an optimum scale-range of $k = 1 - 30$ was found and used to obtain the shown results. The diagonal line represents theoretical D-values.

7.2.1.4. Minkowski Blanket Method

The optimum number of blankets for the Minkowski Blanket Method (Peleg) was found to be $\delta_{\text{opt}} = 1 - 6$. Figure 7.7 shows the (mean) values of the estimated D-values ((a)-(c)) together with the standard deviations SD ((a),(b)). For all images the estimated D-values and their slopes show high deviations for low theoretical D-values, being worse for larger image sizes. SD values are very low (≤ 0.02) for FFT images but higher (up to 0.055) for MD images with low D-values. In the appendix A.2.4, Figure A.5 shows the characteristics of the measures in an exemplary log-log plot. The linearly decaying behaviour for small values of δ changes to a constant value for higher δ-values. In Table A.5 the three best scale-ranges for each image size are listed separately. The quality of the linear fit was high ($R^2 > 0.99$) for FFT and Takagi surface images, but lower for MD images (down to $R^2 = 0.94$).

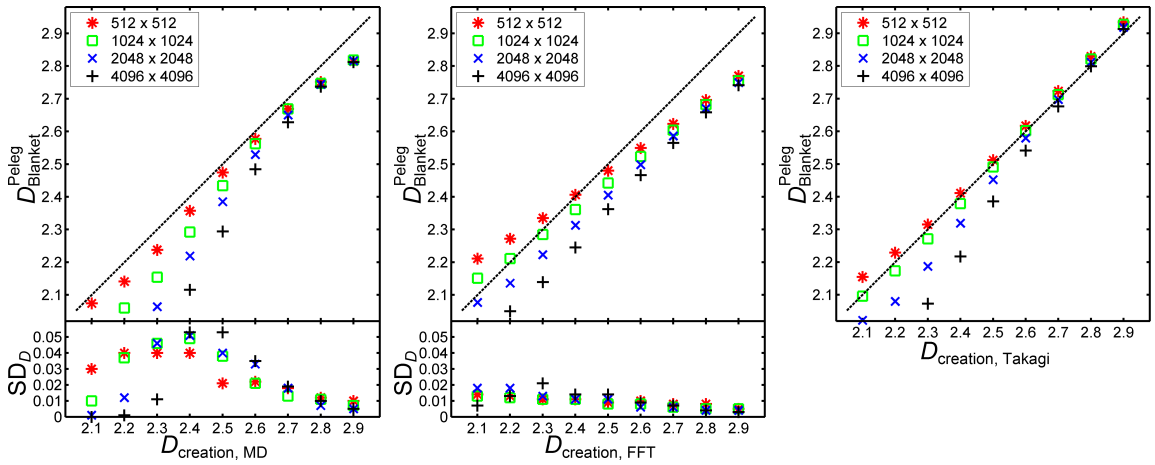

(a) MD **(b)** FFT **(c)** Takagi Surfaces

Figure 7.7.: Estimated D-values ($D^{\text{Peleg}}_{\text{Blanket}}$) obtained by applying the Minkowski Blanket Method (Peleg) to grey value images created with MD (a), FFT (b) and Takagi Surfaces (c). For (a) and (b) $D^{\text{Peleg}}_{\text{Blanket}}$ denotes the mean value, the standard deviation SD is also shown for these generators. For the Minkowski Blanket Method (Peleg) the number of blankets was set to $\delta_{\text{opt}} = 1 - 6$. The diagonal line represents theoretical D-values.

The optimum number of blankets for the Minkowski Blanket Method (Dubuc) was found to be $n_{\text{opt}} = 1 - 100$ over all image sizes and generators. Figure 7.8 shows the (mean) values of the estimated D-values ((a)-(c)) together with the standard deviations SD ((a),(b)). For all investigated generators and image sizes the slope of the obtained results is less compared to the theoretical values. While for the images created with MD and Takagi surfaces the absolute D-values are below the theoretical values, the results for the FFT images start too high for small theoretical D-values and are too low for high theoretical D-values. The slopes and absolute values only marginally deviate from each other for images based on the same generator. SD values are very low (< 0.035), decreasing for increasing image size. In the appendix A.2.4, Figure A.6 shows the linear characteristics of the measures throughout the whole scale-range in an exemplary log-log plot. In Table A.6 the three best scale-ranges for each image size are listed separately. The quality of the linear fit was high ($R^2 > 0.99$) for all image sizes and generators.

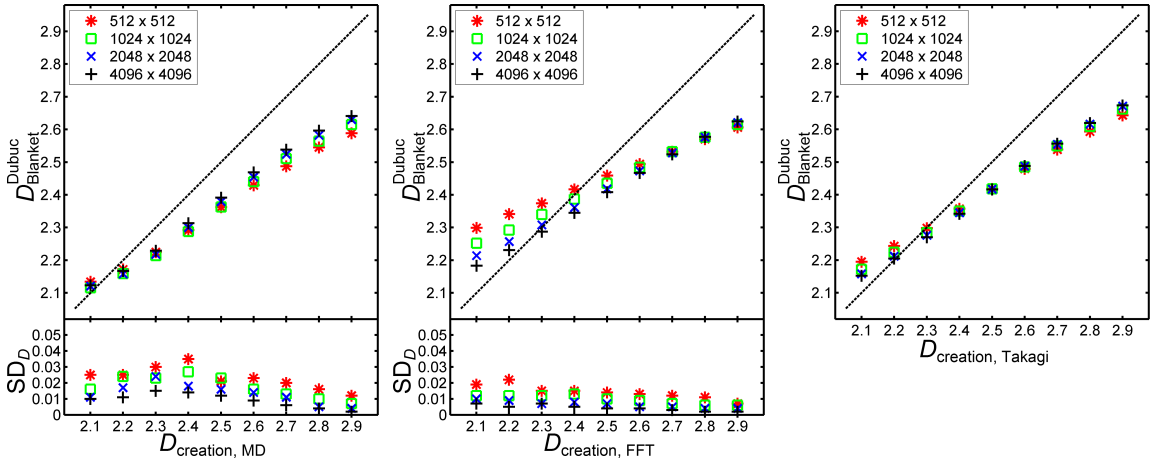

(a) MD **(b)** FFT **(c)** Takagi Surfaces

Figure 7.8.: Estimated D-values ($D^{\text{Dubuc}}_{\text{Blanket}}$) obtained by applying the Minkowski Blanket Method (Dubuc) to grey value images created with MD (a), FFT (b) and Takagi Surfaces (c). For (a) and (b) $D^{\text{Dubuc}}_{\text{Blanket}}$ denotes the mean value, the standard deviation SD is also shown for these generators. For the Minkowski Blanket Method (Dubuc) the number of blankets was set to $n_{\text{opt}} = 1 - 100$. The diagonal line represents theoretical D-values.

7.2.1.5. Triangular Prism Method

The optimum scale-range for the TPM over all image sizes and generators was found to be $s_{\mathrm{TP,opt}} = 2^0 - 2^3$. Figure 7.9 shows the (mean) values of the estimated D-values ((a)-(c)) together with the standard deviation SD ((a),(b)). For all generators most estimated D-values are below the theoretical values, only the results for smaller FFT images start too high for small theoretical D-values. Resulting slopes of the estimated D-values of MD and Takagi surface images are too flat for low D-values (< 2.4). For MD images the slopes also get too steep for high D-values (> 2.4). SD values are very low (≤ 0.03), especially for FFT images (≤ 0.01). In the appendix A.2.5, Figure A.7 shows the characteristics of the measures in an exemplary log-log plot. The linearly decaying behaviour for small values of s changes to constant values for intermediate s-values, before it drops down again for higher s-values. In Table A.7 the three best scale-ranges for each image size are listed separately. The quality of the linear fit was high ($R^2 > 0.99$) for FFT images, but lower for MD and Takagi surface images (down to $R^2 = 0.94$).

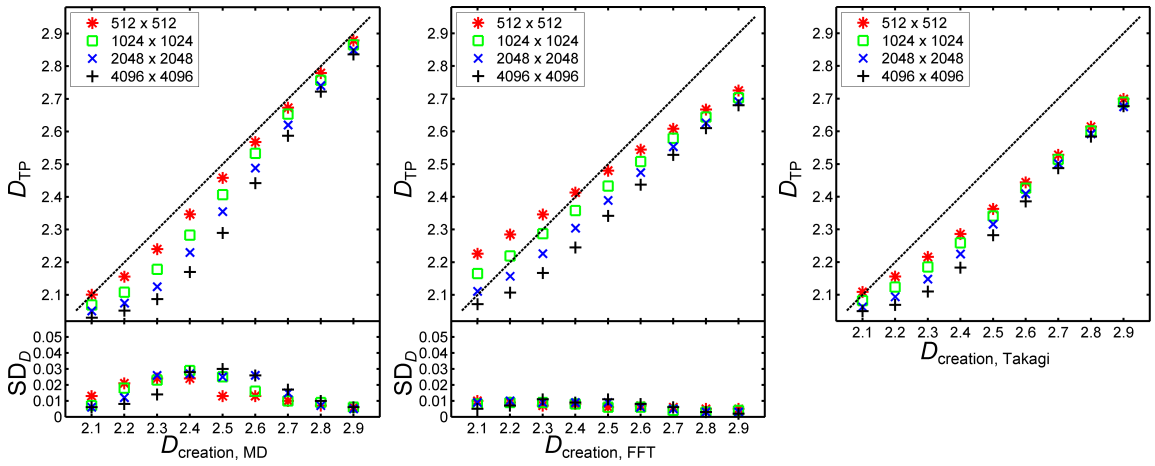

(a) MD **(b)** FFT **(c)** Takagi Surfaces

Figure 7.9.: Estimated D-values (D_{TP}) obtained by applying the TPM to grey value images created with MD (a), FFT (b) and Takagi Surfaces (c). For (a) and (b) D_{TP} denotes the mean value, the standard deviation SD is also shown for these generators. For the TPM an optimum scale-range of $s_{\mathrm{TP,opt}} = 2^0 - 2^3$ was found and used to obtain the shown results. The diagonal line represents theoretical D-values.

7.2.1.6. Pyramid Triangular Prism Method

The optimum scale-down factor ranges for the PTPM over all image sizes and generators were found to be $s_{n,\mathrm{PTP,opt}}^{\mathrm{bicubic}} = 2^0 - 2^3$ (bicubic interpolation), $s_{n,\mathrm{PTP,opt}}^{\mathrm{bilinear}} = 2^0 - 2^4$ (bilinear interpolation), and $s_{n,\mathrm{PTP,opt}}^{\mathrm{nearest}} = 2^0 - 2^3$ (nearest neighbour interpolation). Figures 7.10, 7.11, and 7.12 show the (mean) values of the estimated D-values ((a)-(c)) together with the standard deviations SD ((a),(b)). Resulting slopes of the estimated D-values of MD and Takagi surface images are too flat for low D-values (< 2.4) for all interpolation methods and too steep for high D-values (> 2.4) for bicubic and bilinear interpolation. For FFT images the slopes obtained with bicubic and bilinear interpolation fit well the theoretical values. For all generators and interpolation methods, estimated D-values are in the region of theoretical values and increase for decreasing image sizes. SD values are in a range up to 0.045 for MD images and up to 0.025 for FFT images (bicubic, bilinear) while nearest neighbour interpolation yielded SD values of ≤ 0.035 (MD) and ≤ 0.010 (FFT). In the appendix A.2.6, Figures A.8-A.10 show the characteristics of the measures in exemplary log-log plots. The decaying behaviour for small values of s_n (best linear characteristics for nearest neighbour interpolation) changes to constant values for intermediate s_n-values, before it drops down again for higher s_n-values. In Tables A.8-A.10 the three best scale-down factor ranges for each image size are listed separately. The quality of the linear fit was low for all images, better for nearest neighbour interpolation (down to $R^2 = 0.91$) than for bicubic (down to $R^2 = 0.81$) or bilinear (down to $R^2 = 0.76$) interpolation, and being worse for larger images.

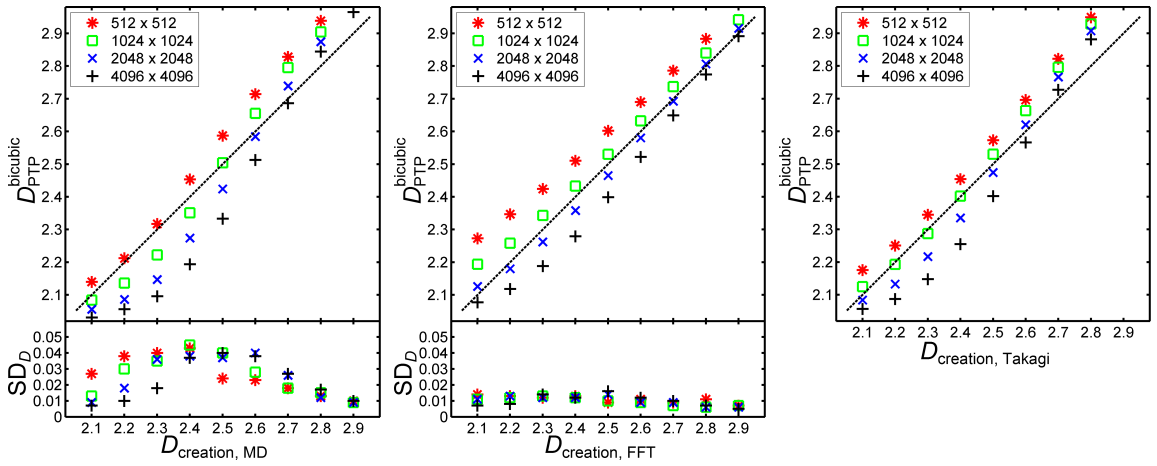

(a) MD **(b)** FFT **(c)** Takagi Surfaces

Figure 7.10.: Estimated D-values ($D_{\mathrm{PTP}}^{\mathrm{bicubic}}$) obtained by applying the PTPM with bicubic interpolation to grey value images created with MD (a), FFT (b) and Takagi Surfaces (c). For (a) and (b) $D_{\mathrm{PTP}}^{\mathrm{bicubic}}$ denotes the mean value, the standard deviation SD is also shown for these generators. For the PTPM with bicubic interpolation an optimum scale-down factor range of $s_{n,\mathrm{PTP,opt}}^{\mathrm{bicubic}} = 2^0 - 2^3$ was found and used to obtain the shown results. The diagonal line represents theoretical D-values.

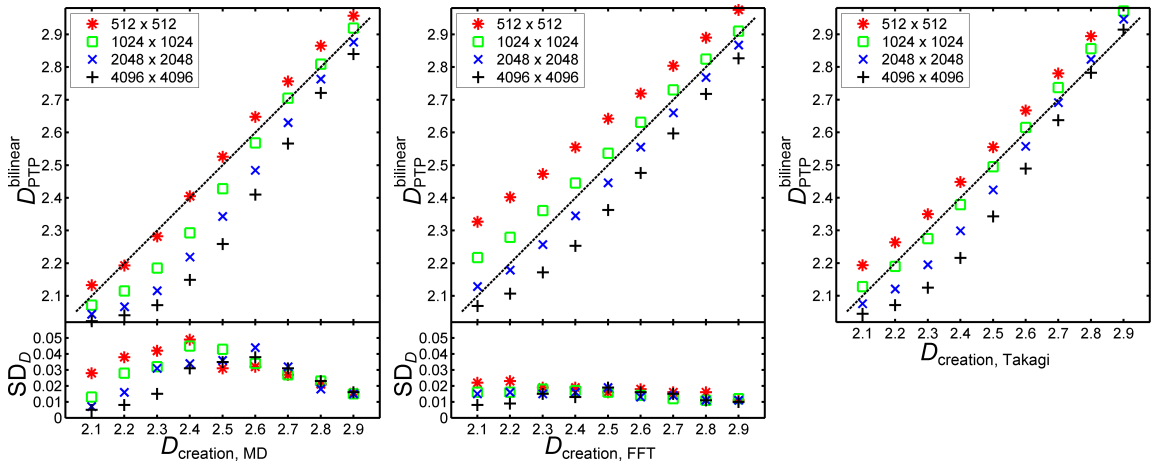

(a) MD **(b)** FFT **(c)** Takagi Surfaces

Figure 7.11.: Estimated D-values ($D_{\mathrm{PTP}}^{\mathrm{bilinear}}$) obtained by applying the PTPM with bilinear interpolation to grey value images created with MD (a), FFT (b) and Takagi Surfaces (c). For (a) and (b) $D_{\mathrm{PTP}}^{\mathrm{bilinear}}$ denotes the mean value, the standard deviation SD is also shown for these generators. For the PTPM with bilinear interpolation an optimum scale-down factor range of $s_{n,\mathrm{PTP,opt}}^{\mathrm{bilinear}} = 2^0 - 2^4$ was found and used to obtain the shown results. The diagonal line represents theoretical D-values.

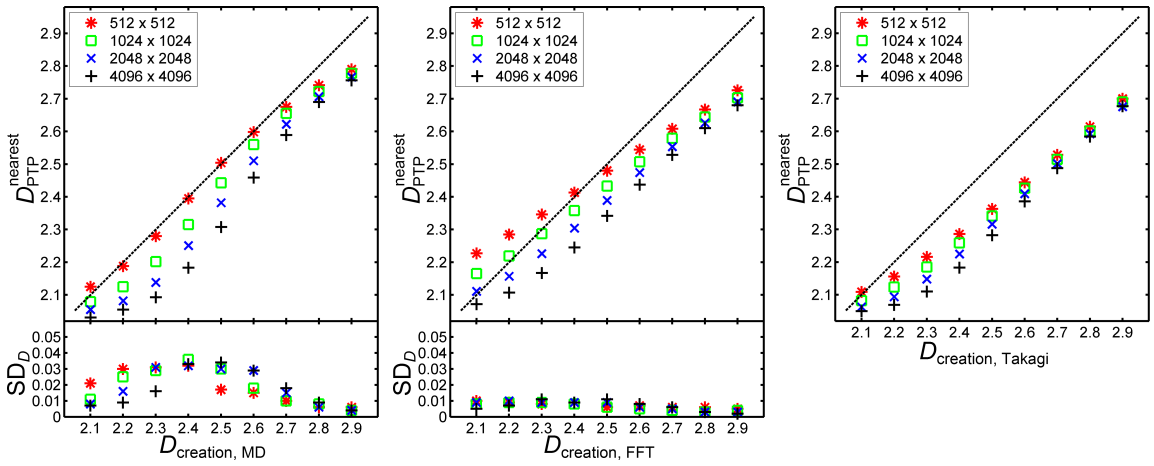

(a) MD **(b)** FFT **(c)** Takagi Surfaces

Figure 7.12.: Estimated D-values ($D_{\mathrm{PTP}}^{\mathrm{nearest}}$) obtained by applying the PTPM with nearest neighbour interpolation to grey value images created with MD (a), FFT (b) and Takagi Surfaces (c). For (a) and (b) $D_{\mathrm{PTP}}^{\mathrm{nearest}}$ denotes the mean value, the standard deviation SD is also shown for these generators. For the PTPM with nearest neighbour interpolation an optimum scale-down factor range of $s_{n,\mathrm{PTP,opt}}^{\mathrm{nearest}} = 2^0 - 2^3$ was found and used to obtain the shown results. The diagonal line represents theoretical D-values.

7.2.1.7. Pyramid Gradient Method

The optimum scale-down factor ranges for the PGM (simple kernel) over all image sizes and generators were found to be $s_{n,\mathrm{PG,opt}}^{\mathrm{simple}} = 2^0 - 2^3$ for all interpolation methods (bicubic, bilinear, and nearest neighbour). Figures 7.13, 7.14, and 7.15 show the (mean) values of the estimated D-values ((a)-(c)) together with the standard deviations SD ((a),(b)). Resulting slopes of the estimated D-values of MD and Takagi surface images are too flat for low D-values (< 2.4) for all interpolation methods.For FFT images the slopes obtained with bicubic and bilinear interpolation fit well the theoretical values. For all generators and interpolation methods, estimated D-values tend to be below theoretical values and increase with decreasing image sizes. SD values are in a range up to 0.050 for MD images and up to 0.025 for FFT images (bicubic, bilinear) while nearest neighbour interpolation yielded SD values of ≤ 0.040 (MD) and ≤ 0.015 (FFT). In the appendix A.2.7, Figures A.11-A.13 show the characteristics of the measures in exemplary log-log plots. Two regions showing linear decays with different slopes can be distinguished. Only the region of small s_n-values shows different slopes for images having different theoretical D-values. In Tables A.11-A.13 the best scale-ranges for each image size are listed separately. The quality of the linear fit was high ($R^2 > 0.99$)

for all images and all interpolation methods.

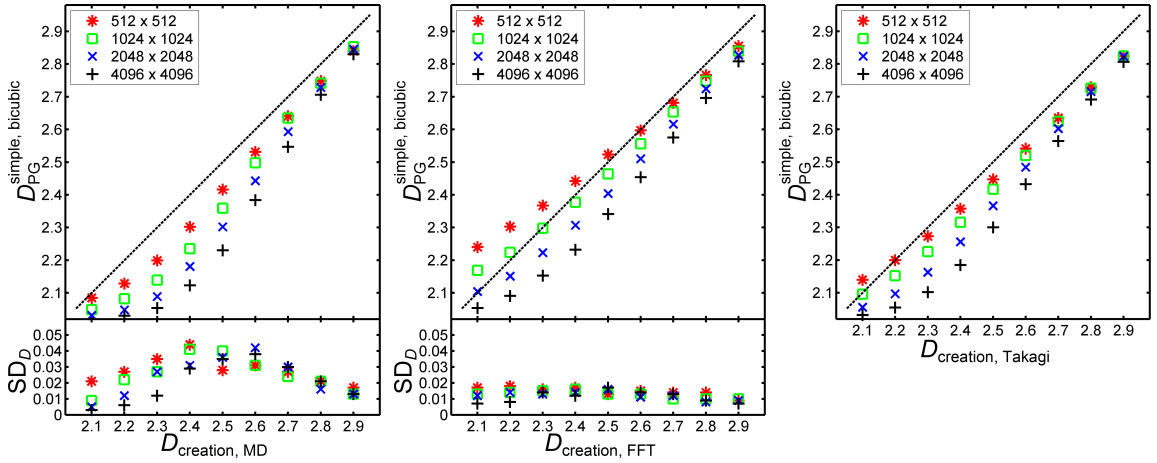

(a) MD **(b)** FFT **(c)** Takagi Surfaces

Figure 7.13.: Estimated D-values ($D_{\mathrm{PG}}^{\mathrm{simple,bicubic}}$) obtained by applying the PGM (simple kernel) with bicubic interpolation to grey value images created with MD (a), FFT (b) and Takagi Surfaces (c). For (a) and (b) $D_{\mathrm{PG}}^{\mathrm{simple,bicubic}}$ denotes the mean value, the standard deviation SD is also shown for these generators. For the PGM (simple kernel) with bicubic interpolation an optimum scale-down factor range of $s_{n,\mathrm{PG,opt}}^{\mathrm{simple,bicubic}} = 2^0 - 2^3$ was found and used to obtain the shown results. The diagonal line represents theoretical D-values.

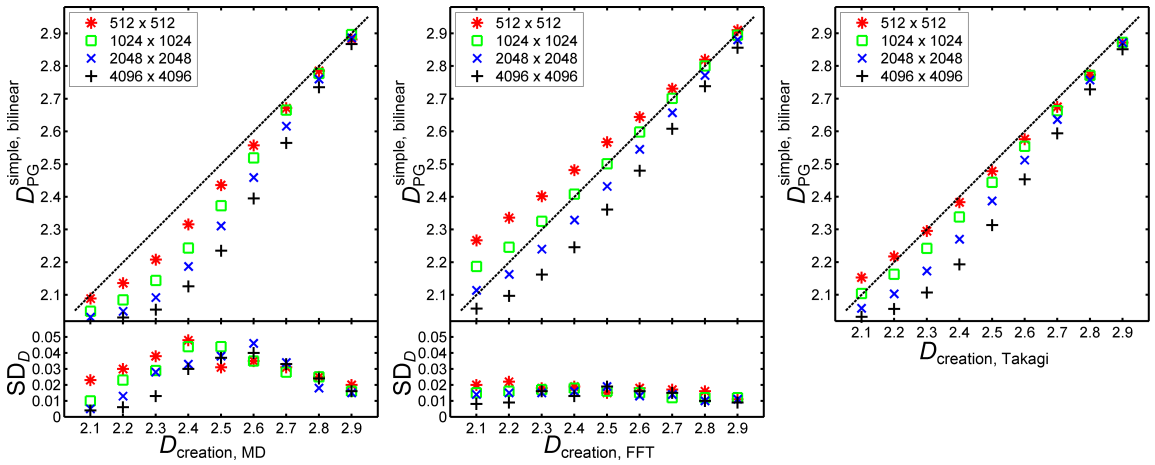

(a) MD **(b)** FFT **(c)** Takagi Surfaces

Figure 7.14.: Estimated D-values ($D_{\mathrm{PG}}^{\mathrm{simple,bilinear}}$) obtained by applying the PGM (simple kernel) with bilinear interpolation to grey value images created with MD (a), FFT (b) and Takagi Surfaces (c). For (a) and (b) $D_{\mathrm{PG}}^{\mathrm{simple,bilinear}}$ denotes the mean value, the standard deviation SD is also shown for these generators. For the PGM (simple kernel) with bilinear interpolation an optimum scale-down factor range of $s_{n,\mathrm{PG,opt}}^{\mathrm{simple,bilinear}} = 2^0 - 2^3$ was found and used to obtain the shown results. The diagonal line represents theoretical D-values.

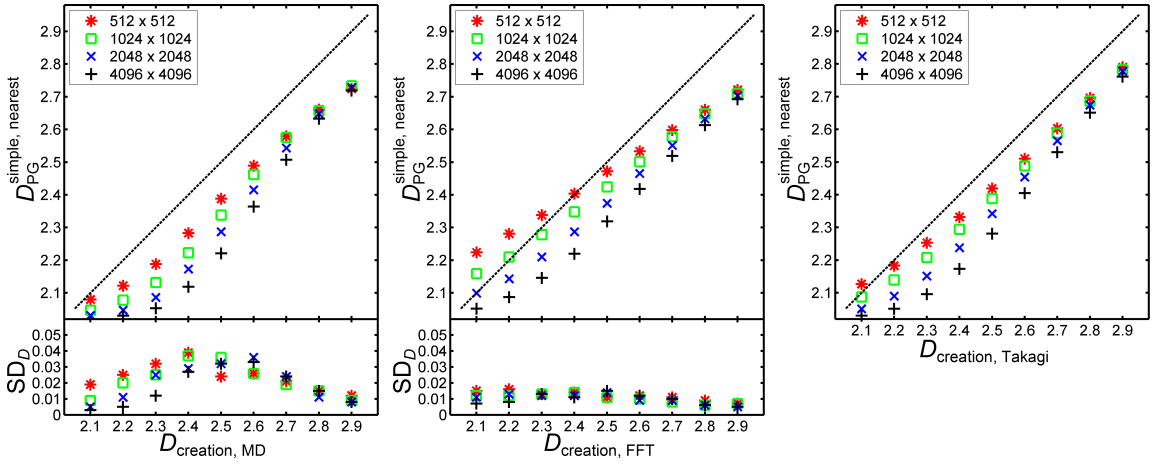

(a) MD **(b)** FFT **(c)** Takagi Surfaces

Figure 7.15.: Estimated D-values ($D_{\mathrm{PG}}^{\mathrm{simple,nearest}}$) obtained by applying the PGM (simple kernel) with nearest neighbour interpolation to grey value images created with MD (a), FFT (b) and Takagi Surfaces (c). For (a) and (b) $D_{\mathrm{PG}}^{\mathrm{simple,nearest}}$ denotes the mean value, the standard deviation SD is also shown for these generators. For the PGM (simple kernel) with nearest neighbour interpolation an optimum scale-down factor range of $s_{n,\mathrm{PG,opt}}^{\mathrm{simple,nearest}} = 2^0 - 2^3$ was found and used to obtain the shown results. The diagonal line represents theoretical D-values.

The optimum scale-down factor ranges for the PGM (Sobel kernel) over all image sizes and generators were found to be $s_{n,\mathrm{PG,opt}}^{\mathrm{sobel}} = 2^0 - 2^3$ for all interpolation methods (bicubic, bilinear, and nearest neighbour). Figures 7.16, 7.17, and 7.18 show the (mean) values of the estimated D-values ((a)-(c)) together with the standard deviations SD ((a),(b)). Resulting slopes of the estimated D-values of MD and Takagi surface images are too flat for low D-values (< 2.4) for all interpolation methods.For FFT images the slopes obtained with bicubic and bilinear interpolation fit better with the theoretical values. For all generators and interpolation methods, estimated D-values tend to be below theoretical values and increase with decreasing image sizes. SD values are in a range up to 0.045 for MD images and up to 0.025 for FFT images (bicubic, bilinear) while nearest neighbour interpolation yielded SD values of ≤ 0.040 (MD) and ≤ 0.020 (FFT). In the appendix A.2.7, Figures A.14-A.16 show the characteristics of the measures in exemplary log-log plots. Two regions showing linear decays with different slopes can be distinguished. Only the region of small s_n-values shows different slopes for images having different theoretical D-values. In Tables A.14-A.16 the best scale-ranges for each image size are listed separately. The quality of the linear fit was high ($R^2 > 0.99$) for all images and all interpolation methods.

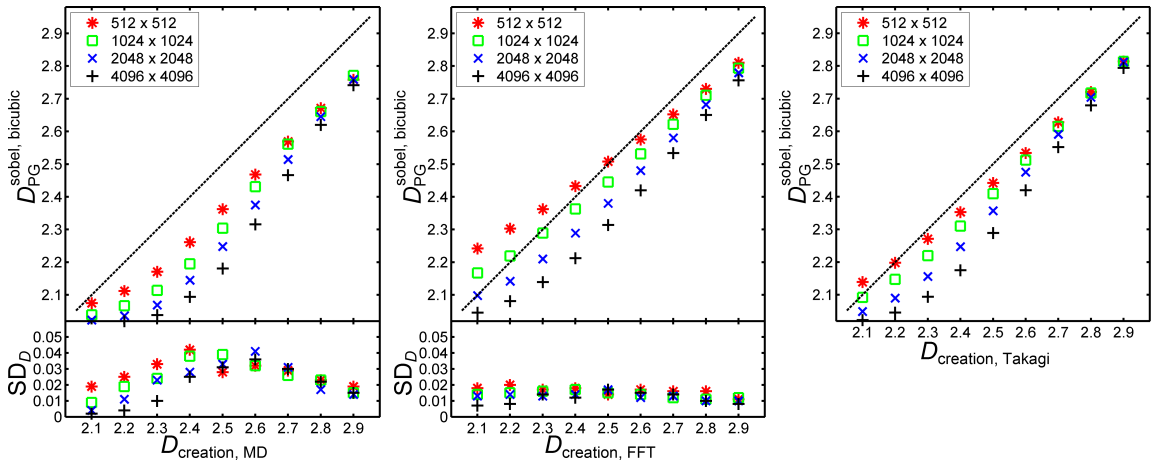

(a) MD **(b)** FFT **(c)** Takagi Surfaces

Figure 7.16.: Estimated D-values ($D_{\mathrm{PG}}^{\mathrm{sobel,bicubic}}$) obtained by applying the PGM (Sobel kernel) with bicubic interpolation to grey value images created with MD (a), FFT (b) and Takagi Surfaces (c). For (a) and (b) $D_{\mathrm{PG}}^{\mathrm{sobel,bicubic}}$ denotes the mean value, the standard deviation SD is also shown for these generators. For the PGM (Sobel kernel) with bicubic interpolation an optimum scale-down factor range of $s_{n,\mathrm{PG,opt}}^{\mathrm{sobel,bicubic}} = 2^0 - 2^3$ was found and used to obtain the shown results. The diagonal line represents theoretical D-values.

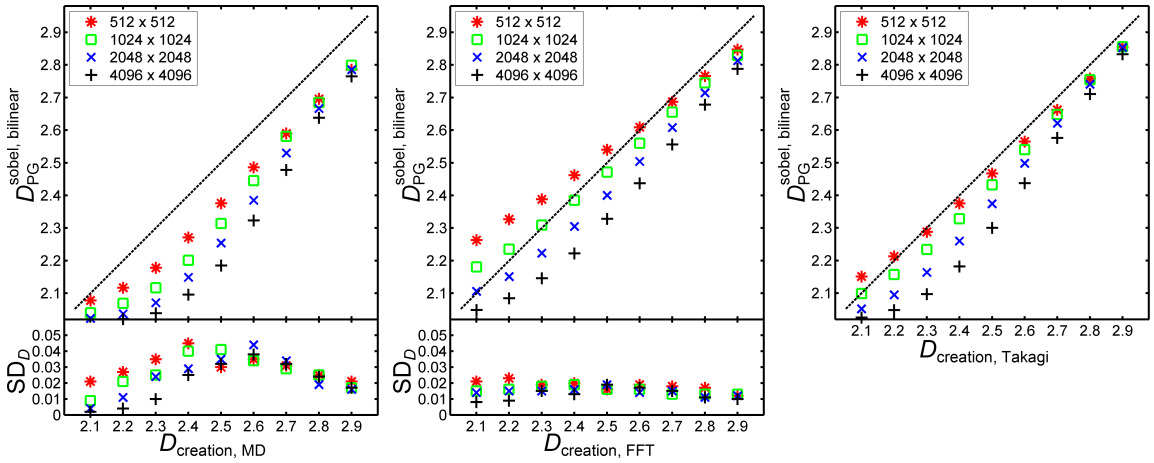

(a) MD **(b)** FFT **(c)** Takagi Surfaces

Figure 7.17.: Estimated D-values ($D_{\mathrm{PG}}^{\mathrm{sobel,bilinear}}$) obtained by applying the PGM (Sobel kernel) with bilinear interpolation to grey value images created with MD (a), FFT (b) and Takagi Surfaces (c). For (a) and (b) $D_{\mathrm{PG}}^{\mathrm{sobel,bilinear}}$ denotes the mean value, the standard deviation SD is also shown for these generators. For the PGM (Sobel kernel) with bilinear interpolation an optimum scale-down factor range of $s_{n,\mathrm{PG,opt}}^{\mathrm{sobel,bilinear}} = 2^0 - 2^3$ was found and used to obtain the shown results. The diagonal line represents theoretical D-values.

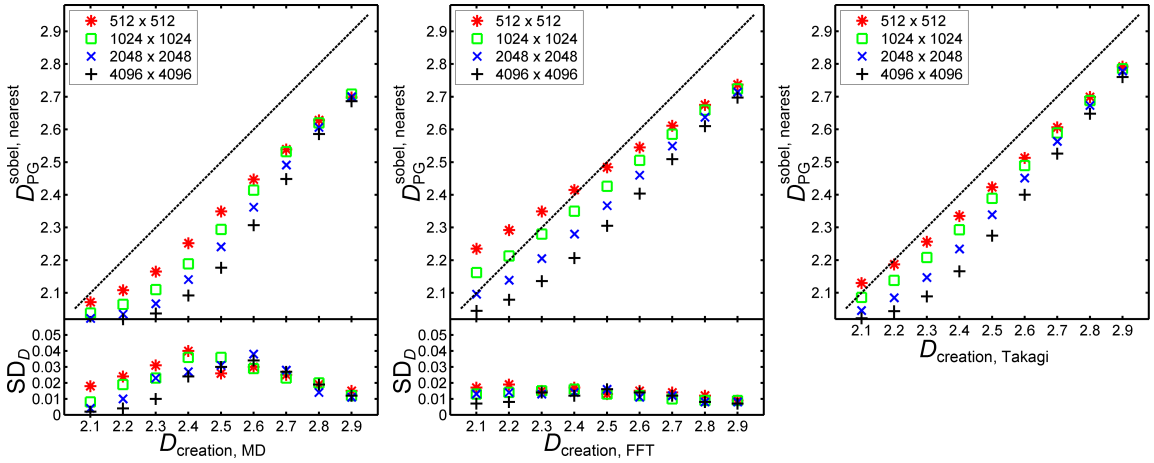

(a) MD **(b)** FFT **(c)** Takagi Surfaces

Figure 7.18.: Estimated D-values ($D_{\mathrm{PG}}^{\mathrm{sobel,nearest}}$) obtained by applying the PGM (Sobel kernel) with nearest neighbour interpolation to grey value images created with MD (a), FFT (b) and Takagi Surfaces (c). For (a) and (b) $D_{\mathrm{PG}}^{\mathrm{sobel,nearest}}$ denotes the mean value, the standard deviation SD is also shown for these generators. For the PGM (Sobel kernel) with nearest neighbour interpolation an optimum scale-down factor range of $s_{n,\mathrm{PG,opt}}^{\mathrm{sobel,nearest}} = 2^0 - 2^3$ was found and used to obtain the shown results. The diagonal line represents theoretical D-values.

7.2.1.8. Pyramid Differences Method

The optimum scale-ranges for the PDM over all image sizes and generators were found to be $s_{n,\mathrm{PD,opt}} = 1-4$ (bicubic and bilinear interpolation) and $s_{n,\mathrm{PD,opt}} = 1-5$ (nearest neighbour interpolation). Figures 7.19, 7.20, and 7.21 show the (mean) values of the estimated D-values ((a)-(c)) together with the standard deviations SD ((a),(b)). For all images the obtained slopes fit well with theoretical values for bicubic and bilinear interpolation, for nearest neighbour interpolation the slope for FFT and Takagi surface images are below theoretical values. The estimated D-values tend to be slightly above theoretical values, mostly for FFT images and for bicubic and bilinear interpolation. However, for these interpolations absolute D-values seem to converge towards theoretical values with increasing image sizes. SD values are in a range up to 0.035 for MD images and up to 0.025 for FFT images. In the appendix A.2.8, Figures A.17-A.19 show linear characteristics of the measures for higher s_n-values in exemplary log-log plots. In Tables A.17-A.19 the best scale-ranges for each image size are listed separately. The quality of the linear fit was high ($R^2 > 0.99$) for all images and all interpolation methods.

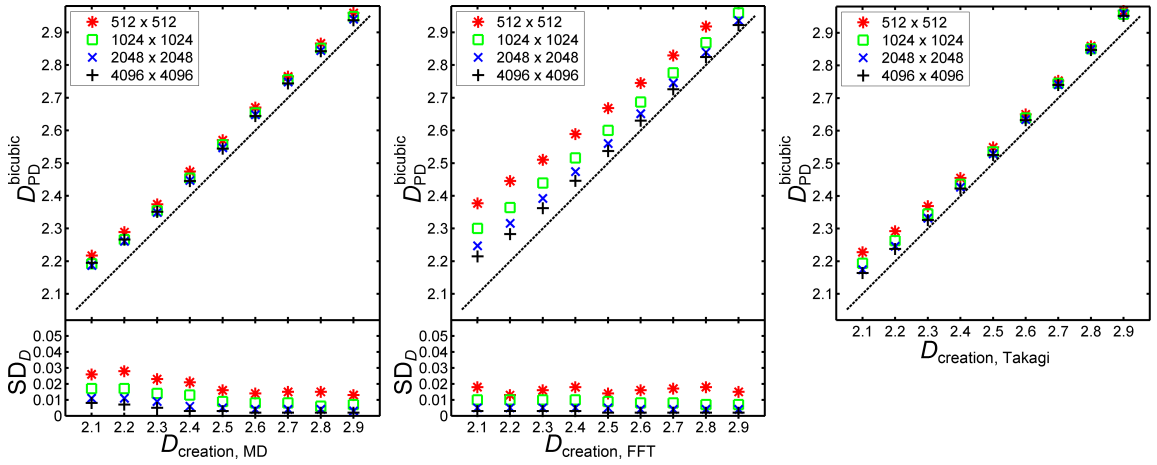

(a) MD **(b)** FFT **(c)** Takagi Surfaces

Figure 7.19.: Estimated D-values ($D_{\mathrm{PD}}^{\mathrm{bicubic}}$) obtained by applying the PDM with bicubic interpolation to grey value images created with MD (a), FFT (b) and Takagi Surfaces (c). For (a) and (b) $D_{\mathrm{PD}}^{\mathrm{bicubic}}$ denotes the mean value, the standard deviation SD is also shown for these generators. For the PDM with bicubic interpolation an optimum scale-down factor range of $s_{n,\mathrm{PD,opt}}^{\mathrm{bicubic}} = 2^1 - 2^4$ was found and used to obtain the shown results. The diagonal line represents theoretical D-values.

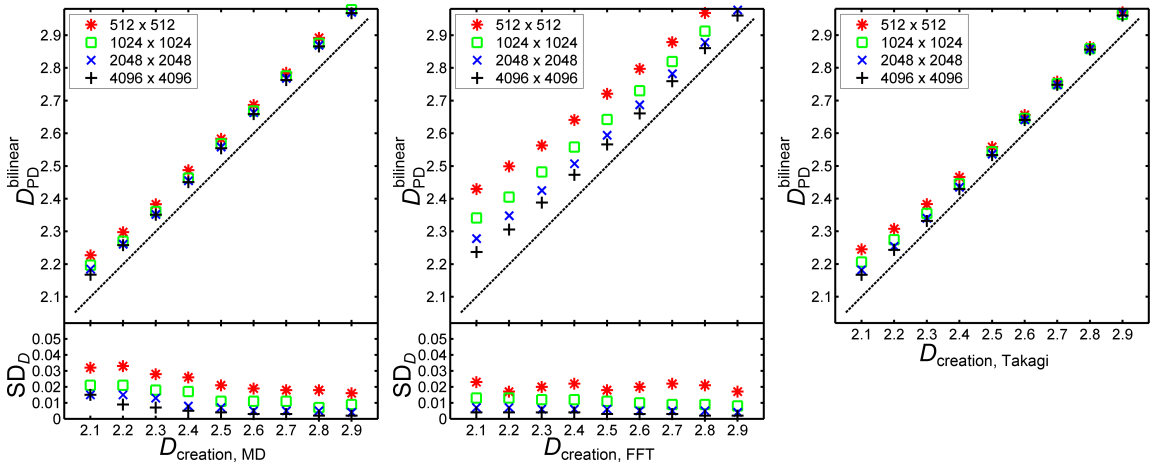

(a) MD **(b)** FFT **(c)** Takagi Surfaces

Figure 7.20.: Estimated D-values ($D_{\mathrm{PD}}^{\mathrm{bilinear}}$) obtained by applying the PDM with bilinear interpolation to grey value images created with MD (a), FFT (b) and Takagi Surfaces (c). For (a) and (b) $D_{\mathrm{PD}}^{\mathrm{bilinear}}$ denotes the mean value, the standard deviation SD is also shown for these generators. For the PDM with bilinear interpolation an optimum scale-down factor range of $s_{n,\mathrm{PD,opt}}^{\mathrm{bilinear}} = 2^1 - 2^4$ was found and used to obtain the shown results. The diagonal line represents theoretical D-values.

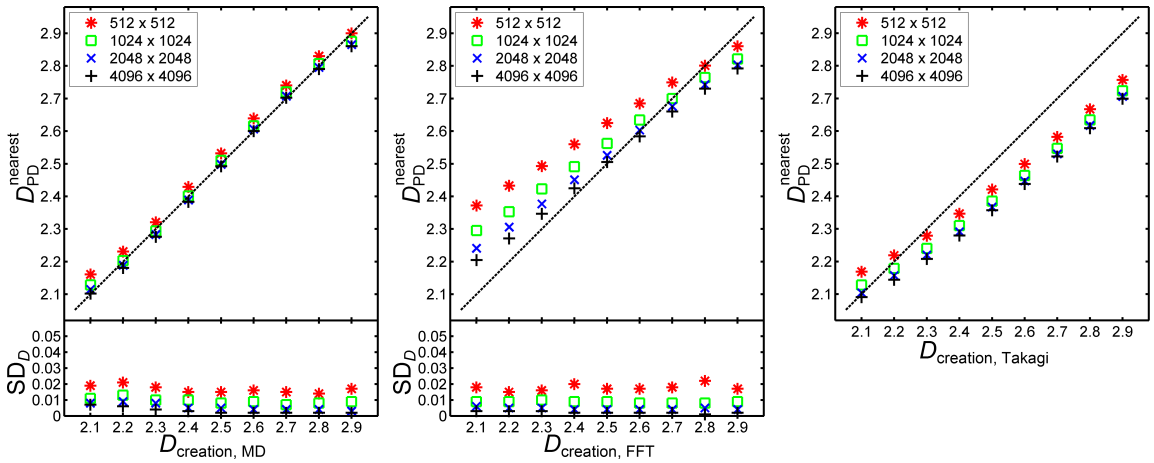

(a) MD **(b)** FFT **(c)** Takagi Surfaces

Figure 7.21.: Estimated D-values ($D_{\mathrm{PD}}^{\mathrm{nearest}}$) obtained by applying the PDM with nearest neighbour interpolation to grey value images created with MD (a), FFT (b) and Takagi Surfaces (c). For (a) and (b) $D_{\mathrm{PD}}^{\mathrm{nearest}}$ denotes the mean value, the standard deviation SD is also shown for these generators. For the PDM with nearest neighbour interpolation an optimum scale-down factor range of $s_{n,\mathrm{PD,opt}}^{\mathrm{nearest}} = 2^1 - 2^5$ was found and used to obtain the shown results. The diagonal line represents theoretical D-values.

7.2.2. Computational Time

The following figures show computational times for all implemented methods and investigated image sizes. All algorithms were implemented in Matlab (R2013a, 8.1.0.604, 64 bit) and the calculations were performed in serial computing on a standard workstation (Intel Pentium G840, 2.80 GHz, 8GB RAM, Windows 7 Enterprise 64 Bit). The results show the mean computational times per image based on a computation of 50 images. The error bars indicate standard errors of the means. For the new pyramidal methods results for different interpolation methods (bicubic, bilinear, nearest neighbour) are given.

Figure 7.22 shows the computational times for all scales described in section 6.2.2 for all investigated image sizes. All new pyramidal approaches are among the fastest methods for all image sizes. All times given in the following are based on an image size of 4096×4096 pixels. While the computational time for a single image with the PTPM ((3.7 ± 0.3) s) is approximately the same as with the TPM ((3.4 ± 0.3) s), the PGM ((0.91 ± 0.02) s) and PDM ((0.76 ± 0.02) s) are even faster than the fastest non-pyramidal method (Fourier Method ((1.68 ± 0.05) s)). The slowest algorithms are the Minkowski Blanket Method ((559 ± 14) s), the improved DBCM ((82 ± 2) s), and the HM ((21.3 ± 0.4) s).

For some methods not all scales have to be calculated to obtain high quality results. In Figure 7.23 the computational times for optimized scales (see previous section 7.2.1) for all investigated image sizes are depicted. While from the new pyramidal approaches only the PDM ((0.28 ± 0.01) s) becomes significantly faster, from the non-pyramidal approaches the improved DBCM ((0.75 ± 0.02) s) as well as the Minkowski Blanket (Peleg) method ((34 ± 1) s) are clearly faster for optimized scales. Again all times given in this paragraph are based on an image size of 4096×4096 pixels.

Figure 7.24 shows the computational times plotted as a function of the image size, again for all calculated scales (a) as well as for the optimized scales (b). The new pyramidal methods (red triangles), especially PGM and PDM, are faster compared to most of the non-pyramidal approaches (blue). For optimized scales (b) the improved DBCM (blue plus) is faster than PTPM and PGM, but still slower than PDM.

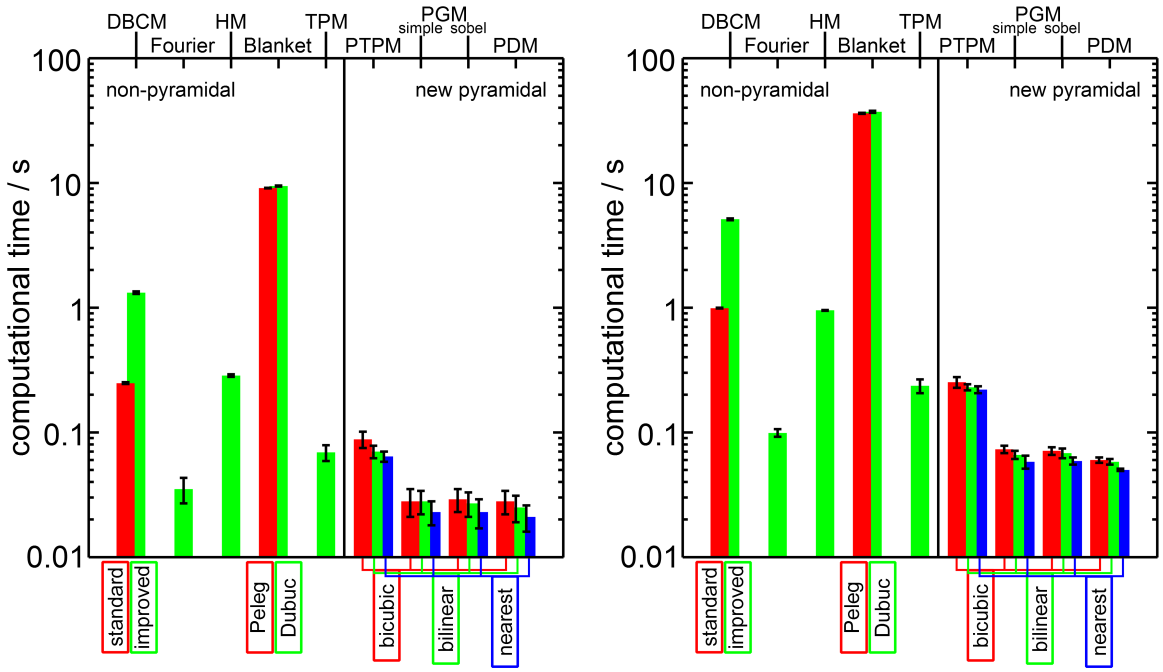

(a) image size: 512×512 (b) image size: 1024×1024

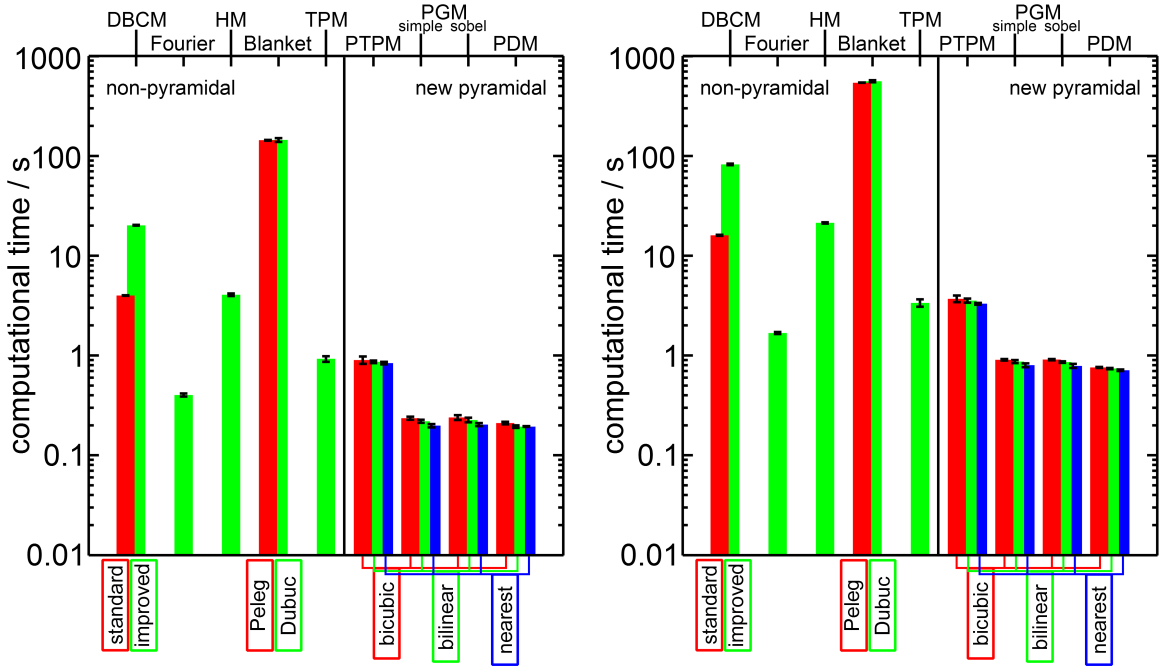

(c) image size: 2048×2048 (d) image size: 4096×4096

Figure 7.22.: Mean computational times per image (based on 50 images) for all implemented methods and all scales (described in section 6.2.2). The error bars indicate standard errors of the means. For the new pyramidal methods, results with different interpolation methods (bicubic, bilinear, nearest neighbour) are given. (a)-(d) show results for image sizes ranging from 512×512 pixels to 4096×4096 pixels.

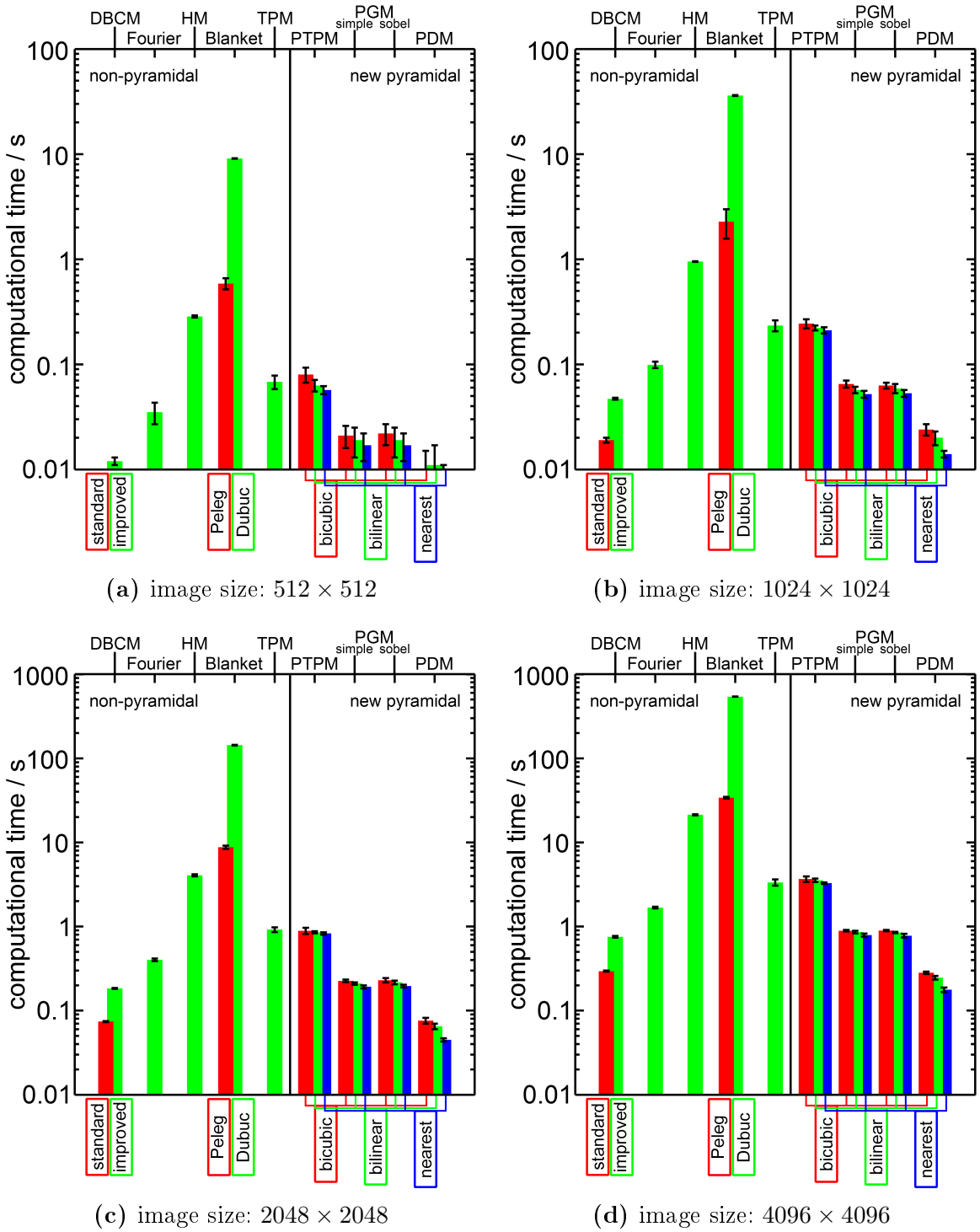

(a) image size: 512 × 512

(b) image size: 1024 × 1024

(c) image size: 2048 × 2048

(d) image size: 4096 × 4096

Figure 7.23.: Mean computational times per image (based on 50 images) for all implemented methods and optimized scales (see section 7.2.1). The error bars indicate standard errors of the means. For the new pyramidal methods, results with different interpolation methods (bicubic, bilinear, nearest neighbour) are given. (a)-(d) show results for image sizes ranging from 512 × 512 pixels to 4096 × 4096 pixels.

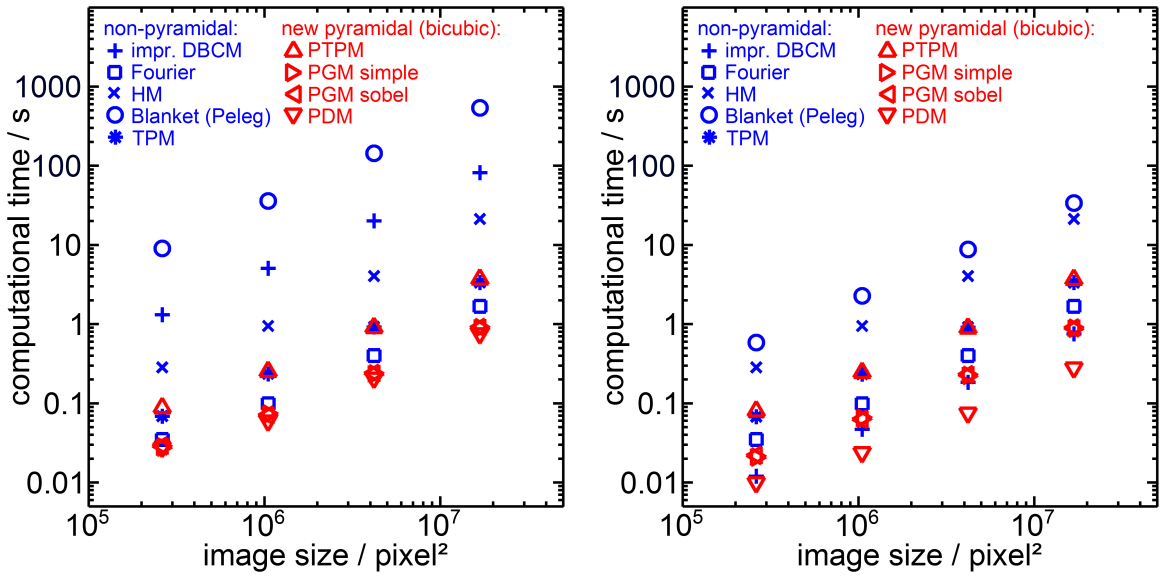

(a) All Scales **(b)** Best Scales

Figure 7.24.: Mean computational times per image (based on 50 images) for all scales (a) and optimized scales (b). For the new pyramidal methods (red triangles) only results for bicubic interpolation are shown. Note that markers for PGM (simple) and PGM (sobel) are superposed due to similar computational times.

7.2.3. Fractal Dimension Variation Range

The following Figures 7.25 - 7.28 show fractal dimension D variation ranges for all implemented methods and investigated image sizes for optimized scales. The dashed horizontal line indicates the optimum theoretical value of 0.8.

Although for some generator-image size combinations non-pyramidal methods (Fourier, TPM, Minkowski Blanket (Peleg)) perform well, the new pyramidal approaches show a more constant, high quality behaviour. For almost all generators and image sizes the new pyramidal methods perform best with bilinear interpolation, followed by the slightly worse bicubic interpolation and worst with nearest neighbour interpolation. All pyramidal methods with bilinear interpolation applied to larger images ($\geq 1024 \times 1024$ pixels) yielded D variation ranges between 0.7 and 0.87. The worst values for the pyramidal methods using bilinear interpolation are obtained for images generated with FFT and an image size of 512×512 pixels.

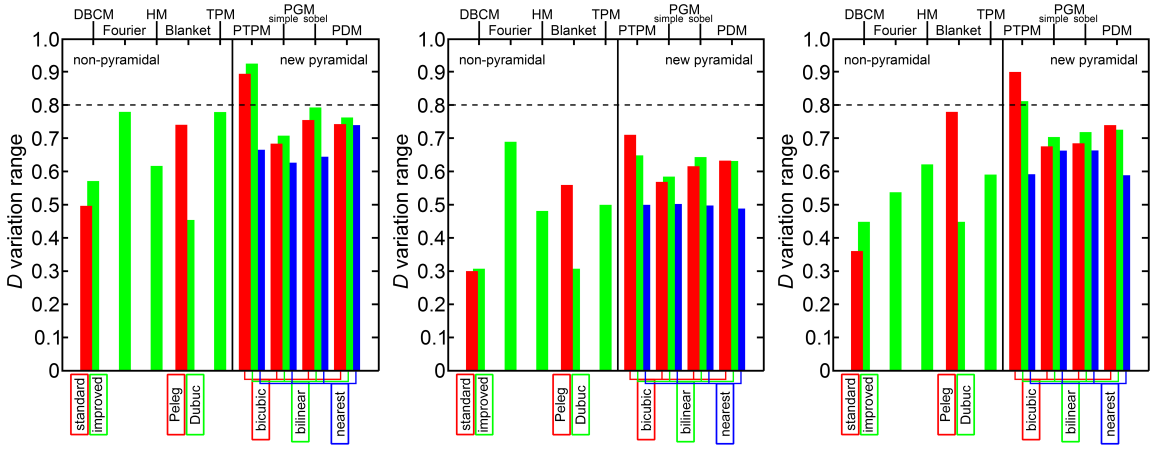

(a) MD (b) FFT (c) Takagi Surfaces

Figure 7.25.: D variation range for images with size 512×512 pixels created with MD (a), FFT (b) and Takagi Surfaces (c). The dashed horizontal line indicates the optimum theoretical value of 0.8.

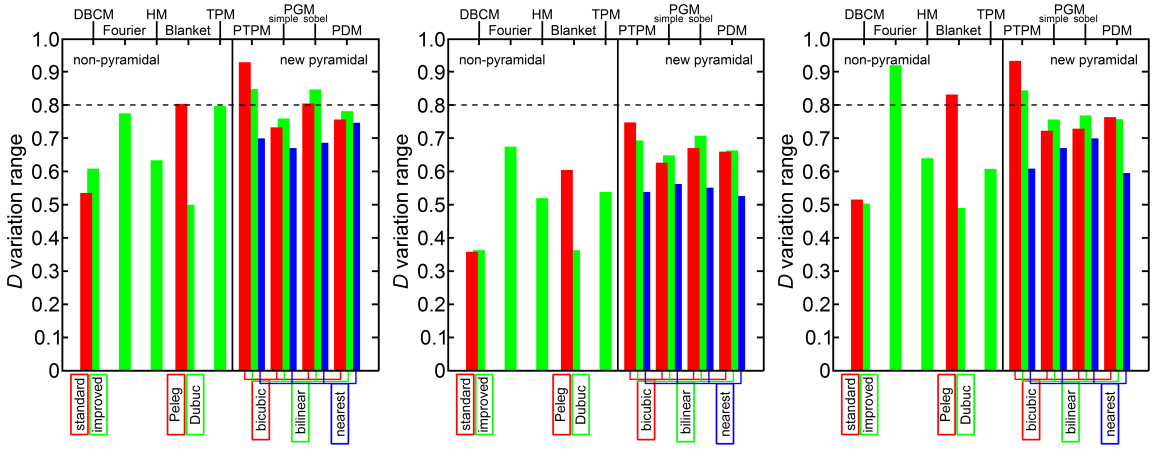

(a) MD (b) FFT (c) Takagi Surfaces

Figure 7.26.: D variation range for images with size 1024×1024 pixels created with MD (a), FFT (b) and Takagi Surfaces (c). The dashed horizontal line indicates the optimum theoretical value of 0.8.

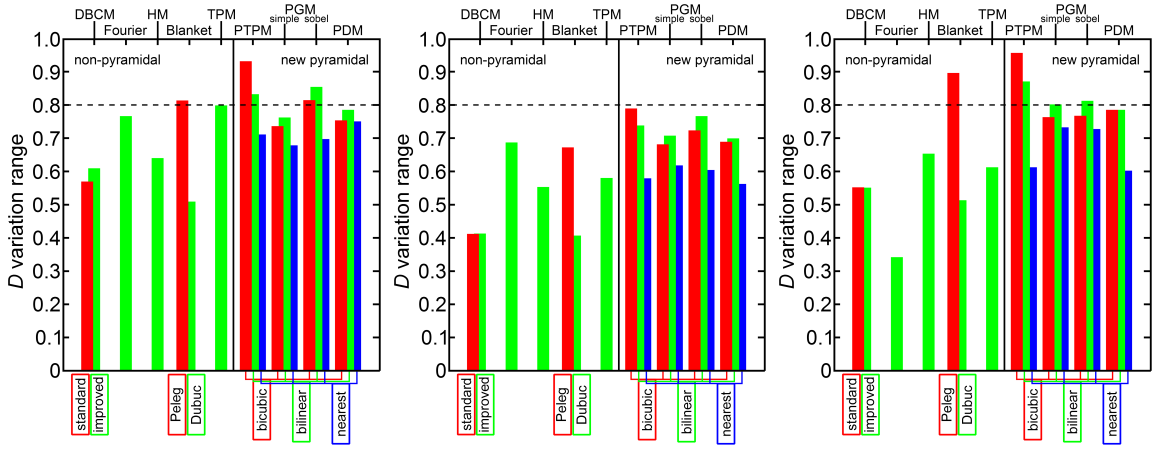

(a) MD (b) FFT (c) Takagi Surfaces

Figure 7.27.: D variation range for images with size 2048 × 2048 pixels created with MD (a), FFT (b) and Takagi Surfaces (c). The dashed horizontal line indicates the optimum theoretical value of 0.8.

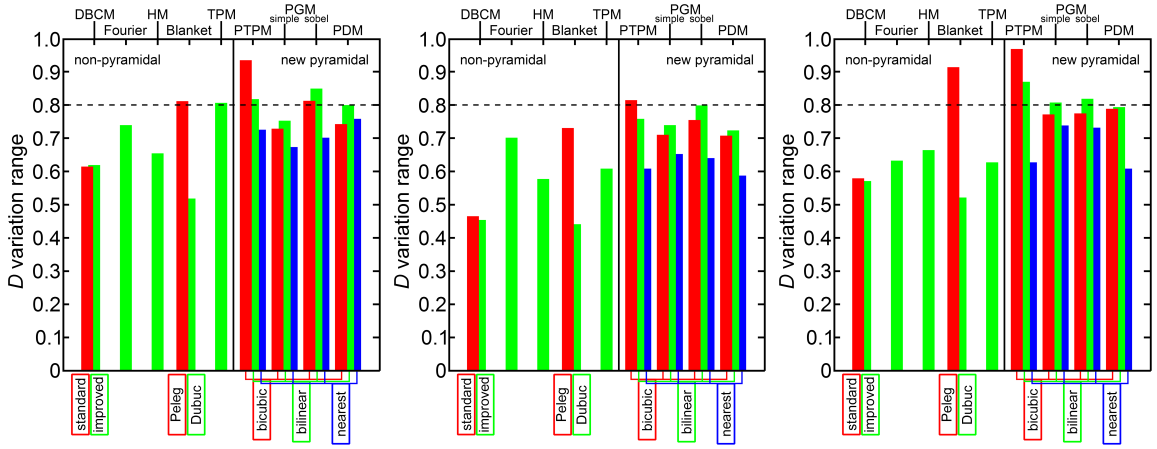

(a) MD (b) FFT (c) Takagi Surfaces

Figure 7.28.: D variation range for images with size 4096 × 4096 pixels created with MD (a), FFT (b) and Takagi Surfaces (c). The dashed horizontal line indicates the optimum theoretical value of 0.8.

8. Conclusion - Part I

The development of the binary PM acted as a starting point for the work on this thesis, hence it was compared to the well established binary BCM. For binary images the same accurate results were obtained with both investigated methods, in terms of computational time the PM was shown to be significantly faster (see Fig. 7.2). For high resolution whole-slide images (e.g. 50.000×50.000 pixels) the PM is able to calculate useful results within seconds, whereas an calculation with the BCM would last many minutes or even hours. This fact is of high relevance when considering applications in clinical practice. Concluding, it can be stated that for binary images PM is superior to BCM[2].

For fractal dimension (D) estimation of grey value images, three new pyramidal approaches were developed, namely the *Pyramid Triangular Prism Method* (PTPM), the *Pyramid Gradient Method* (PGM), and the *Pyramid Differences Method* (PDM). By using artificially created images based on three different methods (MD, FFT, Takagi Surfaces) and with sizes from 512×512 pixels up to 4096×4096 pixels, the new methods were compared to five standard, non-pyramidal approaches (DBCM, Fourier Method, 2D HM, Minkowski Blanket Method, and TPM). It was shown that all new pyramidal methods yield reasonable D-values in rather fast computational times. Three different interpolation methods for the downscaling of the images in order to create the image pyramids were tested. For all pyramidal methods *bicubic* and *bilinear* interpolation resulted in more accurate D-values than *nearest neighbour* interpolation.

All tested methods were optimized over all image sizes and generators by minimizing the root-mean-square deviation (RMSD) from the theoretical D-values. Best results were obtained with the PDM with bilinear interpolation, having a RMSD close to the best non-pyramidal methods (2D HM, improved DBCM) and a high quality of fit of the

linear regression model in the log-log plot. PDM yielded fastest computational times in addition to its high agreement with theoretical D-values and D variation ranges.

Concluding, the presented results verified the first hypothesis proposed in this thesis: *Fractal dimensions of grey value images can be reliably estimated by a pyramidal approach. This pyramidal approach has shorter computational times than standard approaches.*

Part II.

Histological Image Analysis

9. Myocardial Fibrosis

The second part of this thesis presents the application of image analysis, especially fractal methods to histological images of the heart in order to verify the second proposed hypothesis, which states that *"The estimated fractal dimension of histological images can be used as a parameter for a classification of different types of myocardial fibrosis"*.

In this chapter the medical fundamentals of myocardial fibrosis are presented. It starts with a brief description of the human heart and the cardiac interstitial space. Then the (pathological) occurrence of fibrosis in the cardiac structure is summarized. Furthermore, the four different types of fibrosis appearing in this thesis are introduced. In the last part of this chapter, invasive as well as non-invasive techniques for imaging of cardiac tissue, especially fibrosis are presented.

9.1. The Human Heart

The human heart can be seen as an electrically driven mechanical pump that has the task to pump blood into the body and to the lung. It is a muscular organ that comprises four cavities, namely the right and left atrium and the right and left ventricle. Low-oxygen blood fills the right atrium through two caval veins (superior, inferior). From there the blood is transported through the tricuspid valve to the right ventricle. The right ventricle pumps it into the lungs. There the blood is re-oxygenated. Through the pulmonary veins the now high-oxygen blood comes back to the heart, entering the left atrium. After passing the bicuspid valve, the left ventricle pumps it into the aorta and the blood is distributed over the whole body[114,115].

The heart muscle (cardiac muscle) is one of three different types of muscles, the others being skeletal muscles and smooth muscles. It can be specifically found in the *myocardium*. The myocardium is the middle layer in the heart walls that is responsible for pumping out the blood by contracting the heart[116].

9.1.1. The Cardiac Interstitial Space

Cardiomyocytes or *cardiac muscle cells* are the main components of cardiac tissue. They are surrounded by the extracellular matrix (ECM). Cardiac cells, blood vessels and nerves are embedded in a rather complex three-dimensional space, which is called cardiac interstitium. This dynamic environment is essential for normal function of the heart[117]. In the physiological case, the ECM consists mainly of collagen scaffolding of collagen type I ($\approx$ 80%) and type III ($\approx$ 11%). Besides a ground substance of proteoglycans and glycosaminoglycans, among others fibroblasts and immune cells are contained in the matrix[117–120]. The contained fibroblasts, which represent up to 60% of the total myocardial cell population in some species, are morphologically different to fibroblasts in other organs and form a communication and structural support network, which parts are coupled by gap junctions (mostly connexin 43 and 45)[121,122]. Maintenance of the interstitium is provided by the relationship between itself, myocytes, cardiac fibroblasts, the neuro-hormonal system and mechanical forces[123]. A constant process of collagen and tissue turnover, i.e. growth and reparation, is present within these matrices[124].

9.2. Fibrosis in the Heart

A change of the interstitial status may be induced by a disease, (mechanical) stress, inflammation or the hormonal environment. Fibroblasts are metaplased into myofibroblasts, which results in a, compared to type III collagen, relatively higher amount of type I collagen and more fibre cross-linking. Early changes of the composition and structure of the interstitium may be physiological due to a response to current demands. However, persisting and combined changes alter myocardial properties (e.g. conduction) and may lead to arrhythmia and functional impairment and further to morbidity and mortality. Especially an excess of the synthesis and deposition of (type I) collagen seems to play a major role in the enhancement of myocardial fibrosis that

accompanies the appearance of heart failures. The type and hence also the pattern of the occurring fibrosis is partly disease specific[8,117,125,126].

Although the alterations due to fibrosis seem quite destructive, the pathological processes are not necessarily irreversible[127,128]. The complex pathways in fibrotic remodeling are more and more investigated and understood, providing a broad range of potential therapeutic targets[117].

From the functional point of view, two types of fibrosis are distinguished, *reactive* and *replacement* fibrosis. The latter, which is also called reparative fibrosis, occurs when dead cardiac cells are replaced by collagen. On the other hand, reactive fibrosis develops without cell loss, e.g. because of an increased mechanical load.[129]. Besides this differentiation due to the underlying function, a classification due to the morphology (shape) of the fibrosis can be done and is described in the following section.

Besides these well known facts, open questions regarding fibrosis and its influence on impulse propagation, especially on a microscopic level, still remain. Based on a mouse model it has been suggested that fibrosis in the aged heart is a significant parameter for arrhythmia. Furthermore, the texture of fibrosis influences the incidence of arrhythmias[8,9] . Considering the facts above a deeper understanding of the connection between electrical excitation spread and the amount, distribution and type of fibrosis is highly desirable. In particular, the investigation of local morphological differences at microscopic scales would be of high interest for the scientific community in order to assess the vulnerability for arrhythmias.

9.2.1. Types of Fibrosis

Different classification systems for myocardial fibrosis exist[8,117,125]. In the following the four most often used classes are briefly described, examples are shown in Figure 9.1.

- **Compact (focal)** fibrosis (see Figure 9.1a) mainly consists of regions showing dense collagen, free from any myocardial tissue. Despite its appearance it is the least arrhythmogenic compared to the other types[125 117 8].
- **Interstitial** fibrosis (see Figure 9.1b) consists of collagen tissue comprising the extracellular matrix. It shows a typical anisotropic pattern and may separate myocardial bundles. With increasing amount of interstitial fibrosis propagation becomes asynchronous perpendicular to the fibre direction[125 117 8]. It has been found that a high amount of this type predicts ventricular arrhythmias[130].
- In **diffuse** fibrosis (see Figure 9.1c) the short stretches of collagen intermingle with myocardial tissue. It was found that conduction velocity was significantly decreased proportional to the amount of diffuse fibrosis[8].
- The characteristics of **patchy** fibrosis (see Figure 9.1d) are areas where myocardial tissue (bundles) and collagen intermingle. In patchy fibrosis the collagen fibers create long strands. Large conduction delays can be caused by this type due to zig-zag conduction between the myocardial bundles. Hence it is very vulnerable to arrhythmias.[117 8,129]

For the work of this thesis the above classification system was used. Hence the observed types of fibrosis was assigned to the four classes *compact*, *interstitial*, *diffuse*, and *patchy* fibrosis. However, it has to be noted that fibrosis typically does not exhibit only one particular pattern type but may be a composition of the different types. Due to this fact it is obvious that although fibrosis is often classified, a uniform and exact classification of different types of fibrosis is debatable.

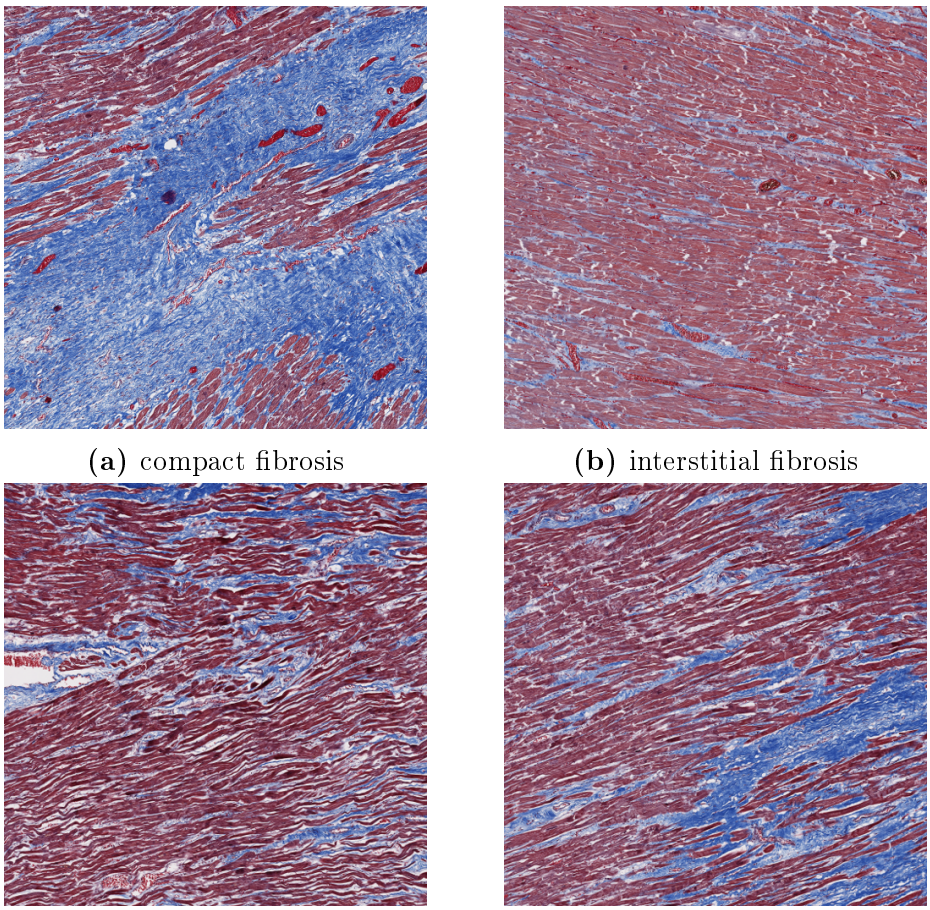

(a) compact fibrosis **(b)** interstitial fibrosis

(c) diffuse fibrosis **(d)** patchy fibrosis

Figure 9.1.: Classification system for myocardial fibrosis that was used in this work. Exemplary images of the four different types were taken from the ground truth images of image set IIb (see chapter 10.1.2). The histological sections were stained with Gieson's Trichrome (collagen: blue, muscle fibres: red), the areas of the shown regions are approximately 2 mm × 2 mm.

9.2.2. Imaging of Fibrosis

As a prerequisite for the characterization of fibrotic tissue, an image of the investigated region has to be obtained. This can either be done by invasive or non-invasive techniques, the most common in the context of fibrosis analysis are described below. In these images, the components of interest (e.g. the collagen in the case of fibrosis) should be intensified before further analysis.

9.2.2.1. Invasive Techniques

Biopsies of cardiac tissue can be taken with catheters or during surgery. An advantage of these techniques is that detailed information about the remodeling (structural and electrical) is achievable. The disadvantages are the risks for the patient and that only information on a very localized region of the heart is obtained[129].

- **Histology**
  For a histological analysis the tissue is frozen or embedded in paraffin. Thereafter, the sample is cut in $4-10\ \mu m$ thick sections. Mostly a trichrome dye (e.g. Masson's Trichrome[131] (collagen: blue, myocytes: red)) or Picrosirius Red[132–134] (collagen: red, myocytes: yellow) are used as cheap dyes to stain the sections and enhance the contrast between collagen and other tissue. Furthermore, Picrosirius Red can enhance the intrinsic birefringence of mature collagen, hence polarized light can be used to visualize the collagen fibres better and in more detail[129,135,136].
  Daunoravicius et al.[137] showed that Masson's trichrome could be used for an automated quantification of myocardial fibrosis by image analysis techniques. The analysis of digital images obtained by scanning histological sections was also the method of choice for the work of this thesis.

- **Immunohistology**
  Also fluorescent labeled antibodies can be used for specific collagen protein investigations with immunohistology or with a Western blot. However, this is more time-consuming or more expensive, hence this method is less frequently used[129].

- **Hydroxyproline Assay**
  The structure of mature collagen is stabilized by the modified amino acid hydroxyproline. Since collagen contains $\approx 14\%$ hydroxyproline, the determination of hydroxyproline (with commercially available kits) is highly specific for collagen and the actual amount can easily be calculated. A disadvantage of this method is

that homogenized tissue samples are required, hence no site-specific information is provided[129,138].

- **Sircol Assay**
  With this method it is possible to measure only newly formed collagen. Although this analysis can be easily performed, this assay also does not provide information on potential heterogeneity[129,139].

- **CNA35**
  Fluorescent labels, which are attached to the truncated bacterial protein CNA35, can be used due to the binding of CNA35 to collagen. Reversible binding and the smaller size of CNA35 compared to antibodies are advantages of this technique. Also MRI (magnetic resonance imaging) tagged labels can be used instead of fluorescent labels[129,140].

9.2.2.2. Non-invasive Techniques

Since the risks for the patients are nearly negligible, non-invasive techniques for an analysis of cardiac fibrosis would be preferable. However, quantitative analysis with these techniques are not completely validated so far.

- **Biomarkers in the Blood**
  Biomarkers which have their origin in the breakdown of the collagen (matrix metalloproteases (MMPs), tissue inhibitors of metalloproteases (TIMPs), Pyridinoline cross-linked carboxyterminal telopeptide (ICTP)) can be detected in blood samples. This method has the advantages of being cheap, non-invasive, and easily applicable in a clinical setting. However, the circulating peptides are not cardiac-specific and no validation of a quantitative analysis of cardiac fibrosis with these biomarkers is available[129,141].

- **MRI / CMR**
  The technique of cardiovascular magnetic resonance imaging (CMR) has become the gold standard for the non-invasive characterization of myocardial tissue[142,143]. The clinical investigation of cardiac scar tissue is often done by late gadolinium enhanced (LGE) magnetic resonance imaging (MRI). The gadolinium is used for the contrast agent, which remains shorter in viable than in scarred tissue due to different washout kinetics[144]. Hence, it is an indirect measurement for collagen deposition. Recently, an MRI technique called ultrashort echo time (UTE) was

developed to detect myocardial fibrosis without using contrast agents[145]. However, due to the current limitations of the achievable resolutions with MRI, for instance interstitial or small patches of fibrosis are undetected or unresolved. This is an important drawback since they are of particular interest because of their role in arrhythmia susceptibility and systolic dysfunction[117,129,146,147].

- **2D strain imaging by speckle-tracking echocardiography (STE)**
  This technique uses ultrasonic sound waves to measure the tissue motion in the heart. The produced acoustic reflections are called *speckles* and can be used to measure the strain, i.e. the change in an objects dimension. These strain measurements can be used to make conclusions about whether fibrotic tissue is present in the heart[148–150]. 2D strain imaging by speckle-tracking echocardiography produces images with coarse resolution hence no accurate morphometric analysis is possible.

10. Material

In this chapter, the histological image sets are described, to which the fractal analysis methods introduced in part I were applied. One image set was used to differentiate between control and fibrosis groups, a second more extensive image set was used to distinguish between different types of fibrosis.

10.1. Histological Images

For diagnosing different types of myocardial fibrosis in histological samples, pathologists typically use magnifications in the range of $1\times - 5\times$, typical investigated areas for classifying fibrosis are in the range of $1 - 4\ \mathrm{mm}^2$. In the following, a detailed description of the image sets used for this work is given.

10.1.1. Image Set I

A first set of images was provided by our partner group of the University of Extremadura in Badajoz, Spain[1].

The images show different regions of 14 different human hearts, namely parts of the papillary muscles (anterior and posterior) and the interventricular septum. The diagnosis for all patients was structural ischemic heart disease. The tissue for investigation was impregnated with paraffin wax, then sections ($7\ \mu m$) were cut on a microtome. A trichrome staining protocol was used to enhance contrast between different tissue types (myocytes and connective tissue). With the used staining method collagen was coloured

[1] contact person: Damián Sánchez-Quintana, Departamento de Anatomía y Biología Celular, Facultad de Medicina, Universidad de Extremadura

blue, muscle fibres red and erythrocytes orange. Since no healthy control hearts were available, from each heart up to two slices showing nonfibrotic regions were chosen and assigned to the *control group*. Furthermore, one or two slices showing fibrotic regions were chosen and assigned to the *fibrosis group*. The set contained 40 different images (20 control, 20 fibrosis), all images were in the TIF(F) file format (uncompressed, 24-bit true colour RGB space) and had a resolution of 2560×1920 pixels. A stereomicroscope (Nikon model SM 1500, $5\times$ magnification) was used for digitalization. The spatial resolution, i.e. the pixel size was $0.68\ \mu\text{m} \times 0.68\ \mu\text{m}$[151].

In the following these images are referred to as *image set I*. It was used in a first step of the work to test algorithms for segmentation and differentiating fibrotic and non-fibrotic regions.

10.1.2. Image Set IIa and IIb

A second set of images was obtained by using samples of formalin-fixed, paraffin-embedded (FFPE) human myocardium that had been stored after routine autopsies by the Biobank Graz. Access to these samples in the context of this study was approved by the ethics committee of the Medical University of Graz (EK-no: 26-315 ex 13/14). Together with an expert[2] 25 samples containing fibrotic tissue were selected. From these samples, sections with a thickness of $3\ \mu\text{m} - 4\ \mu\text{m}$ and lateral sizes of approximately $(22 - 37)\ \text{mm} \times (20 - 25)\ \text{mm}$ were cut on a microtome.

Two subsets of images were created from these histological sections: For *image set IIa* the samples were stained with *Picrosirius Red* (for the staining protocol see appendix A.1.1). Collagen appeared in a bright red with this technique, muscle fibres in orange to yellow. *Image set IIb* was created by using the stain *Gieson's Trichrome*, that brought out the collagen in blue while muscle fibres were coloured red (for the staining protocol see appendix A.1.2).

All samples were digitized with the *Aperio ScanScope® AT* whole-slide imaging scanner. A $40\times$ magnification was used to produce images with sizes of about $(90,000 - 150,000) \times (80,000 - 100,000)$ pixels, depending on the size of the section under investigation. At this resolution the pixel size was approximately $0.245\ \mu\text{m} \times 0.245\ \mu\text{m}$. The images were saved in the SVS file format (see section 2.2.3.4), using TIFF files with JPEG-2000 compression (see sections 2.2.3.2 and 2.2.3.3).

[2] Dr. Martin Asslaber, Institute of Pathology, Medical University of Graz

For further diagnosis and processing, the whole scans were split into tiles with sizes of 8192 × 8192 pixels and saved separately (see Figure 10.1). The *Matlab Toolbox for OpenSlide*[14,15] was used for opening the SVS-files created by the *Aperio* whole-slide scanner. Each new image showed an area of approximately 2 mm × 2 mm, which is a common size for a classification of different types of fibrosis.

For testing automated classification algorithms for different types of fibrosis, the obtained results had to be compared to diagnoses of human experts (see subsequent chapter 11.1). Since expert classification of all images would have been too laborious, subsets of image sets IIa and IIb were used to test the proposed approaches. For the work presented in this thesis, a random selection of 70 images of set IIa was used.[3] Image set IIb included a selection of 110 images of set IIb.[4] The main number of these 110 images showed cuts from a single whole-slide scan, i.e. a single histological section, that was tiled in 99 squared images (see Figure 10.1).

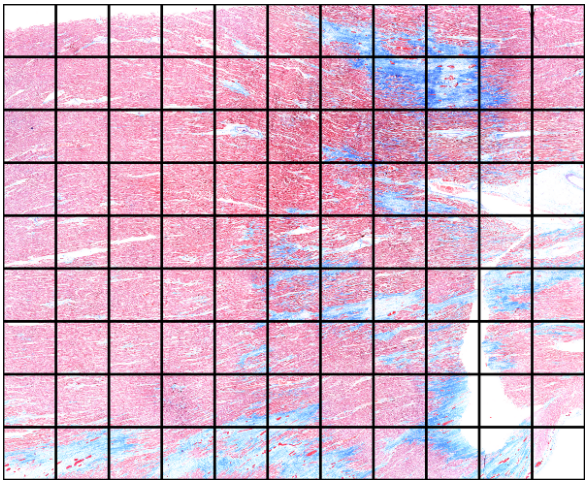

Figure 10.1.: Tiled single whole-slide scan of image set IIb. The scan was divided into 99 single images.

[3] In the following chapters the term *image set IIa* refers to these 70 images.
[4] In the following chapters the term *image set IIb* refers to these 110 images.

11. Methods and Experimental Setup

In this chapter, the proposed methods for an automated classification of different types of fibrosis from histological images are described. The setup for an inter-observer study to obtain inter-rater reliability that acted as a reference for the proposed automated classification is given. Furthermore, the procedures used for fractal dimension estimation and classification are outlined. Obtained results and the corresponding interpretation are presented in subsequent chapters.

11.1. Inter-rater Reliability

Whenever a new method for solving a certain task is proposed, it has to be compared to a reference method. Usually it is compared to the current gold-standard, i.e. the best method known so far. In the case of classification of several types of myocardial fibrosis, gold-standard is the classification by a human expert. However, it is important to not only compare with the results obtained by one particular observer alone. The fact that different experts may not agree completely in every case of a classification is called *inter-observer variability*. So in a first step, a measure for the agreement between the results of two or more experts has to be found. This measure is called *inter-rater reliability* or *inter-rater agreement* and can be compared to the outcome of the new method.

For that reason, inter-observer studies were performed based on the diagnoses of three different experts, namely

- Dr. Damián Sánchez-Quintana,
  Department of Anatomy and Cell Biology, University of Extremadura, Badajoz, Spain,
- Dr. Yolanda Macías,
  Department of Anatomy and Cell Biology, University of Extremadura, Badajoz, Spain,
- and Dr. Sergio Alama Carrizo,
  Instituto de Medicina Legal de Badajoz, Badajoz, Spain.

In a first study, the 70 images of set IIa were grouped by two experts according to different types of fibrosis (compact, diffuse, interstitial, patchy). Their decision should be based on the classification scheme published by de Jong et al.[8], which was presented in section 9.2.1. The four groups by de Jong were complemented by an additional group of images showing no fibrosis.
A second study included the 110 images of set IIb. Each of the three experts assigned the images to one of the five groups (no fibrosis, compact, diffuse, interstitial, patchy).

Several methods exist to obtain an actual measure out of the observers' classifications. Considering the fact that the data is nominal and originated from more than two observers, *Krippendorff's alpha (coefficient)* k_α was chosen as the measure for inter-rater agreement[152,153]. Krippendorff's coefficient usually has values between 0 (no agreement between raters) and 1 (perfect agreement), there might be also values < 0 when there are systematic disagreements. k_α can be calculated computationally efficient by utilizing coincidence matrices[154].

One has to mention that there might be also differences in the results when the same observer does the classification twice or more times. However, this *intra-observer-variability* was neglected during this study since the inter-observer variability is usually much higher.

11.2. Polarization Microscopy

Since Picrosirius Red enhances the intrinsic birefringence of mature collagen, polarization microscopy was used to investigate images that clearly showed fibrotic regions. Different samples of image set IIa were analysed using a *Nikon eclipse 80i* polarization microscope (objective: 4×, 0.2, WD20). Five regions showing different types of

fibrosis were chosen and recorded under normal lighting and linear polarization (angle between polarization filters: 45°) lighting conditions. Images were captured with exposure times between 333 ms and 1500 ms, the *NIS-Elements D* software tool was used for digitalization (2560 × 1920 pixels, lossless TIFF).

In total, five image pairs (normal, polarization) showing different types of fibrosis were captured, see Figure 11.1 for an example. The obtained images were used to optimize

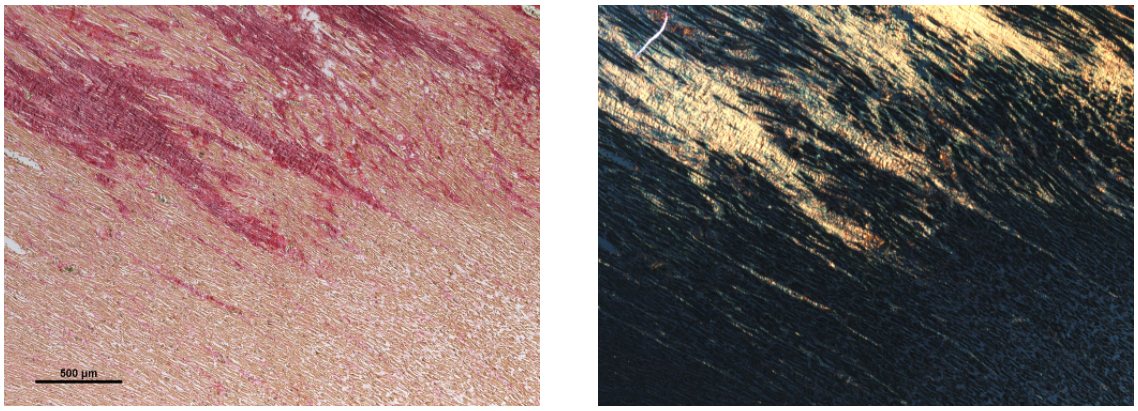

(a) normal **(b)** polarization

Figure 11.1.: Polarization Microscopy - normal (a) and polarization (b) mode. A specific region of one of the samples of set IIa is shown. The black bar in (a) represents a length of 500 µm. The red regions in (a) highlight high collagen content. In polarization mode (b) these regions are very bright and show a better contrast to the surrounding tissue.

parameters necessary for segmentation of fibrotic regions in digital images of samples stained with Picrosirius Red.

11.3. Image Segmentation and Fibrosis Detection

11.3.1. Image Set I

Two different algorithms for segmentation (Colour Thresholding, RGB Relative - see section 2.3.3) were tested and compared. Furthermore, three different parameters (ratios) for assigning images to the control or to the fibrosis group were evaluated.

Segmentation

For quantification of myocardial fibrosis based on Colour Thresholding segmentation[155], as a first step the images were transformed from RGB to the CIE L*a*b* colour space. Thresholds were determined empirically and used to separate the different parts. All pixels with values between the minimum and maximum value of the thresholds were set to 0 (black), all remaining pixels were set to 1 (white). For instance, in the resulting image of the segmentation process for fibrosis, all pixels assigned to the class of fibrosis are white. As a result of this procedure, which is depicted in Figure 11.2, binary images were achieved. The parameters for the RGB Relative algorithm were set empirically by analysing the images of set I and selecting the values, which identified the tissue compartments best.

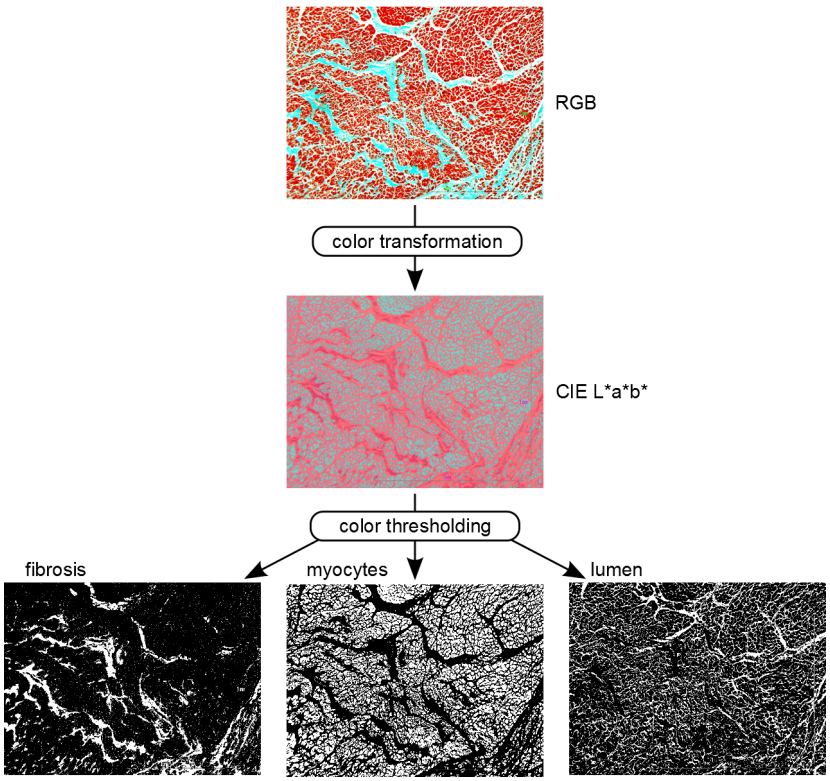

Figure 11.2.: The different steps of the Colour Thresholding algorithm. As a result, binary images were achieved that showed the positions of the pixels assigned to different classes (fibrosis, myocytes, lumen). Figure taken from "M. Mayrhofer-Reinhartshuber et al., *Semi-Automated Detection and Fractal Characterization of Myocardial Fibrosis in Histological Images*; in: Biomedizinische Technik/Biomedical Engineering Vol **59**, p. S616-S619, Figure 1, ©2014 Walter de Gruyter"[151].

Pixel Ratios

The binary images obtained from the segmentation algorithms were used to calculate values proportional to the amount of fibrosis N_{fib}, myocytes N_{myo}, and lumen N_{lum} by summing up the white pixels in the corresponding binary images. Three different ratios r_1, r_2, r_3, were calculated and tested as classification parameters for assigning images to the control or to the fibrosis group.

$$\begin{aligned} r_1 &= N_{\text{fib}}/A_{\text{total}} \\ r_2 &= N_{\text{fib}}/(N_{\text{fib}} + N_{\text{myo}}) \\ r_3 &= N_{\text{fib}}/(A_{\text{total}} - N_{\text{lum}}) \end{aligned}$$

The total area A_{total} is given by the total number of pixels of an image.

11.3.2. Image Set II

Based on the RGB Relative algorithm, two different parameters (ratios) were calculated for assigning images to one of the different types of fibrosis.

Segmentation

For quantification of the collagen, i.e. fibrosis in image sets IIa and IIb, the RGB Relative algorithm was used. Necessary parameters were set empirically by analysing both sub-sets IIa and IIb individually and selecting the values, which identified the tissue compartments best.

Pixel Ratios

The obtained binary images were used to calculate values proportional to the amount of fibrosis N_{fib}, myocytes N_{myo}, and lumen N_{lum}. From an electrophysiological point of view the most interesting ratios r_3 and r_4, given by

$$\begin{aligned} r_3 &= N_{\text{fib}}/(A_{\text{total}} - N_{\text{lum}}) \\ r_4 &= N_{\text{fib}}/(N_{\text{myo}}) \end{aligned}$$

with A_{total} the total number of pixels of an image were calculated.

11.4. Application of Fractal Methods

For images of set I, the binary PM (see section 4.2.2) was used to estimate the fractal dimensions of the segmented images showing fibrosis (connective tissue). D-values obtained from these images were used for assigning them to control or fibrosis group.

All three new pyramidal fractal dimension estimation algorithms (PTPM, PGM, PDM) as well as the best-performing standard approaches (Improved DBCM, HM) were applied to the images of set II (downscaled to a size of 4096×4096 pixels, bicubic interpolation). Optimized scale-ranges (see section 7.2.1 and appendix A.2) were used for all methods, for the pyramidal methods bilinear interpolation was used. For images of set IIa, fractal dimension estimation algorithms were applied to the red-channel of the

segmented images. For images of set IIb, fractal dimension estimation algorithms were applied to the blue-channel of the whole images under investigation.

11.5. Classification of Fibrosis

As a ground truth for the classification of the different types of fibrosis, the results from the inter-rater reliability study were used. For image set IIa, all images that had been classified in the same group by both raters (two-observer-agreement) were taken. For the evaluation of image set IIb, all images having a three-observer agreement were used. Calculated tissue ratios (r_3, r_4) and D-values were assigned to the resulting ground truth groups, mean values and standard errors of the means were calculated. With this approach, typical values (ratios, D-values) for each type of fibrosis were obtained.

To test for normal distribution of the values within each group, Shapiro-Wilk (S-W) tests ($\alpha = 0.05$) were used . One-way analysis of variance (ANOVA) was applied to test for significant differences of the means. Significant differences between the individual groups were evaluated by post-hoc pairwise t-tests (Fisher's least significant difference).

11.5.1. Automated Classification of Fibrosis and Optimization

For an automated classification, rules for assigning an investigated image to a specific type of fibrosis have to be defined. The most simple approach is to define individual constant thresholds for D-values and collagen ratios of each group, i.e. if the resulting D-value and tissue ratios for an image are within predefined, constant ranges, the image is assigned to the corresponding fibrosis type. A slightly more advanced technique is to use simple functions as thresholds, e.g. in a way that thresholds for D-values are dependent on the values of the collagen ratios. Both approaches were used in this work, the latter with a linear dependency between D-value thresholds and collagen ratio. Optimum thresholds were found by varying the value ranges for each type of fibrosis and using the number of the correctly classified ground truth images as a measure. The thresholds that resulted in the maximum number of correctly assigned ground truth images were taken as the optimum values for an automated classification. Additionally, also the thresholds for the segmentation of the different types of tissue (fibrosis,

myocytes, lumen) were varied within a pre-defined range to achieve optimum results. Thereafter the whole image sets IIa and IIb were investigated with these optimized parameters and compared to the classification of the experts.

12. Results and Discussion

12.1. Image Set I

Segmentation algorithms were used to differentiate between the three different regions (fibrosis, myocytes and lumen) in the 40 images of set I. Furthermore, fractal analysis was used to characterize the images. The main aim of the work with this image set was to differentiate between control- and fibrosis-group images.

12.1.1. Pixel Ratios

The empirically determined threshold values for the Colour Thresholding algorithm that were used to separate fibrosis, myocytes and lumen in the investigated images are given in Table 12.1. For the RGB Relative algorithm, the ratio $B > R + (1 - t_{\text{fib}})$ with a sensitivity threshold $t_{\text{fib}} = 0.8$ for the segmentation of fibrotic regions was used. For the regions showing myocytes, $R > B + (1 - t_{\text{myo}})$ with $t_{\text{myo}} = 0.8$, for the lumen the ratio $(R + G + B)/3 > t_{\text{lum}}$ with $t_{\text{lum}} = 0.9$ were used.

Table 12.1.: Empirically determined thresholds for the Colour Thresholding algorithm applied to image set I. L*, a* and b* refer to the minimum (min) and maximum (max) thresholds for the channels in the CIE L*a*b* colour space.

	L*(min)	L*(max)	a*(min)	a*(max)	b*(min)	b*(max)	invert
fibrosis	201	255	0	255	0	255	no
myocytes	0	255	124	255	133	255	yes
lumen	0	208	138	255	0	255	no

The most significant parameter for assigning images to the control or to the fibrosis group was identified by calculating three different ratios, which may be used as classification parameters. All obtained ratios were tested on normal distribution by using

the Shapiro-Wilk (S-W) test with a level of significance $\alpha = 0.05$. Thereafter, mean values for r_1, r_2, r_3 and standard errors of the means were calculated. The obtained results can be seen in Figure 12.1a. All ratios show clear differences between control and fibrosis groups. Figure 12.1b compares the results of the two segmentation methods (Colour Thresholding, RGB Relative) for the best discriminative ratio r_2. Both methods yielded a statistically significant differentiation between control and fibrosis group (Mann-Whitney U test, two-tailed, $p < 0.001$). The difference was higher for Colour Thresholding (control: $r_2 = 4 - 6\%$, fibrosis: $r_2 = 41 - 47\%$) than for RGB Relative (control: $r_2 = 6 - 8\%$, fibrosis: $r_2 = 38 - 44\%$).

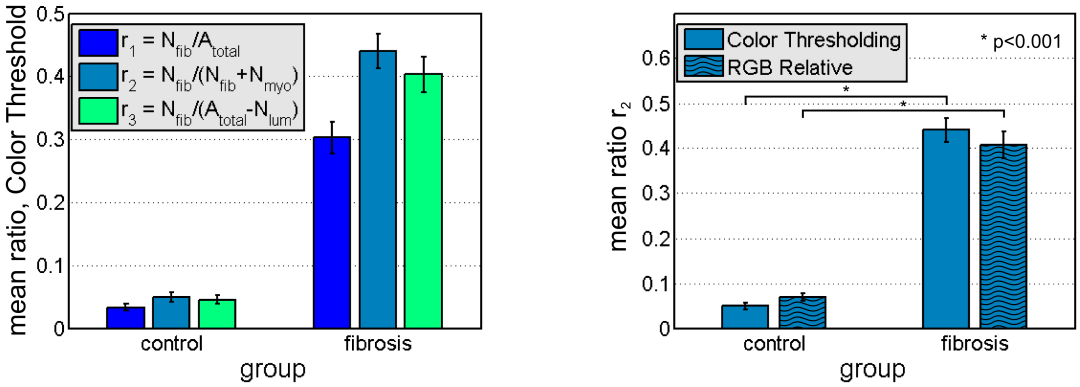

(a) Colour thresholding. **(b)** Discriminatory power of r_2

Figure 12.1.: (a) shows different mean ratios (r_1, r_2, r_3) of the pixel sums assigned to fibrosis N_{fib}, myocytes N_{myo}, lumen N_{lum} and total image pixels A_{total}. r_2 shows the highest difference for differentiating between the investigated groups (control and fibrosis). (b) shows the discriminatory power of r_2 on different segmentation algorithms (Colour Thresholding vs. RGB Relative). Figures taken from "M. Mayrhofer-Reinhartshuber et al., *Semi-Automated Detection and Fractal Characterization of Myocardial Fibrosis in Histological Images*; in: Biomedizinische Technik/Biomedical Engineering Vol **59**, p. S616-S619, Figure 2 and Figure 3, ©2014 Walter de Gruyter"[151].

12.1.2. Fractal Dimension

For the obtained D-values, S-W tests were performed to prove the normal distribution of the obtained values (level of significance $\alpha = 0.05$). The mean value for the estimated fractal dimensions (binary PM) of the control group was found to be $D_{\text{p}} = (0.95 \pm 0.20)$. For the fibrosis group $D_{\text{p}} = (1.65 \pm 0.10)$ was obtained. Student's t-test (two-tailed, p<0.001) was used to show that D_{p} is a statistically significant parameter to discriminate between images of both groups. The results are depicted in Figure 12.2.

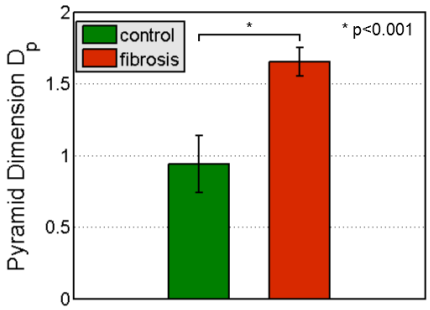

Figure 12.2.: Estimated fractal dimensions (Pyramid Method) of the investigated groups (control vs. fibrosis). Figure taken from "M. Mayrhofer-Reinhartshuber et al., *Semi-Automated Detection and Fractal Characterization of Myocardial Fibrosis in Histological Images*; in: Biomedizinische Technik/Biomedical Engineering Vol **59**, p. S616-S619, Figure 4, ©2014 Walter de Gruyter" [151].

12.2. Image Set IIa

12.2.1. Inter-rater Reliability

Inter-rater reliability for the classification of 70 images from set IIa grouped by two experts yielded a value for Krippendorff's coefficient k_α of

$$k_{\alpha,\mathrm{IIa}} = 0.87.$$

In total 63, i.e. 90% out of the 70 images were classified concordantly and were used as the ground truth in the following steps. The correlation between the diagnoses of the experts is shown in Table A.20 in the appendix A.3.1. Most disagreements occurred between the types *no fibrosis* and *interstitial* (2 of 7 disagreements), and between *interstitial* and *diffuse* (2/7). From the concordantly assigned images, 9 were assigned to *no fibrosis*, 15 to *interstitial*, 13 to *compact*, 11 to *diffuse*, and 15 to *patchy*.

12.2.2. Polarization Microscopy

Five image pairs obtained by normal and polarization microscopy (see section 11.2) of samples of set IIa were used to optimize segmentation with the RGB Relative algorithm (see section 2.3.3). From each of the five polarization images a mask M_{pol} was created as a reference image by using the L*-channel in CIE L*a*b* colour space (Figure 12.3, right). The RGB Relative algorithm was used to create a segmentation mask M_{RGB} based on the corresponding normal image (Figure 12.3, left). The used threshold

t_R for the ratio $R/(R+G+B)$ was varied to find the best agreement between the mask created with RBG Relative and the mask obtained from the polarization image. Therefore, a minimum deviation between both images had to be found by minimizing the squared error $SE = \sum(M_{RGB} - M_{pol})^2$. In Figure 12.3 an example of SE vs. t_R is shown. The analysis of all five image pairs yielded an average, i.e. optimum threshold of $\bar{t}_{R,opt} = (0.47 \pm 0.05)$. However, it has to be noted that the illumination as well as the quality of the histological samples and the used colours had a strong influence on segmentation parameters. Therefore, the applicability of the obtained results for $\bar{t}_{R,opt}$ is limited.

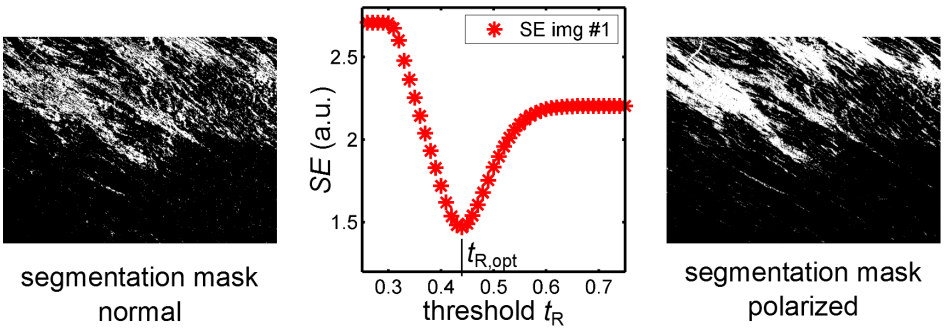

Figure 12.3.: Polarization Microscopy - Evaluation of segmentation parameters. A segmentation mask based on the normal image is created with varying thresholds t_R to find the minimum of SE (minimum difference of the segmented areas of the normal (left) and polarization (right) image) at $t_R = t_{R,opt}$. $t_{R,opt}$ represents the optimum threshold for the RGB Relative algorithm.

12.2.3. Classification of Fibrosis

12.2.3.1. Classification of Fibrosis with Pixel Ratios

For image set IIa the best segmentation of the pixels showing fibrosis was obtained by the RGB Relative algorithm with $R/(R+G+B) > t_{fib}$ and a threshold t_{fib}, where R, G and B denote the normalized red, green and blue values of a pixel. The pixels showing lumen were obtained by $(R+G+B)/3 > t_{lum}$ and a threshold t_{lum}. No distinct segmentation of the regions showing myocytes was possible with basic segmentation algorithms like RGB Relative. Hence r_4 was not calculated for images of image set IIa. Threshold values for reasonable segmentation of the different tissue compartments were empirically determined to be $t_{fib} = 0.64$ and $t_{lum} = 0.9$.

In Figure 12.4 the results for the collagen ratio r_3 of the ground truth images of image set IIa are shown. The blue bars indicate the mean values with the standard errors of the means. S-W tests ($\alpha = 0.05$) verified the normal distribution of the values within each group. One-way ANOVA yielded significant differences for the means ($p < 10^{-8}$). Post-hoc pairwise t-tests (Fisher's LSD) showed significant differences ($p < 0.01$) between the individual groups that are indicated with plus signs.

r_3 yielded significant differences between *compact*, *no fibrosis/interstitial*, and *diffuse/patchy*.

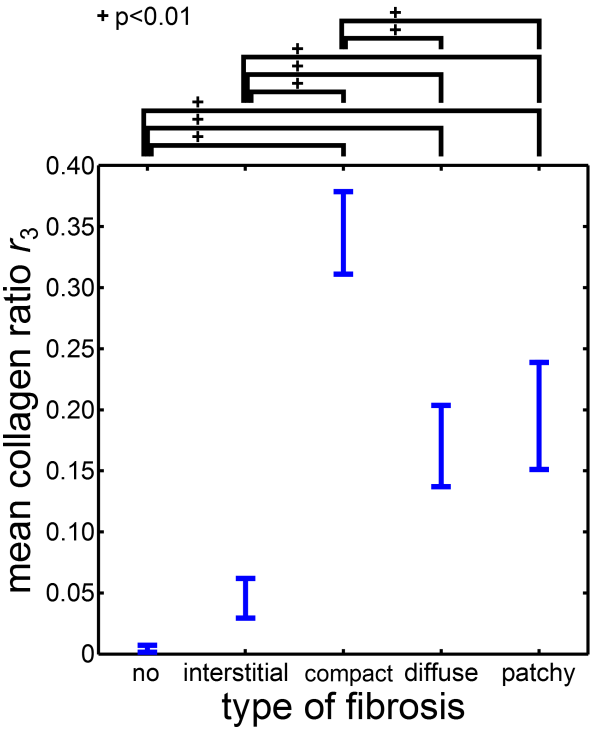

Figure 12.4.: Mean collagen ratio r_3 corresponding to the amounts of fibrosis in the ground truth images of set IIa. For segmentation the parameters $t_{\text{fib}} = 0.64$ and $t_{\text{lum}} = 0.9$ were used. Significant differences ($p < 0.01$) between the groups are indicated with a plus sign.

12.2.3.2. Classification of Fibrosis with Fractal Methods

In Figures 12.5 - 12.9 the results of the three new pyramidal fractal dimension estimation algorithms (PTPM, PGM, PDM) as well as the in part I best-performing standard approaches (Improved DBCM, HM) applied to the ground truth images of image set IIa are shown. The blue bars indicate the mean values with the standard errors of the means. S-W tests ($\alpha = 0.05$) verified the normal distribution of the values within each group. One-way ANOVA yielded significant differences for the means of all tested fractal methods. p-values were very low ($p < 10^{-11}$) for all D-values except for D_{H} ($p < 10^{-3}$). Post-hoc pairwise t-tests (Fisher's LSD) showed significant differences ($p < 0.01$) between the individual groups that are indicated with plus signs in the figures.

$D_{\mathrm{PTP}}^{\mathrm{bilinear}}$ and $D_{\mathrm{PG}}^{\mathrm{simple,bilinear}}$ yielded significant differences between *no fibrosis*, *interstitial*, *compact*, and *diffuse/patchy* - see Figures 12.5 and 12.7. $D_{\mathrm{PD}}^{\mathrm{bilinear}}$ yielded significant differences between *compact*, *patchy* and the other types (*no fibrosis/interstitial/diffuse*) - see Figure 12.6. $D_{\mathrm{DBC}}^{\mathrm{improved}}$ yielded significant differences between *no fibrosis*, *interstitial* and the other types (*compact/diffuse/patchy*) - see Figure 12.8. D_{H} yielded significant differences between *no fibrosis* and *compact/diffuse/patchy* as well as between *interstitial* and *diffuse* - see Figure 12.9.

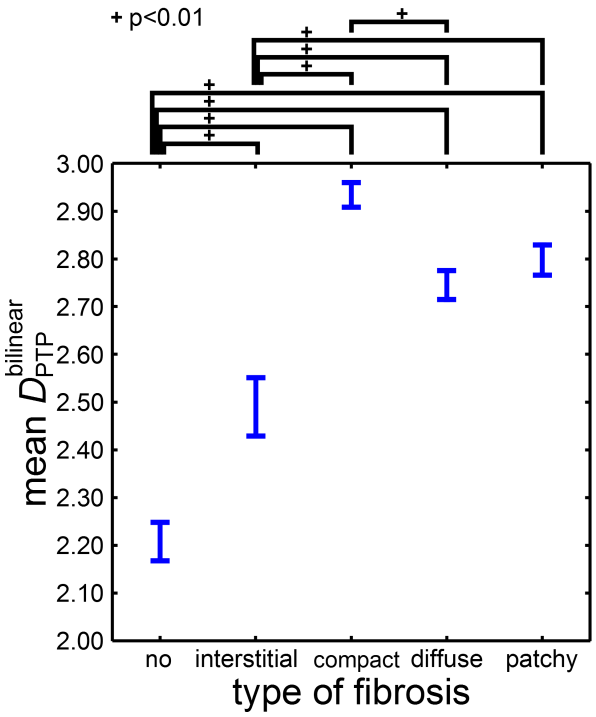

Figure 12.5.: $D_{\mathrm{PTP}}^{\mathrm{bilinear}}$ obtained for the ground truth images of set IIa. Significant differences ($p < 0.01$) between the groups are indicated with a plus sign.

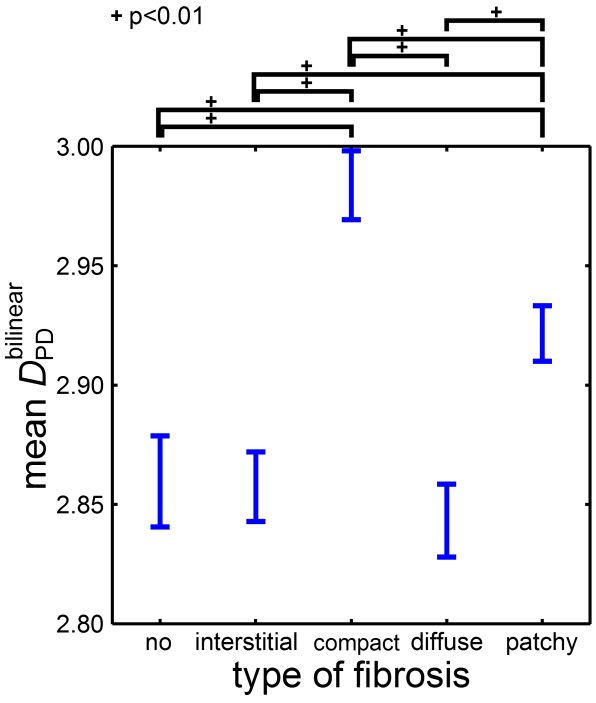

Figure 12.6.: $D_{\mathrm{PD}}^{\mathrm{bilinear}}$ obtained for the ground truth images of set IIa. Significant differences ($p < 0.01$) between the groups are indicated with a plus sign.

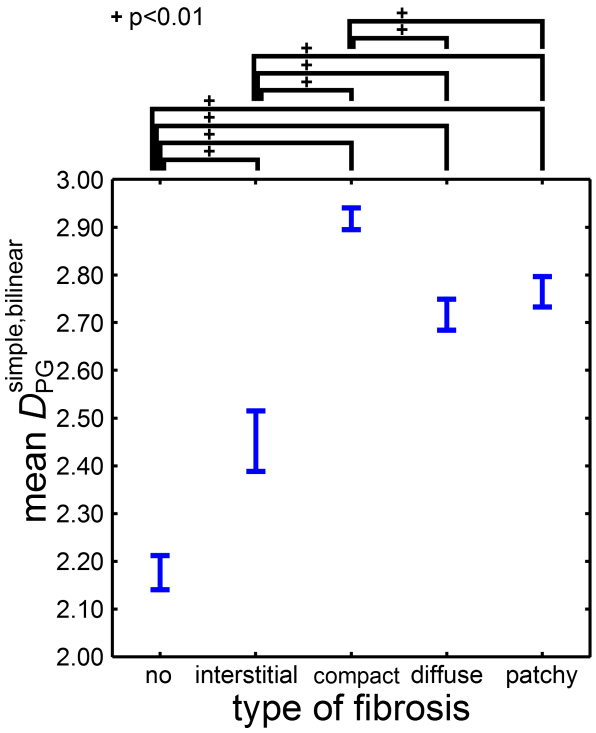

Figure 12.7.: $D_{\mathrm{PG}}^{\mathrm{simple,bilinear}}$ obtained for the ground truth images of set IIa. Significant differences ($p < 0.01$) between the groups are indicated with a plus sign.

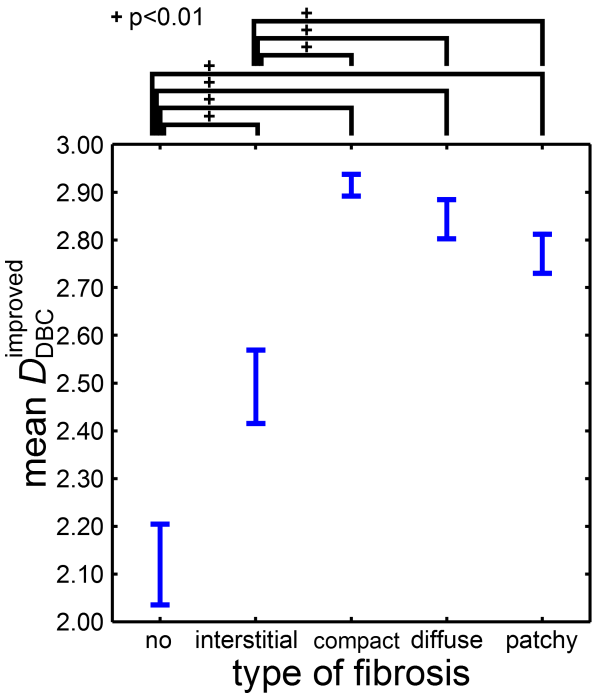

Figure 12.8.: $D_{\mathrm{DBC}}^{\mathrm{improved}}$ obtained for the ground truth images of set IIa. Significant differences ($p < 0.01$) between the groups are indicated with a plus sign.

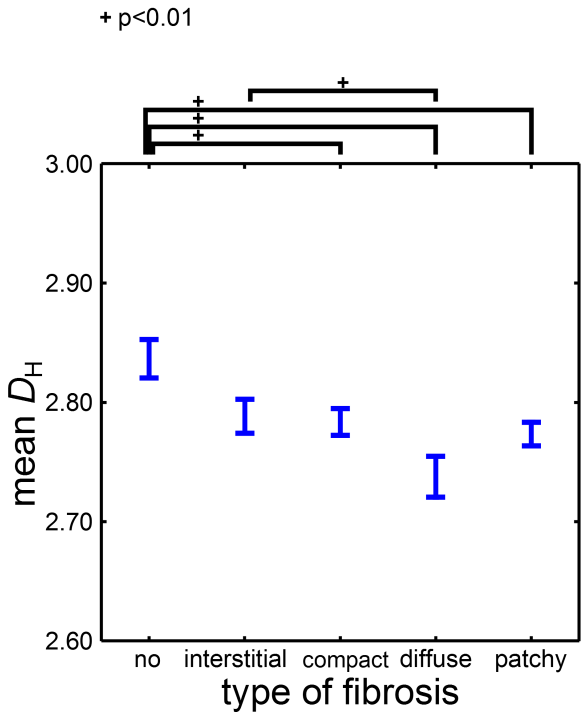

Figure 12.9.: D_H obtained for the ground truth images of set IIa. Significant differences ($p < 0.01$) between the groups are indicated with a plus sign.

12.2.3.3. Automated Classification of Fibrosis

For achieving the goal of an automated classification of the different types of fibrosis the ranges for D- and r_3-values, which acted as classification rules, were optimized as described in chapter 11.5.1. For each type of fibrosis these ranges were varied in predefined regions that were based on the results presented in the previous sections. Furthermore, the segmentation thresholds t_{fib} and t_{lum} were varied within empirically determined ranges, t_{fib} from 0.58 to 0.66, and t_{lum} from 0.82 to 0.98. The ranges which resulted in a maximum number of correctly classified ground truth images $N_{\text{corr,gt}}$ were taken as optimum values. In Tables 12.2 and 12.3 the optimum constant thresholds and ranges of the fractal dimension D and collagen ratio r_3 for an automated classification of the ground truth images to the different types of fibrosis (no fibrosis, interstitial, compact, diffuse, patchy) based on the applied fractal methods (PTPM, PDM, PGM (simple kernel), improved DBCM, HM) are presented. In addition to $N_{\text{corr,gt}}$ also the percentage of correctly classified ground truth images $n_{\text{corr,gt}}$ is given. The optimum ranges given in this and the following tables (12.2, 12.3, 12.5, 12.6) are the classification rules when a new image should be assigned to one of the types of fibrosis. They have to be applied in the same order as they are listed in the tables. So first it has to be checked whether the investigated image belongs to class *no fibrosis*. If not, the next step is to check whether it belongs to class *interstitial* fibrosis, and so on.

Best results were obtained for the PDM and the improved DBCM with which 72% and 70% of all ground truth images were assigned to the correct type of fibrosis.

The optimum parameters were used for an automated classification of all images of image set IIa. In Table 12.4 the obtained results are compared to classifications of each expert $i = 1, 2$. In addition to absolute ($N_{\text{corr},i}$) and relative ($n_{\text{corr},i}$) numbers of concordantly assigned images, Krippendorff's coefficients $k_{\alpha,i}$ are given as measures of agreement between automated and experts classifications.

Best results were obtained for the PDM (66% to 69% of all images assigned concordantly with the experts, $k_{\alpha,\text{i}}$: 0.57 to 0.60) and the improved DBCM (64% to 69%, $k_{\alpha,\text{i}}$: 0.55 to 0.61).

Table 12.2.: Image set IIa - Optimized segmentation thresholds (t_{fib}, t_{lum}) and ranges of fractal dimension D and collagen ratio r_3 for an automated classification of the ground truth images to the different types of fibrosis (no fibrosis, interstitial, compact, diffuse, patchy) based on the applied fractal methods (PTPM, PDM, PGM (simple kernel)). All thresholds and ranges were assumed to be constant (see chapter 11.5.1). $N_{\text{corr,gt}}$ denotes the absolute number, $n_{\text{corr,gt}}$ the percentage of correctly classified images of the 63 ground truth images of image set IIa.

	PTPM	PDM	PGM
t_{fib} t_{lum}	0.66 0.90	0.60 0.90	0.64 0.90
no fibrosis	$D < 2.18$ $r_3 < 0.02$	$r_3 < 0.009$	$D < 2.20$ $r_3 < 0.09$
interstitial	$D \geq 2.18$ $r_3 < 0.02$	$r_3 = [0.009, 0.05]$	$D \geq 2.20$ $r_3 < 0.09$
compact	$D \geq 2.82$ $r_3 \geq 0.02$	$D \geq 2.93$ $r_3 \geq 0.05$	$D \geq 2.85$ $r_3 \geq 0.09$
diffuse	$D < 2.65$ $r_3 \geq 0.02$	$D < 2.87$ $r_3 \geq 0.05$	$D < 2.81$ $r_3 \geq 0.09$
patchy	$D = [2.65, 2.82]$ $r_3 \geq 0.02$	$D = [2.87, 2.93]$ $r_3 \geq 0.05$	$D = [2.81, 2.85]$ $r_3 \geq 0.09$
$N_{\text{corr,gt}}$ $n_{\text{corr,gt}}$	40 64%	45 72%	40 64%

Table 12.3.: Image set IIa - Optimized segmentation thresholds (t_{fib}, t_{lum}) and ranges of fractal dimension D and collagen ratio r_3 for an automated classification of the ground truth images to the different types of fibrosis (no fibrosis, interstitial, compact, diffuse, patchy) based on the applied fractal methods (improved DBCM, HM). All thresholds and ranges were assumed to be constant (see chapter 11.5.1). $N_{\text{corr,gt}}$ denotes the absolute number, $n_{\text{corr,gt}}$ the percentage of correctly classified images of the 63 ground truth images of image set IIa.

	DBCM	HM
t_{fib}	0.62	0.62
t_{lum}	0.98	0.82
no fibrosis	$r_3 < 0.005$	$r_3 < 0.006$
interstitial	$r_3 = [0.005, 0.03]$	$r_3 = [0.006, 0.09]$
compact	$r_3 > 0.31$	$r_3 > 0.33$
diffuse	$D > 2.88$ $r_3 = [0.03, 0.31]$	$D < 2.72$ $r_3 = [0.09, 0.33]$
patchy	$D \leq 2.88$ $r_3 = [0.03, 0.31]$	$D \geq 2.72$ $r_3 = [0.09, 0.33]$
$N_{\text{corr,gt}}$	44	40
$n_{\text{corr,gt}}$	70%	64%

Table 12.4.: Image set IIa - Concordantly classified images in absolute ($N_{\text{corr},i}$) and relative ($n_{\text{corr},i}$) numbers obtained with methods and ranges given in Tables 12.2 and 12.3. In addition Krippendorff's coefficients $k_{\alpha,i}$ are given as measures of agreement between automated and experts ($i = 1, 2$) classifications. The agreement between both experts was found to be $k_{\alpha,\text{IIa}} = 0.87$ (63 out of 70 images, i.e. 90% assigned to the same groups, see section 12.2.1).

	PTPM	PDM	PGM	DBCM	HM
$N_{\text{corr},1}$	41	46	42	45	43
$N_{\text{corr},2}$	44	48	43	48	43
$n_{\text{corr},1}$	59%	66%	60%	64%	61%
$n_{\text{corr},2}$	63%	69%	61%	69%	61%
$k_{\alpha,1}$	0.47	0.57	0.49	0.55	0.51
$k_{\alpha,2}$	0.53	0.60	0.51	0.61	0.51

In Tables 12.5 and 12.6 the optimum thresholds and ranges of the fractal dimension D and collagen ratio r_3 with thresholds for D assumed as linear functions of r_3 (see chapter 11.5.1) for an automated classification of the ground truth images to the different types of fibrosis (no fibrosis, interstitial, compact, diffuse, patchy) based on the applied fractal methods (PTPM, PDM, PGM (simple kernel), improved DBCM, HM) are presented. In addition to $N_{\mathrm{corr,gt}}$ also the percentage of correctly classified ground truth images $n_{\mathrm{corr,gt}}$ is given.

Best results were obtained for the PDM with which 76% of all ground truth images were assigned to the correct type of fibrosis.

The optimum parameters were used for an automated classification of all images of image set IIa. In Table 12.7 the obtained results are compared to classifications of each expert $i = 1, 2$. In addition to absolute ($N_{\mathrm{corr},i}$) and relative ($n_{\mathrm{corr},i}$) numbers of concordantly assigned images, Krippendorff's coefficients $k_{\alpha,i}$ are given as measures of agreement between automated and experts classifications.

Best results were obtained for the PDM with which 71% to 73% of all images were assigned concordantly with the experts ($k_{\alpha,\mathrm{i}}$: 0.64 to 0.66). The correlation between the diagnoses of the human experts and the automated diagnosis with PDM is shown in Tables A.21 and A.22 in the appendix A.3.1.

Table 12.5.: Image set IIa - Optimized segmentation thresholds (t_{fib}, t_{lum}) and ranges of fractal dimension D and collagen ratio r_3 for an automated classification of the ground truth images to the different types of fibrosis (no fibrosis, interstitial, compact, diffuse, patchy) based on the applied fractal methods (PTPM, PDM). Thresholds for D were assumed as linear functions of r_3 (see chapter 11.5.1). $N_{\text{corr,gt}}$ denotes the absolute number, $n_{\text{corr,gt}}$ the percentage of correctly classified images of the 63 ground truth images of image set IIa.

	PTPM	PDM
t_{fib} t_{lum}	0.66 0.90	0.60 0.90
no fibrosis	$D < 2.175$ $r_3 < 0.004$	$D \leq 2.8$ $r_3 < 0.05$ or $r_3 < 0.009$
interstitial	$r_3 < 0.0193$	$D > 2.8$ $r_3 = [0.009, 0.05]$
compact	$D \geq (-1.121 \cdot r_3 + 3.137)$ $r_3 \geq 0.0193$	$D \geq (-0.2 \cdot r_3 + 3.01)$ $r_3 \geq 0.05$
diffuse	$D < (-1.121 \cdot r_3 + 3.137)$ $r_3 > 0.163$	$D < (-0.2 \cdot r_3 + 3.01)$ $D < 2.869$
patchy	$D < (-1.121 \cdot r_3 + 3.137)$ $r_3 = [0.0193, 0.163]$	$D < (-0.2 \cdot r_3 + 3.01)$ $D \geq 2.869$
$N_{\text{corr,gt}}$ $n_{\text{corr,gt}}$	43 68%	48 76%

Table 12.6.: Image set IIa - Optimized segmentation thresholds (t_{fib}, t_{lum}) and ranges of fractal dimension D and collagen ratio r_3 for an automated classification of the ground truth images to the different types of fibrosis (no fibrosis, interstitial, compact, diffuse, patchy) based on the applied fractal methods (PGM (simple kernel), improved DBCM, HM). Thresholds for D were assumed as linear functions of r_3 (see chapter 11.5.1). $N_{\text{corr,gt}}$ denotes the absolute number, $n_{\text{corr,gt}}$ the percentage of correctly classified images of the 63 ground truth images of image set IIa.

	PGM	DBCM	HM
t_{fib} t_{lum}	0.64 0.90	0.62 0.98	0.62 0.82
no fibrosis	$D < 2.194$ $r_3 < 0.005$	$r_3 < 0.005$	$r_3 < 0.006$
interstitial	$r_3 < 0.024$	$r_3 = [0.005, 0.03]$	$r_3 < 0.09$
compact	$D \geq (-1.312 \cdot r_3 + 3.238)$ $r_3 \geq 0.024$	$D \leq (0.7 \cdot r_3 + 2.7)$ $r_3 > 0.11$	$D \geq (-0.4 \cdot r_3 + 2.87)$ $r_3 \geq 0.09$
diffuse	$D < (-1.312 \cdot r_3 + 3.238)$ $r_3 > 0.19$	$D > (0.7 \cdot r_3 + 2.7)$ $D > 2.88$	$D < (-0.4 \cdot r_3 + 2.87)$ $D < 2.705$
patchy	$D < (-1.312 \cdot r_3 + 3.238)$ $r_3 = [0.024, 0.19]$	$D > (0.7 \cdot r_3 + 2.7)$ $D \leq 2.88$	$D < (-0.4 \cdot r_3 + 2.87)$ $D \geq 2.705$
$N_{\text{corr,gt}}$ $n_{\text{corr,gt}}$	43 68%	45 71%	43 68%

Table 12.7.: Image set IIa - Concordantly classified images in absolute ($N_{\text{corr},i}$) and relative ($n_{\text{corr},i}$) numbers obtained with methods and ranges given in Tables 12.5 and 12.6. In addition Krippendorff's coefficients $k_{\alpha,i}$ are given as measures of agreement between automated and experts ($i = 1, 2$) classifications. The agreement between both experts was found to be $k_{\alpha,\text{IIa}} = 0.87$ (63 out of 70 images, i.e. 90% assigned to the same groups, see section 12.2.1).

	PTPM	PDM	PGM	DBCM	HM
$N_{\text{corr},1}$	45	50	45	46	46
$N_{\text{corr},2}$	46	51	46	49	46
$n_{\text{corr},1}$	64%	71%	64%	66%	66%
$n_{\text{corr},2}$	66%	73%	66%	70%	66%
$k_{\alpha,1}$	0.55	0.64	0.55	0.57	0.57
$k_{\alpha,2}$	0.57	0.66	0.57	0.62	0.57

12.3. Image Set IIb

12.3.1. Inter-rater Reliability

Inter-rater reliability for the classification of 110 images of set IIb classified by all three experts yielded an agreement (Krippendorff's coefficient k_α) of

$$k_{\alpha,\mathrm{IIb},3} = 0.70.$$

In total 73, i.e. 66% out of the 110 images were classified concordantly and were used as the ground truth in the following steps. The correlation between the diagnoses of the experts is shown in Tables A.23, A.24 and A.25 in the appendix A.3.2. Most disagreements occurred between the types *diffuse* and *interstitial* (10 of 37 disagreements), *no fibrosis* and *interstitial* (8/37), and between *compact* and *patchy* (8/37). From the concordantly assigned images, 8 were assigned to *no fibrosis*, 15 to *interstitial*, 24 to *compact*, 10 to *diffuse*, and 16 to *patchy*.

When neglecting the classification of the least experienced observer, i.e. including only the rating by the two same experts as for set IIa, a value of

$$k_{\alpha,\mathrm{IIb},2} = 0.76$$

was found. 89, i.e. 81% out of the 110 images were classified concordantly. Most disagreements occurred between the types *diffuse* and *interstitial* (7 of 21 disagreements), *compact* and *patchy* (4/21), and between *no fibrosis* and *interstitial* (3/21).

12.3.2. Classification of Fibrosis

12.3.2.1. Classification of Fibrosis with Pixel Ratios

For image set IIb the segmentation of the pixels showing fibrosis was obtained by the RGB Relative algorithm with $B > R + (1 - t_{\mathrm{fib}})$, t_{fib} denoting a sensitivity threshold. The pixels showing lumen were obtained by $(R+G+B)/3 > t_{\mathrm{lum}}$ with a threshold t_{lum}. Segmentation of the pixels showing myocytes was obtained by $R/(R+G+B) > t_{\mathrm{myo}}$ with a threshold t_{myo}. Threshold values for reasonable segmentation of the different tissue compartments were empirically determined to be $t_{\mathrm{fib}} = 0.9$, $t_{\mathrm{lum}} = 0.9$, and $t_{\mathrm{myo}} = 0.38$.

In Figure 12.10 the results for the collagen ratios r_3 and r_4 of the ground truth images of image set IIb are shown. The blue bars indicate the mean values with the standard errors of the means. S-W tests ($\alpha = 0.05$) verified the normal distribution of the values within each group. One-way ANOVA yielded significant differences for the means (r_3: $p < 10^{-16}$, r_4: $p < 10^{-4}$). Post-hoc pairwise t-tests (Fisher's LSD) showed significant differences between the individual groups that are indicated with asterisks ($p < 0.001$) or plus signs ($p < 0.01$).

r_3 yielded significant differences between *compact*, *diffuse/patchy*, and *no fibrosis/interstitial* - see Figure 12.10a. r_4 yielded significant differences between *compact* and all other types *no fibrosis/interstitial/diffuse/patchy* - see Figure 12.10b.

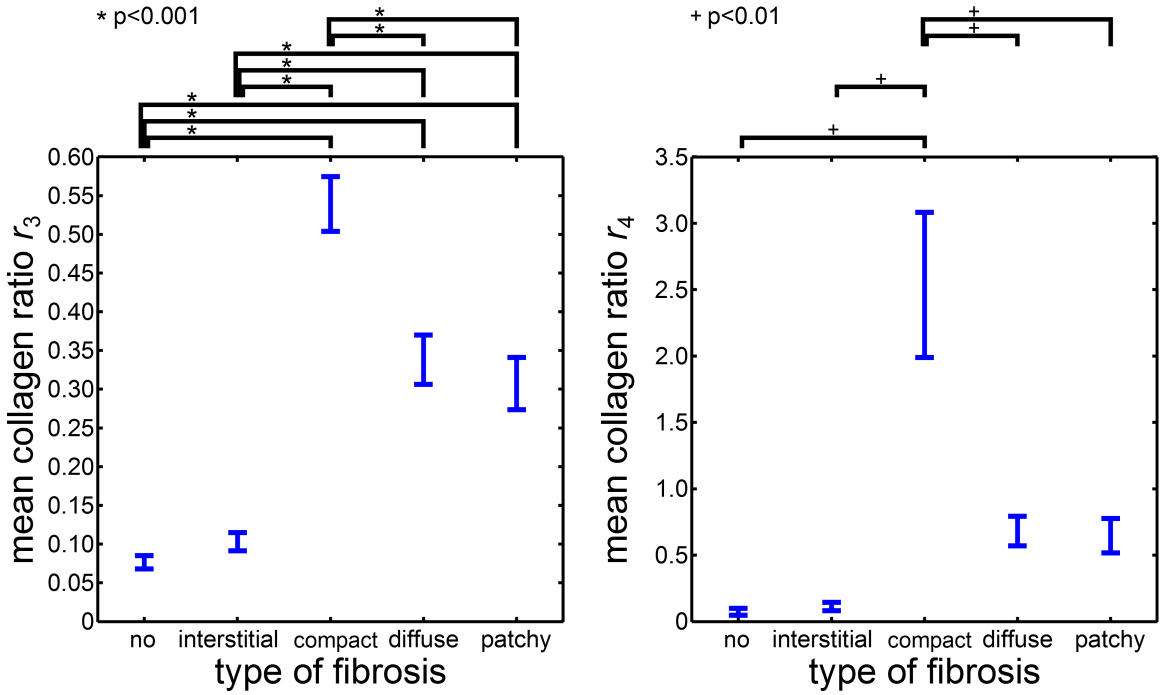

(a) r_3, $t_{\text{fib}} = 0.9$, $t_{\text{lum}} = 0.9$. **(b)** r_4, $t_{\text{fib}} = 0.9$, $t_{\text{myo}} = 0.38$.

Figure 12.10.: Mean collagen ratios r_3 (a) and r_4 (b) corresponding to the amounts of fibrosis in the ground truth images of set IIb. Significant differences between the groups are indicated with asterisks ($p < 0.001$) or plus signs ($p < 0.01$).

12.3.2.2. Classification of Fibrosis with Fractal Methods

In Figures 12.11 - 12.15 the results of the three new pyramidal fractal dimension estimation algorithms (PTPM, PGM, PDM) as well as the in part I best-performing standard approaches (Improved DBCM, HM) applied to the ground-truth images of

image set IIb are shown. The blue bars indicate the mean values with the standard errors of the means. S-W tests ($\alpha = 0.05$) verified the normal distribution of the values within each group. One-way ANOVA yielded significant differences ($p < 10^{-8}$) for the means of all tested methods except $D_{\mathrm{DBC}}^{\mathrm{improved}}$ ($p > 0.39$). Post-hoc pairwise t-tests (Fisher's LSD) showed significant differences ($p < 0.01$) between the individual types of fibrosis that are indicated with plus signs in the figures.

$D_{\mathrm{PTP}}^{\mathrm{bilinear}}$ and $D_{\mathrm{PG}}^{\mathrm{simple,bilinear}}$ showed significant differences between *compact* and all other types, between *interstitial* and *diffuse* and between *diffuse* and *patchy* - see Figures 12.11 and 12.13. $D_{\mathrm{PD}}^{\mathrm{bilinear}}$ and D_{H} showed significant differences between *compact*, *diffuse* and the other types (*no fibrosis*/*interstitial*/*patchy*) - see Figures 12.12 and 12.15. $D_{\mathrm{DBC}}^{\mathrm{improved}}$ showed no significant differences between the types of fibrosis (One-way ANOVA: $p > 0.39$) - see Figure 12.14.

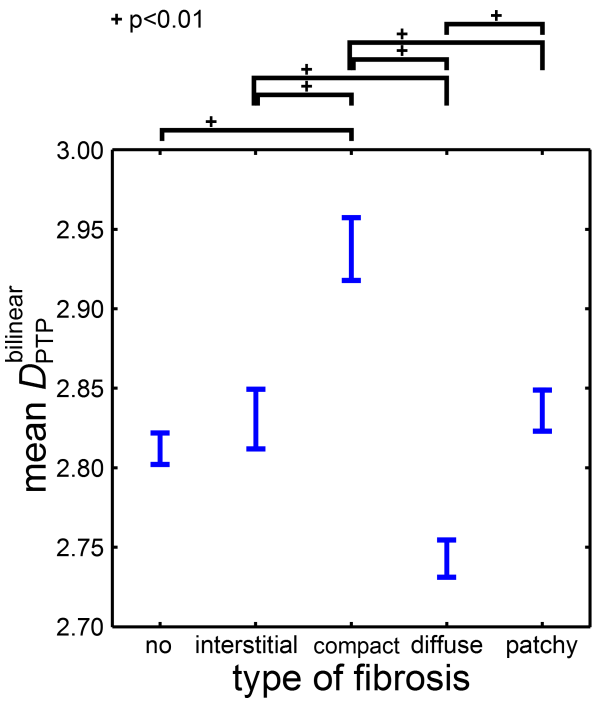

Figure 12.11.: $D_{\mathrm{PTP}}^{\mathrm{bilinear}}$ obtained for the ground truth images of set IIb. Significant differences ($p < 0.01$) between the groups are indicated with a plus sign.

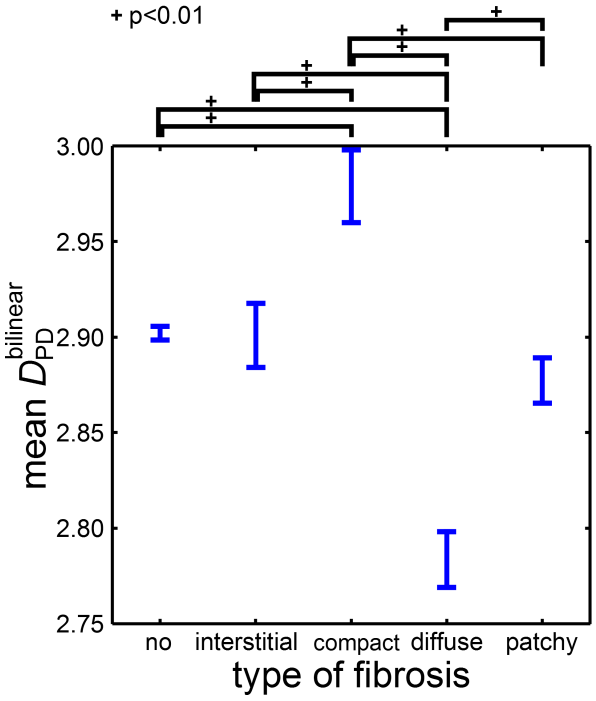

Figure 12.12.: $D_{\mathrm{PD}}^{\mathrm{bilinear}}$ obtained for the ground truth images of set IIb. Significant differences ($p < 0.01$) between the groups are indicated with a plus sign.

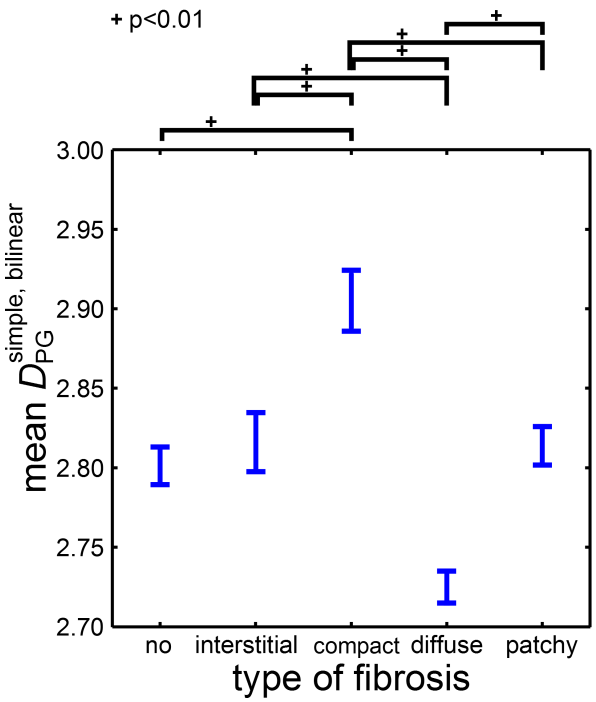

Figure 12.13.: $D_{\mathrm{PG}}^{\mathrm{simple,bilinear}}$ obtained for the ground truth images of set IIb. Significant differences ($p < 0.01$) between the groups are indicated with a plus sign.

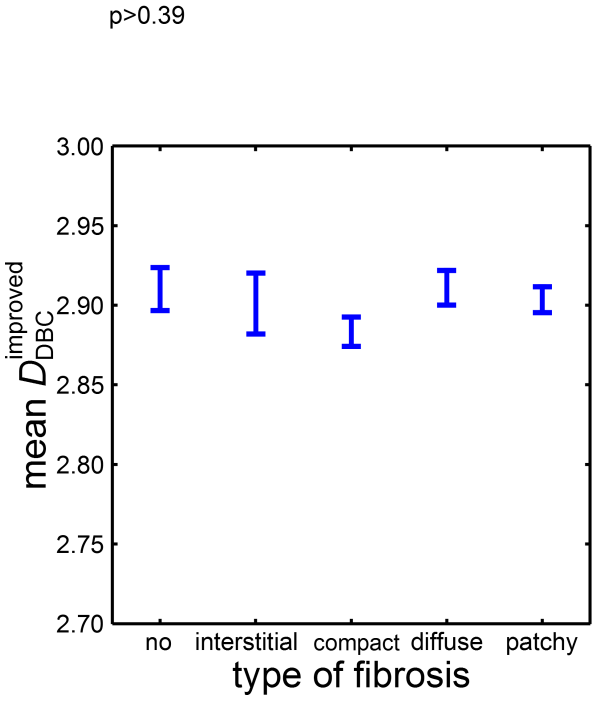

Figure 12.14.: $D_{\mathrm{DBC}}^{\mathrm{improved}}$ obtained for the ground truth images of set IIb. No significant differences between the groups were found (One-way ANOVA: $p > 0.39$).

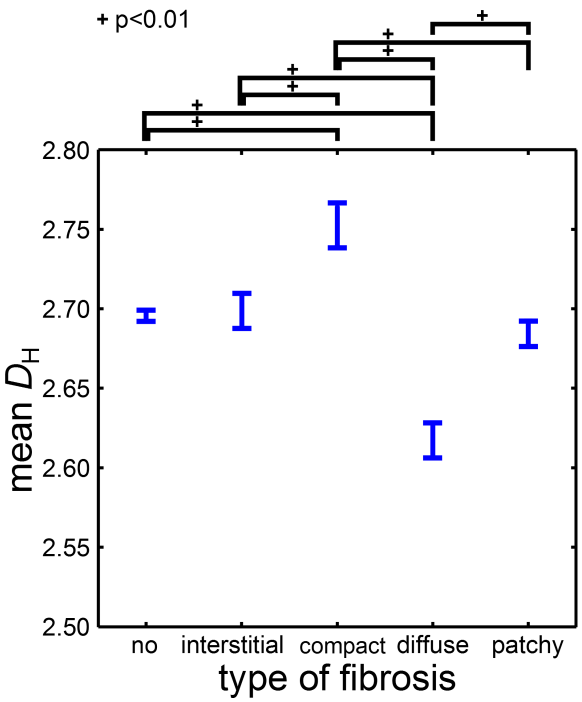

Figure 12.15.: D_H obtained for the ground truth images of set IIb. Significant differences ($p < 0.01$) between the groups are indicated with a plus sign.

12.3.2.3. Automated Classification of Fibrosis

For achieving the goal of an automated classification of the different types of fibrosis the ranges for D-, r_3-, and r_4-values, which acted as classification rules, were optimized as described in chapter 11.5.1. For each type of fibrosis these ranges were varied in predefined regions that were based on the results presented in the previous sections. Furthermore, the segmentation thresholds t_{fib}, t_{lum} and t_{myo} were varied within empirically determined ranges, t_{fib} from 0.58 to 0.66, t_{lum} from 0.82 to 0.98, and t_{myo} from 0.36 to 0.40. The ranges which resulted in a maximum number of correctly classified ground truth images $N_{\text{corr,gt}}$ were taken as optimum values. In Table 12.8 the optimum constant thresholds and ranges of the fractal dimension D and collagen ratio r_3 for an automated classification of the ground truth images to the different types of fibrosis (no fibrosis, interstitial, compact, diffuse, patchy) based on the applied fractal methods (PTPM, PDM, PGM (simple kernel), HM) are presented. Table 12.10 shows the results with collagen ratio r_4. DBCM showed no significant differences of $D_{\text{DBC}}^{\text{improved}}$ between the different types of fibrosis and is therefore not included in these tables. In addition to $N_{\text{corr,gt}}$ also the percentage of correctly classified ground truth images $n_{\text{corr,gt}}$ is given. The optimum ranges given in this and the following tables (12.8, 12.10, 12.12, 12.13,

12.15, 12.16) are the classification rules when a new image should be assigned to one of the types of fibrosis. They have to be applied in the same order as they are given in the tables. So first it has to be checked whether the investigated image belongs to class *no fibrosis*. If not, the next step is to check whether it belongs to class *interstitial* fibrosis, and so on.

The investigated methods yielded comparable results with 73% to 75% (r_3) and 71% to 74% (r_4) correctly assigned ground truth images, the results obtained including collagen ratio r_3 being slightly better than with r_4.

The optimum parameters were used for an automated classification of all images of image set IIb. In Tables 12.9 and 12.11 the obtained results are compared to classifications of each expert $i = 1, 2, 3$. In addition to absolute ($N_{\mathrm{corr},i}$) and relative ($n_{\mathrm{corr},i}$) numbers of concordantly assigned images, Krippendorff's coefficients $k_{\alpha,i}$ (comparison with one expert) and $k_{\alpha,[i,j]}$ (comparison with two experts) are given as measures of agreement between automated and experts classifications.

Comparable results were obtained for all investigated methods, being slightly better with collagen ratio r_3 (61% to 67% of all images assigned concordantly with the experts, $k_{\alpha,[\mathrm{i,j}]}$: 0.53 to 0.63) than with r_4 (56% to 65%, $k_{\alpha,[\mathrm{i,j}]}$: 0.51 to 0.63).

Table 12.8.: Image set IIb - Optimized segmentation thresholds (t_{fib}, t_{lum}) and ranges of fractal dimension D and collagen ratio r_3 for an automated classification of the ground truth images to the different types of fibrosis (no fibrosis, interstitial, compact, diffuse, patchy) based on the applied fractal methods (PTPM, PDM, PGM (simple kernel), HM). All thresholds and ranges were assumed to be constant (see chapter 11.5.1). $N_{\text{corr,gt}}$ denotes the absolute number, $n_{\text{corr,gt}}$ the percentage of correctly classified images of the 73 ground truth images of image set IIb.

	PTPM	PDM	PGM	HM
t_{fib} t_{lum}	0.80 0.98	0.75 0.94	0.80 0.94	0.90 0.90
no fibrosis	$r_3 \leq 0.022$	$r_3 \leq 0.023$	$r_3 \leq 0.021$	$r_3 \leq 0.057$
interstitial	$r_3 = [0.022, 0.08]$	$r_3 = [0.023, 0.06]$	$r_3 = [0.021, 0.08]$	$r_3 = [0.057, 0.15]$
compact	$r_3 \geq 0.27$	$r_3 \geq 0.24$	$r_3 \geq 0.28$	$D \geq 2.73$ $r_3 \geq 0.15$
diffuse	$D < 2.77$ $r_3 = [0.08, 0.27]$	$D < 2.84$ $r_3 = [0.06, 0.24]$	$D < 2.77$ $r_3 = [0.08, 0.28]$	$D < 2.64$ $r_3 \geq 0.15$
patchy	$D \geq 2.77$ $r_3 = [0.08, 0.27]$	$D \geq 2.84$ $r_3 = [0.06, 0.24]$	$D \geq 2.77$ $r_3 = [0.08, 0.28]$	$D = [2.64, 2.73)$ $r_3 \geq 0.15$
$N_{\text{corr,gt}}$ $n_{\text{corr,gt}}$	53 73%	53 73%	55 75%	54 74%

Table 12.9.: Image set IIb (110 images) - Concordantly classified images in absolute ($N_{\mathrm{corr},i}$) and relative ($n_{\mathrm{corr},i}$) numbers obtained with methods and ranges given in Table 12.8. In addition Krippendorff's coefficients $k_{\alpha,[i,j]}$ are given as measures of agreement between automated and experts ($[i,j] = 1,2,3$) classifications (single index i: comparison with one expert i, double index $[i,j]$: comparison with two experts i and j). The agreement between all three experts was found to be $k_{\alpha,\mathrm{IIb},3} = 0.70$ (see section 12.3.1).

	PTPM	PDM	PGM	HM
$N_{\mathrm{corr},1}$	69	70	70	72
$N_{\mathrm{corr},2}$	67	68	67	66
$N_{\mathrm{corr},3}$	70	69	74	73
$n_{\mathrm{corr},1}$	63%	64%	64%	65%
$n_{\mathrm{corr},2}$	61%	62%	61%	60%
$n_{\mathrm{corr},3}$	64%	63%	67%	66%
$k_{\alpha,1}$	0.52	0.54	0.53	0.55
$k_{\alpha,2}$	0.50	0.52	0.50	0.48
$k_{\alpha,3}$	0.53	0.53	0.57	0.56
$k_{\alpha,[1,2]}$	0.59	0.61	0.60	0.60
$k_{\alpha,[1,3]}$	0.61	0.61	0.63	0.63
$k_{\alpha,[2,3]}$	0.53	0.54	0.55	0.54

Table 12.10.: Image set IIb - Optimized segmentation thresholds (t_{fib}, t_{myo}) and ranges of fractal dimension D and collagen ratio r_4 for an automated classification of the ground truth images to the different types of fibrosis (no fibrosis, interstitial, compact, diffuse, patchy) based on the applied fractal methods (PTPM, PDM, PGM (simple kernel), HM). All thresholds and ranges were assumed to be constant (see chapter 11.5.1). $N_{\text{corr,gt}}$ denotes the absolute number, $n_{\text{corr,gt}}$ the percentage of correctly classified images of the 73 ground truth images of image set IIb.

	PTPM	PDM	PGM	HM
t_{fib} t_{myo}	0.70 0.38	0.85 0.38	0.85 0.38	0.90 0.38
no fibrosis	$D < 2.83$ $r_4 < 0.08$	$r_4 < 0.05$	$r_4 < 0.05$	$r_4 < 0.085$
interstitial	$D \geq 2.83$ $r_4 < 0.08$	$r_4 = [0.05, 0.21]$	$r_4 = [0.05, 0.21]$	$r_4 = [0.085, 0.24]$
compact	$r_4 \geq 0.50$	$D \geq 2.88$ $r_4 \geq 0.21$	$D \geq 2.83$ $r_4 \geq 0.21$	$D \geq 2.73$ $r_4 \geq 0.24$
diffuse	$D < 2.77$ $r_4 = [0.08, 0.50)$	$D < 2.81$ $r_4 \geq 0.21$	$D < 2.76$ $r_4 \geq 0.21$	$D < 2.64$ $r_4 \geq 0.24$
patchy	$D \geq 2.77$ $r_4 = [0.08, 0.50)$	$D = [2.81, 2.88)$ $r_4 \geq 0.21$	$D = [2.76, 2.83)$ $r_4 \geq 0.21$	$D = [2.64, 2.73)$ $r_4 \geq 0.24$
$N_{\text{corr,gt}}$ $n_{\text{corr,gt}}$	52 71%	52 71%	53 73%	54 74%

Table 12.11.: Image set IIb (110 images) - Concordantly classified images in absolute ($N_{\mathrm{corr},i}$) and relative ($n_{\mathrm{corr},i}$) numbers obtained with methods and ranges given in Table 12.10. In addition Krippendorff's coefficients $k_{\alpha,[i,j]}$ are given as measures of agreement between automated and experts ($[i,j] = 1,2,3$) classifications (single index i: comparison with one expert i, double index $[i,j]$: comparison with two experts i and j). The agreement between all three experts was found to be $k_{\alpha,\mathrm{IIb},3} = 0.70$ (see section 12.3.1).

	PTPM	PDM	PGM	HM
$N_{\mathrm{corr},1}$	66	66	68	71
$N_{\mathrm{corr},2}$	67	62	65	67
$N_{\mathrm{corr},3}$	62	69	69	72
$n_{\mathrm{corr},1}$	60%	60%	62%	65%
$n_{\mathrm{corr},2}$	61%	56%	59%	61%
$n_{\mathrm{corr},3}$	56%	63%	63%	65%
$k_{\alpha,1}$	0.50	0.48	0.51	0.54
$k_{\alpha,2}$	0.51	0.43	0.47	0.50
$k_{\alpha,3}$	0.45	0.51	0.51	0.55
$k_{\alpha,[1,2]}$	0.59	0.56	0.58	0.60
$k_{\alpha,[1,3]}$	0.58	0.59	0.60	0.63
$k_{\alpha,[2,3]}$	0.51	0.51	0.52	0.54

In Tables 12.12, 12.13, 12.15, and 12.16 the optimum thresholds and ranges of the fractal dimension D and collagen ratios r_3 and r_4 with thresholds for D assumed as linear functions of r_3, r_4 (see chapter 11.5.1) for an automated classification of the ground truth images to the different types of fibrosis (no fibrosis, interstitial, compact, diffuse, patchy) based on the applied fractal methods (PTPM, PDM, PGM (simple kernel), improved DBCM) are presented. Again DBCM yielded much worse results and is therefore not included in these tables. In addition to $N_{\text{corr,gt}}$ also the percentage of correctly classified ground truth images $n_{\text{corr,gt}}$ is given.

The investigated methods yielded comparable results with 78% to 82% (r_3) and 81% to 82% (r_4) correctly assigned ground truth images.

The optimum parameters were used for an automated classification of all images of image set IIb. In Tables 12.14 and 12.17 the obtained results are compared to classifications of each expert $i = 1, 2, 3$. In addition to absolute ($N_{\text{corr},i}$) and relative ($n_{\text{corr},i}$) numbers of concordantly assigned images, Krippendorff's coefficients $k_{\alpha,i}$ (comparison with one expert) and $k_{\alpha,[i,j]}$ (comparison with two experts) are given as measures of agreement between automated and experts classifications.

Comparable results were obtained for all investigated methods. Methods including collagen ratio r_3 resulted in 61% to 73% ($k_{\alpha,[\text{i,j}]}$: 0.57 to 0.67), methods including $r4$ in 62% to 71% ($k_{\alpha,[\text{i,j}]}$: 0.57 to 0.67) of all images assigned concordantly with the experts. The correlation between the diagnoses of the human experts and the best automated diagnosis with a pyramidal method (PGM,r_4) is shown in Tables A.26, A.27 and A.28 in the appendix A.3.2. Most disagreements occurred between the types *compact* and *patchy* (automated diagnosis yielded more often *patchy* instead of *compact* than vice versa), *no fibrosis* and *interstitial* (automated diagnosis yielded more often *interstitial* instead of *no fibrosis* than vice versa), and *interstitial* and *diffuse*.

Table 12.12.: Image set IIb - Optimized segmentation thresholds (t_{fib}, t_{lum}) and ranges of fractal dimension D and collagen ratio r_3 for an automated classification of the ground truth images to the different types of fibrosis (no fibrosis, interstitial, compact, diffuse, patchy) based on the applied fractal methods (PTPM, PDM). Thresholds for D were assumed as linear functions of r_3 (see chapter 11.5.1). $N_{\text{corr,gt}}$ denotes the absolute number, $n_{\text{corr,gt}}$ the percentage of correctly classified images of the 73 ground truth images of image set IIb.

	PTPM	PDM
t_{fib} t_{lum}	0.70 0.88	0.70 0.98
no fibrosis	$D = [2.810, 2.827]$ $r_3 < 0.022$	$D = [2.899, 2.909]$ $r_3 < 0.0168$
interstitial	$r_3 < 0.049$	$r_3 < 0.0474$
compact	$D \geq (-4.273 \cdot r_3 + 3.716)$ $r_3 \geq 0.049$	$D \geq (-4.3776 \cdot r_3 + 3.6458)$ $r_3 \geq 0.0474$
diffuse	$D < (-4.273 \cdot r_3 + 3.716)$ $D < 2.759$ $r_3 \geq 0.049$	$D < (-4.3776 \cdot r_3 + 3.6458)$ $D < 2.8386$ $r_3 \geq 0.0474$
patchy	$D < (-4.273 \cdot r_3 + 3.716)$ $D \geq 2.759$ $r_3 \geq 0.049$	$D < (-4.3776 \cdot r_3 + 3.6458)$ $D \geq 2.8386$ $r_3 \geq 0.0474$
$N_{\text{corr,gt}}$ $n_{\text{corr,gt}}$	59 81%	60 82%

Table 12.13.: Image set IIb - Optimized segmentation thresholds (t_{fib}, t_{lum}) and ranges of fractal dimension D and collagen ratio r_3 for an automated classification of the ground truth images to the different types of fibrosis (no fibrosis, interstitial, compact, diffuse, patchy) based on the applied fractal methods (PGM (simple kernel), HM). Thresholds for D were assumed as linear functions of r_3 (see chapter 11.5.1). $N_{\text{corr,gt}}$ denotes the absolute number, $n_{\text{corr,gt}}$ the percentage of correctly classified images of the 73 ground truth images of image set IIb.

	PGM	HM
t_{fib} t_{lum}	0.80 0.94	0.90 0.90
no fibrosis	$D = [2.801, 2.821]$ $r_3 < 0.034$	$D = [2.681, 2.713]$ $r_3 < 0.091$
interstitial	$r_3 < 0.082$	$r_3 < 0.13$
compact	$D \geq (-1.4 \cdot r_3 + 3.16)$ $r_3 \geq 0.082$	$D \geq (-0.18 \cdot r_3 + 2.77)$ $r_3 \geq 0.13$
diffuse	$D < (-1.4 \cdot r_3 + 3.16)$ $D < 2.768$ $r_3 \geq 0.082$	$D < (-0.18 \cdot r_3 + 2.77)$ $D < 2.64$ $r_3 \geq 0.13$
patchy	$D < (-1.4 \cdot r_3 + 3.16)$ $D \geq 2.768$ $r_3 \geq 0.082$	$D < (-0.18 \cdot r_3 + 2.77)$ $D \geq 2.64$ $r_3 \geq 0.13$
$N_{\text{corr,gt}}$ $n_{\text{corr,gt}}$	57 78%	60 82%

Table 12.14.: Image set IIb (110 images) - Concordantly classified images in absolute ($N_{\mathrm{corr},i}$) and relative ($n_{\mathrm{corr},i}$) numbers obtained with methods and ranges given in Tables 12.12 and 12.13. In addition Krippendorff's coefficients $k_{\alpha,[i,j]}$ are given as measures of agreement between automated and experts ($[i,j] = 1,2,3$) classifications (single index i: comparison with one expert i, double index $[i,j]$: comparison with two experts i and j). The agreement between all three experts was found to be $k_{\alpha,\mathrm{IIb},3} = 0.70$ (see section 12.3.1).

	PTPM	PDM	PGM	HM
$N_{\mathrm{corr},1}$	75	76	74	73
$N_{\mathrm{corr},2}$	68	70	67	72
$N_{\mathrm{corr},3}$	80	76	78	75
$n_{\mathrm{corr},1}$	68%	69%	67%	66%
$n_{\mathrm{corr},2}$	62%	64%	61%	65%
$n_{\mathrm{corr},3}$	73%	69%	71%	68%
$k_{\alpha,1}$	0.59	0.61	0.58	0.57
$k_{\alpha,2}$	0.51	0.54	0.50	0.56
$k_{\alpha,3}$	0.65	0.60	0.62	0.59
$k_{\alpha,[1,2]}$	0.62	0.63	0.61	0.63
$k_{\alpha,[1,3]}$	0.67	0.66	0.66	0.65
$k_{\alpha,[2,3]}$	0.58	0.57	0.56	0.58

Table 12.15.: Image set IIb - Optimized segmentation thresholds (t_{fib}, t_{myo}) and ranges of fractal dimension D and collagen ratio r_4 for an automated classification of the ground truth images to the different types of fibrosis (no fibrosis, interstitial, compact, diffuse, patchy) based on the applied fractal methods (PTPM, PDM). Thresholds of D were assumed as linear functions of r_4 (see chapter 11.5.1). $N_{\text{corr,gt}}$ denotes the absolute number, $n_{\text{corr,gt}}$ the percentage of correctly classified images of the 73 ground truth images of image set IIb.

	PTPM	PDM
t_{fib} t_{myo}	0.70 0.38	0.85 0.38
no fibrosis	$D = [2.810, 2.827]$ $r_4 < 0.032$	$D = [2.891, 2.917]$ $r_4 < 0.074$
interstitial	$r_4 < 0.085$	$r_4 < 0.18$
compact	$D \geq (-0.09 \cdot r_4 + 2.93)$ $r_4 \geq 0.085$	$D \geq (-0.075 \cdot r_4 + 2.97)$ $r_4 \geq 0.18$
diffuse	$D < (-0.09 \cdot r_4 + 2.93)$ $D < 2.76$ $r_4 \geq 0.085$	$D < (-0.075 \cdot r_4 + 2.97)$ $D < 2.82$ $r_4 \geq 0.18$
patchy	$D < (-0.09 \cdot r_4 + 2.93)$ $D \geq 2.76$ $r_4 \geq 0.085$	$D < (-0.075 \cdot r_4 + 2.97)$ $D \geq 2.82$ $r_4 \geq 0.18$
$N_{\text{corr,gt}}$ $n_{\text{corr,gt}}$	59 81%	59 81%

Table 12.16.: Image set IIb - Optimized segmentation thresholds (t_{fib}, t_{myo}) and ranges of fractal dimension D and collagen ratio r_4 for an automated classification of the ground truth images to the different types of fibrosis (no fibrosis, interstitial, compact, diffuse, patchy) based on the applied fractal methods (PGM (simple kernel), HM). Thresholds of D were assumed as linear functions of r_4 (see chapter 11.5.1). $N_{\text{corr,gt}}$ denotes the absolute number, $n_{\text{corr,gt}}$ the percentage of correctly classified images of the 73 ground truth images of image set IIb.

	PGM	HM
t_{fib} t_{myo}	0.85 0.38	0.90 0.38
no fibrosis	$D = [2.802, 2.822]$ $r_4 < 0.09$	$D = [2.674, 2.720]$ $r_4 < 0.12$
interstitial	$r_4 < 0.18$	$r_4 < 0.24$
compact	$D \geq (-0.08 \cdot r_4 + 2.92)$ $r_4 \geq 0.18$	$D \geq (-0.065 \cdot r_4 + 2.76)$ $r_4 \geq 0.24$
diffuse	$D < (-0.08 \cdot r_4 + 2.92)$ $D < 2.76$ $r_4 \geq 0.18$	$D < (-0.065 \cdot r_4 + 2.76)$ $D < 2.64$ $r_4 \geq 0.24$
patchy	$D < (-0.08 \cdot r_4 + 2.92)$ $D \geq 2.76$ $r_4 \geq 0.18$	$D < (-0.065 \cdot r_4 + 2.76)$ $D \geq 2.64$ $r_4 \geq 0.24$
$N_{\text{corr,gt}}$ $n_{\text{corr,gt}}$	59 81%	60 82%

Table 12.17.: Image set IIb (110 images) - Concordantly classified images in absolute ($N_{\mathrm{corr},i}$) and relative ($n_{\mathrm{corr},i}$) numbers obtained with methods and ranges given in Tables 12.15 and 12.16. In addition Krippendorff's coefficients $k_{\alpha,[i,j]}$ are given as measures of agreement between automated and experts ($[i,j] = 1,2,3$) classifications (single index i: comparison with one expert i, double index $[i,j]$: comparison with two experts i and j). The agreement between all three experts was found to be $k_{\alpha,\mathrm{IIb},3} = 0.70$ (see section 12.3.1).

	PTPM	PDM	PGM	HM
$N_{\mathrm{corr},1}$	75	75	76	78
$N_{\mathrm{corr},2}$	68	70	71	74
$N_{\mathrm{corr},3}$	68	76	78	77
$n_{\mathrm{corr},1}$	68%	68%	69%	71%
$n_{\mathrm{corr},2}$	62%	64%	65%	67%
$n_{\mathrm{corr},3}$	62%	69%	71%	70%
$k_{\alpha,1}$	0.59	0.59	0.61	0.63
$k_{\alpha,2}$	0.51	0.53	0.55	0.58
$k_{\alpha,3}$	0.65	0.60	0.63	0.61
$k_{\alpha,[1,2]}$	0.62	0.63	0.64	0.66
$k_{\alpha,[1,3]}$	0.67	0.66	0.67	0.67
$k_{\alpha,[2,3]}$	0.58	0.57	0.58	0.59

The agreement between human experts and the automated classification with the best performing pyramidal method (PGM, r_4, thresholds as given in Table 12.16) is illustrated graphically by comparing the results for the 99 tiles of the single whole-slide scan of image set IIb (see section 10.1.2, Figure 10.1). In Figure 12.16 the agreement between the human experts is depicted (71% to 86% agreement), Figure 12.17 shows the agreement between automated diagnosis and each human expert (67% to 74% agreement).

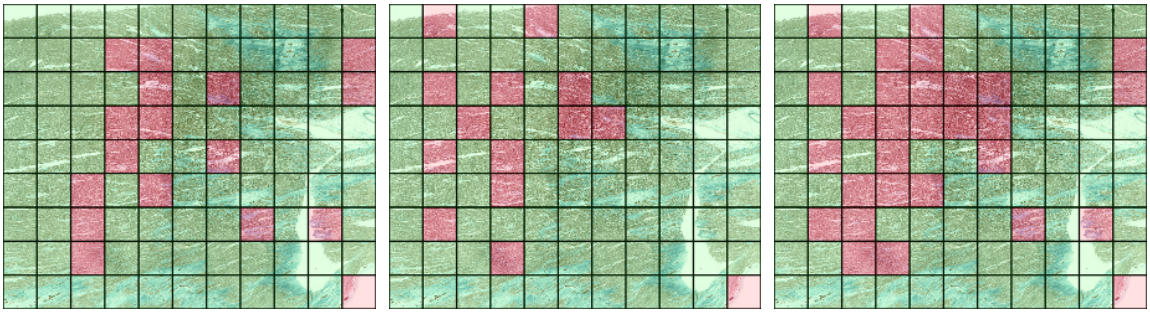

(a) Expert 1 vs. 2 **(b)** Expert 1 vs. 3 **(c)** Expert 2 vs. 3

Figure 12.16.: Illustration of the agreement between human experts 1,2 and 3 for the tiles of the single whole-slide scan of image set IIb (see section 10.1.2, Figure 10.1). The squares with green overlay indicate concordantly classified images, squares with red overlay indicate regions assigned to different types of fibrosis (5 classes: *no fibrosis*, *interstitial*, *compact*, *diffuse*, *patchy* fibrosis).

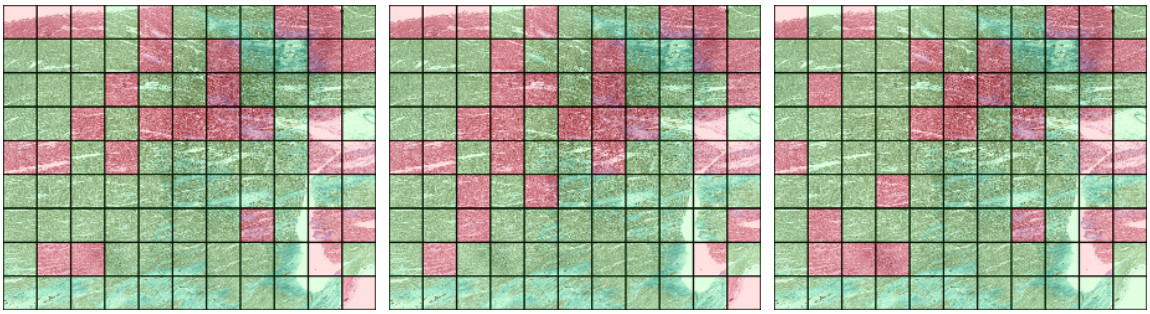

(a) Expert 1 vs. auto **(b)** Expert 2 vs. auto **(c)** Expert 3 vs. auto

Figure 12.17.: Illustration of the agreement between human experts (1,2,3) and automated diagnosis (PGM, r_4, thresholds as given in Table 12.16) for the tiles of the single whole-slide scan of image set IIb (see section 10.1.2, Figure 10.1). The squares with green overlay indicate concordantly classified images, squares with red overlay indicate regions assigned to different types of fibrosis (5 classes: *no fibrosis*, *interstitial*, *compact*, *diffuse*, *patchy* fibrosis).

13. Conclusion - Part II

The second part of this thesis presented the application of image analysis, especially fractal methods to histological images of the heart.

Firstly, image set I including 40 histological images (20 control, 20 fibrosis, stained with Masson's Trichrome) of human hearts that had suffered from ischemic heart disease was investigated. With two different segmentation algorithms (Colour Deconvolution, RGB Relative) and three different collagen ratios the amount of connective tissue was quantified. The results showed significantly higher amounts for the fibrosis group than for the control group. The binary Pyramid Method was used to calculate the fractal dimension D_{P} of the images. $D_{\mathrm{P}} = 1.65 \pm 0.10$ was obtained for the fibrosis group. This significantly different value compared to the control group is in the same range as values obtained for liver fibrosis[156].

Secondly, image sets IIa (70 images, Picrosirius Red) and IIb (110 images, Gieson's Trichrome) of human hearts showing myocardial fibrosis were investigated. Experts assigned the images to five different types of fibrosis (*no fibrosis*, *interstitial*, *compact*, *diffuse*, *patchy*). Concordantly classified images were used as ground truth. Collagen ratios (r_3: collagen vs. lumen; r_4: collagen vs. myocytes) and D-values based on the best-performing fractal dimension estimation algorithms evaluated in the first part of this thesis (PTPM, PDM, PGM, DBCM, HM) were calculated. An automated classification algorithm was developed and optimized by finding the best performing thresholds for collagen ratios (constant) and D-values (constant or linear function of collagen ratios) for the assignment rules for the ground truth images.

For image set IIa, significant differences between most of the different types of fibrosis were obtained for all but the HM. The best performing automated classification (r_3, PDM, linear function thresholds) resulted in 71% to 73% of all images assigned in accordance with the human experts (Krippendorff's coefficient $k_\alpha = 0.64 - 0.66$). The

accordance between the experts was better with 90% of all images classified concordantly ($k_{\alpha,\mathrm{IIa}} = 0.87$).

For image set IIb, significant differences between most of the different types of fibrosis were obtained for all but the DBCM. All methods based on thresholds for D-values as linear function of collagen ratios yielded the best results with 61% to 73% of all images assigned in accordance with the human experts (Krippendorff's coefficient $k_\alpha = 0.57 - 0.67$). The accordance between the experts was slightly better with $66 - 83\%$ of the images classified concordantly ($k_{\alpha,\mathrm{IIb},3} = 0.70$).

Most disagreements between automated and expert classification occurred between the types *compact* and *patchy* (automated diagnosis yielded more often *patchy* instead of *compact* than vice versa), *no fibrosis* and *interstitial* (automated diagnosis yielded more often *interstitial* instead of *no fibrosis* than vice versa), and *interstitial* and *diffuse*. Also the classifications of the experts showed their least agreements for exactly the same combinations.

Although the agreement between the human experts was better than for the developed automated diagnosis, it can be concluded that the presented results verified the second hypothesis proposed in this thesis: *The estimated fractal dimension of histological images can be used as a parameter for a classification of different types of myocardial fibrosis.*

Part III.

Conclusion and Outlook

14. Conclusion and Discussion

In the first part of this thesis the hypothesis *"Fractal dimensions of grey value images can be reliably estimated by a pyramidal approach. This pyramidal approach has shorter computational times than standard approaches."* was verified. Therefore three new pyramidal approaches for fractal dimension (D) estimation were developed and tested, namely the *Pyramid Triangular Prism Method* (PTPM), the *Pyramid Gradient Method* (PGM), and the *Pyramid Differences Method* (PDM). The new methods as well as five non-pyramidal methods were applied to artificially created images. It was shown that all new pyramidal methods yield reasonable D-values in rather fast computational times. Best results were obtained with the PDM with bilinear interpolation, which also showed fastest computational times in addition to its high agreement with theoretical D-values and D variation ranges.

In the second part of this thesis the new methods were applied to histological images of the human heart. The proposed automated classification algorithms used estimated fractal dimension values and two different collagen ratios to assign histological images of the myocardium to five different types of fibrosis. Tests were performed on two different image sets (IIa, IIb), which were stained with different colours (IIa: Picrosirius Red, IIb: Gieson's Trichrome). For image set IIa the best-performing automated classification utilized the PDM together with linear function thresholds and resulted in 71% to 73% of all images assigned in accordance with the human experts (Krippendorff's coefficient $k_\alpha = 0.64 - 0.66$). The accordance between the experts was better with 90% of all images classified concordantly ($k_{\alpha,\mathrm{IIa}} = 0.87$). For image set IIb all fractal methods and collagen ratios with linear function thresholds yielded comparable results with 61% to 73% of all images assigned in accordance with the human experts (Krippendorff's coefficient $k_\alpha = 0.57 - 0.67$). The accordance between the experts was slightly better with $66 - 83\%$ of the images classified concordantly ($k_{\alpha,\mathrm{IIb},3} = 0.70$). However, with these results the second hypothesis *"The estimated fractal dimension of histological*

images can be used as a parameter for a classification of different types of myocardial fibrosis.", was verified.

Since both the automated as well as the experts among each other showed main disagreements for the differentiation between *no fibrosis* and *interstitial*, *interstitial* and *diffuse*, and *compact* and *patchy*, an automated classification system based on values obtained from image analysis methods may actually result in more reproducible outcomes than a classification by humans.

14.1. Limitations of this Study

The three new pyramidal fractal dimension estimation algorithms were evaluated empirically by applying them to artificially created images. These artificially generated images were interpreted as images with known (theoretical) fractal dimensions, i.e. as representations of theoretical fractals. Since any digital image has the intrinsic property of not being able to replicate structures until infinity (finite image/pixel size, borders/discontinuities, ...), these artificial images can be at most seen as approximations to theoretical fractals. Thus the method of evaluating the algorithms by comparing their outcomes to theoretical values is debatable. However, similar approaches for estimating fractal dimensions were used successfully in the past, hence it seems reasonable to use this approach for the present study.

Furthermore, in this study fractal methods were only tested on square images, neglecting possible influences from rectangular shapes. Including all influences from non-square image sizes would lengthen every section, making definitions and descriptions more complicated and worsen readability. Since the intended audience of this thesis might have a more medical than mathematical background, the restriction to square images seems appropriate for this work.

The used collagen ratios were obtained by using rather simple image segmentation algorithms. Although this resulted in fast computation times, more advanced segmentation algorithms would probably improve the outcome.

Regarding the automated classification of myocardial fibrosis it has to be noted that fibrosis typically does not exhibit only one particular pattern type but may be a composition of the different types. Due to this fact it is obvious that although fibrosis is

often classified, a uniform and exact classification of different types of fibrosis is debatable. In addition, the images of set IIb showed a large percentage of longitudinal sections and just a few transverse sections which made a differentiation between the types difficult for the human experts - and maybe also for the developed automated classification algorithm. For that reason, to further improve statistics and to perfect the proposed automated classification algorithms, it would be desirable to use a larger number of images classified by experts.

15. Outlook

Especially because of the good results obtained with the new pyramidal fractal methods (PTPM, PDM, PGM), a more theoretical/mathematical description of them, probably based on the Hausdorff-Besicovitch Dimension would be desirable. Furthermore, extensive studies would be required to analyse influences from non-square image sizes or border effects.

For testing the proposed automated classification algorithm, a selection of images (IIa: 70, IIb: 110) out of the thousands of available images were used since an expert classification of all images would have been too laborious. However, in the future a higher number of classified images would improve the proposed automated classification algorithms. Furthermore, more advanced segmentation algorithms and optimization procedures to obtain rules for the assignment of the images to the different classes may also enhance the outcome.

Another important step would be to take a closer look at the images that could not be automatically assigned in accordance with the human experts. Together with experts, the classification rules could be revised to improve the automated classification system. Based on this improvement more reproducible results than obtained from different expert may be achieved.

The main future goal is to use the proposed techniques in practice in order to support researchers and pathologists. Hence a main next step is to integrate the methods in a user-friendly software package that can be easily used.

Danksagung

Zuallererst darf ich mich bei meinem Betreuer, Helmut Ahammer, sehr herzlich bedanken. Sein mir vermitteltes Fachwissen und seine Erfahrungen bildeten das Fundament für die hier vorliegende Arbeit. Weiters möchte ich seinen stets freundlichen, offenen und menschlichen Charakter hervorheben, an dem auch die Leidenschaft für seine Arbeit abzulesen ist. Besonders bedanke ich mich hierbei auch für die Freiheiten, die er mir in der Zeit unserer Zusammenarbeit gewährte.
Besonderer Dank gilt all jenen, die dazu beigetragen haben, dass ich mein Doktoratsstudium als eine wunderschöne Zeit in Erinnerung behalten werde. Als der Mannschaft vorort gilt dieser Dank dem "A(-Labor)-Team": Michi, Robert und Phil, ihr ward eine echte Bereicherung, durch eure fröhliche und lustige Art habe ich mich immer auf meine mehr als unregelmäßigen Besuche bei euch und meinem Arbeitsplatz gefreut. Auch die mehr als schweißtreibenden Ausflüge auf diverse Sportplätze und Videoabende mit den Coimbras werde ich nicht vergessen. Ganz zu schweigen von unserer Firmengründung in Berlin. Dank geht natürlich auch an Stefan und die NERDs 08, für lustige erste, zweite und dritte Halbzeiten. An Mani, der mich mehr als einmal und besonders in schwierigen Phasen in mehreren Ländern dieser Erde um- und versorgte. Dann gibt es natürlich auch noch Patrick, der die Stellung bei HÅNS gehalten hat und immer einen Teller Nudeln, einen Kaffee, ein Go-Brett oder einen Platz auf der Couch für mich bereithält. Ihr alle habt die Zeit meines Studiums bereichert, mich durch dunkle und helle Zeiten begleitet und ihr alle habt Anteil am Erfolg dieser Arbeit.
Auch wenn es nicht immer so schien, gab und gibt es auch ein Leben außerhalb von Graz - und weitere Menschen, bei denen ich mich bedanken möchte. Allen voran stehen hier natürlich meine Eltern Anna und Martin. Es ist unmöglich, in wenigen Sätzen zu beschreiben, für was und wie sehr ich mich bei euch bedanken will. Nur durch eure Hilfe habe ich es bis hierher geschafft. Ich darf nur hoffen, dass ich meinen eigenen Kindern ähnlich zur Seite stehen und für sie da sein kann, wie ihr das für mich getan habt.

Meinem Bruder Martin danke ich vor allem für die leider viel zu seltenen Gespräche, egal ob über (Koch-)Künste, Philosophen oder andere Themen des täglichen Seins. Es ist schön, einen Bruder wie dich zu haben, der immer da ist wenn man ihn braucht. Ich freue mich jedes Mal, wenn wir uns sehen, egal ob Thalgau, Hamburg, online oder sonst irgendwie oder irgendwo auf dieser Welt.
Lemur, dir danke ich dafür, dass du mir eine andere Sicht der Dinge, eine für mich neue, wunderschöne Welt gezeigt hast. Du hast mein Leben verändert und ich werde immer, wenn ich meine Augen schließe, das Glitzern in deinen Augen sehen. Möge die Sonne immer auf deine Insel und dein Fell scheinen.
Zum Abschluss möchte ich mich bei Gott bedanken. Erst mit dir macht alles Sinn. Danke.

Bibliography

[1] R. Lopes and N. Betrouni, *Fractal and multifractal analysis: A review* Medical Image Analysis **13**, 634 (2009).

[2] H. Ahammer and M. Mayrhofer-Reinhartshuber, *Image Pyramids for Calculation of the Box Counting Dimension* Fractals **20**, 281 (2012).

[3] E. Hofer, F. Keplinger, T. Thurner, T. Wiener, D. Sanchez-Quintana, V. Climent, and G. Plank, *A new floating sensor array to detect electric near fields of beating heart preparations* Biosensors and Bioelectronics **21**, 2232 (2006).

[4] R. Arnold, T. Wiener, D. Sanchez-Quintana, and E. Hofer, *Topology and Conduction in the Inferior Right Atrial Isthmus Measured in Rabbit Hearts* 33rd Annual International Conference of the IEEE EMBS pp. 247–250 (2011).

[5] T. Wiener, F. O. Campos, G. Plank, and E. Hofer, *Decomposition of fractionated local electrograms using an analytic signal model based on sigmoid functions* Biomedizinische Technik/Biomedical Engineering **57**, 371 (2012).

[6] F. O. Campos, A. J. Prassl, G. Seemann, R. Weber dos Santos, G. Plank, and E. Hofer, *Influence of ischemic core muscle fibers on surface depolarization potentials in superfused cardiac tissue preparations: a simulation study* Medical & Biological Engineering & Computing **50**, 461 (2012).

[7] F. O. Campos, T. Wiener, A. J. Prassl, H. Ahammer, G. Plank, R. Weber Dos Santos, D. Sánchez-Quintana, and E. Hofer, *A 2D-computer model of atrial tissue based on histographs describes the electro-anatomical impact of microstructure on endocardiac potentials and electric near-fields.* Conf Proc IEEE Eng Med Biol Soc **2010**, 2541 (2010).

[8] S. de Jong, T. A. van Veen, H. V. van Rijen, and J. M. de Bakker, *Fibrosis and Cardiac Arrhythmias* Journal of cardiovascular pharmacology **57**, 630 (2011).

[9] J. M. De Bakker and H. M. Van Rijen, *Continuous and Discontinuous Propagation in Heart Muscle* Journal of Cardiovascular Electrophysiology **17**, 567 (2006).

[10] S. Peleg, J. Naor, R. Hartley, and D. Avnir, *Multiple Resolution Texture Analysis and Classification* IEEE Transactions on Pattern Analysis and Machine Intelligence **PAMI-6**, 518 (1984).

[11] W. Burger and M. J. Burge, *Principles of Digital Image Processing* (Springer London, 2009).

[12] JPEG committee, *The JPEG committee home page* (2014), URL `http://www.jpeg.org/`.

[13] IJG, *Independent JPEG Group* (2014), URL `http://www.ijg.org/`.

[14] A. Goode, B. Gilbert, J. Harkes, D. Jukic, and M. Satyanarayanan, *OpenSlide: A vendor-neutral software foundation for digital pathology* Journal of Pathology Informatics **4**, 27 (2013).

[15] D. Forsberg, *MATLAB interface for OpenSlide*, http://www.medicalimagecomputing.net/software/openslide-matlab-toolbox-reading-whole-slide-images/ (2013).

[16] R. Keys, *Cubic convolution interpolation for digital image processing* Acoustics, Speech and Signal Processing, IEEE Transactions on **29**, 1153 (1981).

[17] I. Sun Microsystems, *Programming in Java™Advanced Imaging*, vol. 1.0.1 (Sun Microsystems, Inc., 901 San Antonio Road, Palo Alto, California 94303 U.S.A., 1999).

[18] S. Lloyd, *Least squares quantization in PCM* Information Theory, IEEE Transactions on **28**, 129 (1982).

[19] A. C. Ruifrok and D. A. Johnston, *Quantification of histochemical staining by color deconvolution.* Analytical and quantitative cytology and histology/the International Academy of Cytology [and] American Society of Cytology **23**, 291 (2001).

[20] B. B. Mandelbrot, *Fractals: Form, Chance and Dimension* (W.H.Freeman & Company, 1977), 1st ed.

[21] D. Paumgartner, G. Losa, and E. R. Weibel, *Resolution effect on the stereological estimation of surface and volume and its interpretation in terms of fractal dimensions.* J Microsc **121**, 51 (1981).

[22] B. B. Mandelbrot, *The Fractal Geometry of Nature : Updated and Augmented* (W. H. Freeman and Company, New York, 1983).

[23] C. Puente, J. Romeu, R. Pous, X. Garcia, and F. Benitez, *Fractal multiband antenna based on the Sierpinski gasket* Electronics Letters **32**, 1 (1996).

[24] D. H. Werner and S. Ganguly, *An overview of fractal antenna engineering research* IEEE Antennas and Propagation Magazine **45**, 38 (2003), ISSN 1045-9243.

[25] C. Mahatthanajatuphat, S. Saleekaw, and P. Akkaraekthalin, *A rhombic patch monopole antenna with modified Minkowski fractal geometry for UMTS, WLAN, and mobile WIMAX application* Progress in Electromagnetics Research-Pier **89**, 57 (2009).

[26] J. Ruis, *Design and Production of Scaffold for Artificial Blood Vessels (Tissue Engineering) by means of Rapid Prototyping using Fractal Geometry*, http://www.fractal.org/Fractal-Research-and-Products/Prototype-Fractal-Geometry.pdf (2007).

[27] J. E. Saik, M. K. McHale, and J. L. West, *Biofunctional materials for directing vascular development.* Curr Vasc Pharmacol **10**, 331 (2012).

[28] G. A. Losa, A. D. Ieva, F. Grizzi, and G. D. Vico, *On the fractal nature of nervous cell system* Frontiers in Neuroanatomy **5**, 45 (2011).

[29] S. Romand, Y. Wang, M. Toledo-Rodriguez, and H. Markram, *Morphological Development of Thick-Tufted Layer V Pyramidal Cells in the Rat Somatosensory Cortex* Frontiers in Neuroanatomy **5**, 5 (2011).

[30] G. B. West, *The importance of quantitative systemic thinking in medicine.* Lancet **379**, 1551 (2012).

[31] G. Landini, *Fractals in microscopy* Journal of Microscopy **241**, 1 (2011), ISSN 1365-2818.

[32] H. Ahammer, T. T. J. DeVaney, and H. A. Tritthart, *How much resolution is enough? Influence of downscaling the pixel resolution of digital images on the generalised dimensions* Physica D **181**, 147 (2003).

[33] H. Ahammer and T. T. J. DeVaney, *The influence of edge detection algorithms on the estimation of the fractal dimension of binary digital images.* Chaos **14**, 183 (2004).

[34] J. P. Sturmberg and B. J. West, in *Handbook of Systems and Complexity in Health* (Springer, 2013), pp. 171–192.

[35] E. R. Weibel, *Fractal geometry: a design principle for living organisms* American Journal of Physiology-Lung Cellular and Molecular Physiology **261**, L361 (1991).

[36] M. E. Dokukin, N. V. Guz, R. M. Gaikwad, C. D. Woodworth, , and I. Sokolov, *Cell Surface as a Fractal: Normal and Cancerous Cervical Cells Demonstrate Different Fractal Behavior of Surface Adhesion Maps at the Nanoscale* Phys. Rev. Lett. **107**, 028101 (2011).

[37] A. Di Ieva, F. Grizzi, C. Sherif, C. Matula, and M. Tschabitscher, *Angioarchitectural heterogeneity in human glioblastoma multiforme: A fractal-based histopathological assessment* Microvascular Research **81**, 222 (2011).

[38] H. F. Jelinek, D. Ristanovic, and N. T. Milosevic, *The morphology and classification of alpha ganglion cells in the rat retinae: a fractal analysis study.* J Neurosci Methods **201**, 281 (2011).

[39] F. N. Doubal, T. J. MacGillivray, N. Patton, B. Dhillon, M. S. Dennis, and J. M. Wardlaw, *Fractal analysis of retinal vessels suggests that a distinct vasculopathy causes lacunar stroke.* Neurology **74**, 1102 (2010).

[40] P. Di Giovanni, T. S. Ahearn, S. I. K. Semple, L. M. Lovell, I. Miller, F. J. Gilbert, T. W. Redpath, S. D. Heys, and R. T. Staff, *The biological correlates of macroscopic breast tumour structure measured using fractal analysis in patients undergoing neoadjuvant chemotherapy.* Breast Cancer Res Treat **133**, 1199 (2012).

[41] G. Soda, S. Nardoni, D. Bosco, F. Grizzi, N. Dioguardi, and M. Melis, *Fractal analysis of liver fibrosis* Pathologica **95**, 98 (2003).

[42] W.-C. Wu, H.-W. Chung, and H.-J. Chung, *Fractal analysis in liver fibrosis.* Hepatology **37**, 483 (2003).

[43] D. Mahmoud-Ghoneim, *Optimizing automated characterization of liver fibrosis histological images by investigating color spaces at different resolutions* Theoretical Biology and Medical Modelling **8**, 1 (2011).

[44] P. Calès, J. Boursier, J. Chaigneau, F. Lainé, J. Sandrini, S. Michalak, I. Hubert, N. Dib, F. Oberti, S. Bertrais, et al., *Diagnosis of different liver fibrosis characteristics by blood tests in non-alcoholic fatty liver disease.* Liver Int **30**, 1346 (2010).

[45] F. Moal, D. Chappard, J. Wang, E. Vuillemin, S. Michalak-Provost, M. C. Rousselet, F. Oberti, and P. Calès, *Fractal dimension can distinguish models and pharmacologic changes in liver fibrosis in rats.* Hepatology **36**, 840 (2002).

[46] M. F. Barnsley, *Fractals Everywhere* (Morgan Kaufmann, 1993), 2nd ed.

[47] L. S. Liebovitch, *Fractals and Chaos Simplified for the Life Sciences* (Oxford University Press, 1998).

[48] L. F. Richardson, *The problem of contiguity* General systems yearbook **6**, 139 (1961).

[49] B. B. Mandelbrot, *How long is the coast of Britain* Science **156**, 636 (1967).

[50] C. Carethéodory, *Über das lineare Maßvon Punktmengen - eine Verallgemeinerung das Längenbegriffs* Nachrichten der K. Gesellschaft der Wissenschaften zu Göttingen. Mathematisch-physikalische Klasse pp. 404–426 (1914).

[51] F. Hausdorff, *Dimension und äußeres Maß* Mathematische Annalen **79**, 157 (1918).

[52] A. Besicovitch, *On Linear Sets of Points of Fractional Dimension* Mathematische Annalen **101**, 161 (1929).

[53] K. J. Falconer, *Fractal Geometry - Mathematical Foundations and Applications* (John Wiley & Sons, Ltd, West Sussex, England, 2003).

[54] K. J. Falconer, *Fraktale Geometrie : Mathematische Grundlagen und Anwendungen* (Spektrum Akademischer Verlag, Heidelberg, Berlin, Oxford, 1993).

[55] J. M. Keller, S. Chen, and R. M. Crownover, *Texture Description and Segmentation through Fractal Geometry* Computer Vision, Graphics, and Image Processing **45**, 150 (1989).

[56] R. Lopes, P. Dubois, I. Bhouri, M. H. Nedoui, S. Maouche, and N. Betrouni, *Local fractal and multifractal features for volumic texture characterization* Pattern Recognition **44**, 1690 (2011).

[57] D. Adams, *Life, the Universe and Everything (The Hitchhiker's Guide to the Galaxy - III)* (Del Rey, 1995).

[58] D. A. Russell, J. D. Hanson, and E. Ott, *Dimension of Strange Attractors* Physical Review Letters **45**, 1175 (1980).

[59] F. Normant and C. Tricot, *Method for evaluating the fractal dimension of curves using convex hulls* Phys. Rev. A **43**, 6518 (1991).

[60] S. Appleby, *Multifractal Characterization of the Distribution Pattern of the Human Population* Geographical Analysis **28**, 147 (1996).

[61] S. A. Pruess, *Fractals in the Earth Sciences* (Plenum Press, 1995), chap. Some remarks on the numerical estimation of fractal dimension, pp. 65–75.

[62] R. Higgs, *Imaging: Fractal analysis for CHD mortality.* Nature Reviews Cardiology **8**, 62 (2011).

[63] A. C. Sullivan, J. P. Hunt, and A. L. Oldenburg, *Fractal analysis for classification of breast carcinoma in optical coherence tomography.* J Biomed Opt **16**, 066010 (2011).

[64] C. A. Pickover and A. Khorasani, *Fractal characterization of speech waveform graphs* Computers & Graphics **10**, 51 (1986).

[65] A. K. Bisoi and J. Mishra, *On calculation of fractal dimension of images* Pattern Recognition Letters **22**, 631 (2001).

[66] P. Asvestas, G. K. Matsopoulos, and K. S. Nikita, *A Power Differentiation Method of Fractal Dimension Estimation for 2-D Signals* Journal of Visual Communication and Image Representation **9**, 392 (1998).

[67] W.-L. Lee and K.-S. Hsieh, *A robust algorithm for the fractal dimension of images and its applications to the classification of natural images and ultrasonic liver images* Signal Processing **90**, 1894 (2010).

[68] M. Mayrhofer-Reinhartshuber, P. Kainz, and H. Ahammer, in *Proceedings of the 2013* 2$^{\text{nd}}$ *International Conference of Pattern Recognition Applications and Methods* (INSTICC, 2013), pp. 239–243.

[69] N. Sarkar and B. B. Chaudhuri, *An efficient approach to estimate fractal dimension of textural images* Pattern Recognition **25**, 1035 (1992).

[70] B. B. Chaudhuri and N. Sarkar, *Texture Segmentation using fractal dimension* IEEE Transactions on Pattern Analysis and Machine Intelligence **17**, 72 (1995).

[71] N. Sarkar and B. B. Chaudhuri, *Multifractal and generalized dimensions of gray-tone digital images* Signal Processing **42**, 181 (1995).

[72] M. K. Biswas, T. Ghose, S. Guha, and P. K. Biswas, *Fractal dimension estimation for texture images: A parallel approach* Pattern Recognition Letters **19**, 309 (1998).

[73] N. Sarkar and B. Chaudhuri, *An efficient differential box-counting approach to compute fractal dimension of image* Systems, Man and Cybernetics, IEEE Transactions on **24**, 115 (1994).

[74] W.-S. Chen, S.-Y. Yuan, and C.-M. Hsieh, *Two algorithms to estimate fractal dimension of gray-level images* Optical Engineering **42**, 2452 (2003).

[75] X. C. Jin, S. H. Ong, and Jayasooriah, *A practical method for estimating fractal dimension* Pattern Recognition Letters **16**, 457 (1995).

[76] J. Li, Q. Du, and C. Sun, *An improved box-counting method for image fractal dimension estimation* Pattern Recognition **42**, 2460 (2009).

[77] M. Aguilar, E. Anguiano, and M. Pancorbo, *Fractal characterization by frequency analysis. II. A new method* Journal of Microscopy **172**, 233 (1993).

[78] E. Anguiano, M. Pancorbo, and M. Aguilar, *Fractal characterization by frequency analysis. I. Surfaces* Journal of Microscopy **172**, 223 (1993).

[79] H. Ahammer, J. Kröpfl, C. Hackl, and R. Sedivy, *Fractal dimension and image statistics of anal intraepithelial neoplasia* Chaos, Solitons & Fractals **44**, 86 (2011).

[80] R. F. Voss, in *Fundamental algorithms for computer graphics* (Springer, 1991), pp. 805–835.

[81] T. Higuchi, *Approach to an irregular time series on the basis of the fractal theory* Physica D: Nonlinear Phenomena **31**, 277 (1988).

[82] H. Ahammer, *Higuchi dimension of digital images.* PLoS One **6**, e24796 (2011).

[83] S. Spasić, *On 2D generalization of HiguchiŠs fractal dimension* Chaos, Solitons & Fractals **69**, 179 (2014).

[84] H. Ahammer, N. Sabathiel, and M. A. Reiss, *Is a two-dimensional generalization of the Higuchi algorithm really necessary?* Chaos: An Interdisciplinary Journal of Nonlinear Science **25**, 073104 (2015).

[85] Y. Y. Tang, Y. Tao, and E. C. M. Lam, *New Method for Feature Extraction based on Fractal Behavior* Pattern Recognition **35**, 1071 (2002).

[86] B. Dubuc, S. Zucker, C. Tricot, J. Quiniou, and D. Wehbi, *Evaluating the Fractal Dimension of Surfaces* Proc. R. Soc. Lond. A **425**, 113 (1989).

[87] S. Novianto, Y. Suzuki, and J. Maeda, *Near optimum estimation of local fractal dimension for image segmentation* Pattern Recognition Letters **24**, 365 (2003).

[88] P. Brodatz, *Textures: a photographic album for artists and designers* (Dover Pubns, 1966).

[89] K. C. Clarke, *Computation of the fractal dimension of topographic surfaces using the triangular prism surface area method* Computers & Geosciences **12**, 713 (1986).

[90] S. Jaggi, D. A. Quattrochi, and N. S.-N. Lam, *Implementation and operation of three fractal measurement algorithms for analysis of remote-sensing data* Computers & Geosciences **19**, 745 (1993).

[91] W. Zhao, Ph.D. thesis, Louisiana State University, Louisiana, USA (2001).

[92] N. S.-N. Lam, H.-l. Qiu, D. A. Quattrochi, and C. W. Emerson, *An Evaluation of Fractal Methods for Characterizing Image Complexity* Cartography and Geographic Information Science **29**, 25 (2002).

[93] G. Zhou and N. S.-N. Lam, *A comparison of fractal dimension estimators based on multiple surface generation algorithms* Computers & Geosciences **31**, 1260 (2005).

[94] M. C. Shelberg, N. Lam, and H. Moellering, Tech. Rep., DTIC Document (1983).

[95] M. F. Goodchild, *Fractals and the accuracy of geographical measures* Journal of the International Association for Mathematical Geology **12**, 85 (1980).

[96] R. Voss, in *The Science of Fractal Images*, edited by H.-O. Peitgen and D. Saupe (Springer New York, 1988), pp. 21–70.

[97] J. R. Parker, *Algorithms for image processing and computer vision* (John Wiley & Sons, 1997).

[98] W. Ju and N. S.-N. Lam, *An improved algorithm for computing local fractal dimension using the triangular prism method* Computers & Geosciences **35**, 1224 (2009).

[99] W. Sun, *Three new implementations of the triangular prism method for computing the fractal dimension of remote sensing images* Photogrammetric Engineering & Remote Sensing **72**, 373 (2006).

[100] G. Chinga, P. O. Johnsen, R. Dougherty, E. L. Berli, and J. Walter, *Quantification of the 3D microstructure of SC surfaces* Journal of microscopy **227**, 254 (2007).

[101] I. Sobel, *An isotropic 3× 3 image gradient operator* (Academic Press, Boston, MA, 1990).

[102] T. Witten Jr and L. M. Sander, *Diffusion-limited aggregation, a kinetic critical phenomenon* Physical review letters **47**, 1400 (1981).

[103] P. Kainz, M. Mayrhofer-Reinhartshuber, and H. Ahammer, *IQM: An Extensible and Portable Open Source Application for Image and Signal Analysis in Java* PLoS ONE **10**, e0116329 (2015).

[104] A. Fournier, D. Fussell, and L. Carpenter, *Computer Rendering of Stochastic Models* Commun. ACM **25**, 371 (1982).

[105] D. Saupe, in *The Science of Fractal Images*, edited by H.-O. Peitgen and D. Saupe (Springer New York, 1988), pp. 71–136.

[106] I. Marák, *On Synthetic Terrain Erosion Modeling: A Survey* Proc. of CESCG **97** (1997).

[107] M. J. Turner, J. M. Blackledge, and P. R. Andrews, *Fractal geometry in digital imaging* (Academic Press, San Diego, California, 1998).

[108] M. Hata, in *Patterns and Waves Qualitative Analysis of Nonlinear Differential Equations*, edited by M. M. Takaaki Nishida and H. Fujii (Elsevier, 1986), vol. 18 of *Studies in Mathematics and Its Applications*, pp. 259 – 278.

[109] N. Kôno, *On self-affine functions* Japan Journal of Applied Mathematics **3**, 259 (1986).

[110] B. Dubuc, J. F. Quiniou, C. Roques-Carmes, C. Tricot, and S. W. Zucker, *Evaluating the fractal dimension of profiles* Phys. Rev. A **39**, 1500 (1989).

[111] H. Qiu, N. S.-N. Lam, D. A. Quattrochi, and J. A. Gamon, *Fractal characterization of hyperspectral imagery* Photogrammetric Engineering and Remote Sensing **65**, 63 (1999).

[112] P. Viola and M. Jones, in *Proceedings of the 2001 IEEE Computer Society Conference on Computer Vision and Pattern Recognition, 2001. CVPR 2001.* (IEEE, 2001), vol. 1, pp. I–511.

[113] P. Viola and M. Jones, *Robust Real-Time Face Detection* International Journal of Computer Vision **57**, 137 (2004).

[114] R. Arnold, Ph.D. thesis, Medizinische Universität Graz (2013).

[115] J. S. Robb and R. C. Robb, *The normal heart: anatomy and physiology of the structural units* American Heart Journal **23**, 455 (1942).

[116] L. C. Junqueira, J. Carneiro, R. O. Kelley, and M. Gratzl, *Histologie*, vol. 7 (Springer, 2005).

[117] S. K. White, D. M. Sado, A. S. Flett, and J. C. Moon, *Characterising the myocardial interstitial space: the clinical relevance of non-invasive imaging* Heart **98**, 773 (2012).

[118] F. J. Manasek, *Macromolecules of the extracellular compartment of embryonic and mature hearts.* Circulation Research **38**, 331 (1976).

[119] K. T. Weber, *Cardiac interstitium in health and disease: The fibrillar collagen network* Journal of the American College of Cardiology **13**, 1637 (1989), ISSN 0735-1097, {ACC} Anniversary Seminar.

[120] R. I. Bashey, A. Martinez-Hernandez, and S. A. Jimenez, *Isolation, characterization, and localization of cardiac collagen type VI. Associations with other extracellular matrix components.* Circulation Research **70**, 1006 (1992).

[121] I. Banerjee, J. W. Fuseler, R. L. Price, T. K. Borg, and T. A. Baudino, *Determination of cell types and numbers during cardiac development in the neonatal and adult rat and mouse* American Journal of Physiology - Heart and Circulatory Physiology **293**, H1883 (2007).

[122] J. Baum and H. S. Duffy, *Fibroblasts and myofibroblasts: what are we talking about?* Journal of cardiovascular pharmacology **57**, 376 (2011).

[123] C. A. Souders, S. L. Bowers, and T. A. Baudino, *Cardiac Fibroblast: The Renaissance Cell* Circulation Research **105**, 1164 (2009).

[124] T. A. Baudino, W. Carver, W. Giles, and T. K. Borg, *Cardiac fibroblasts: friend or foe?* American Journal of Physiology - Heart and Circulatory Physiology **291**, H1015 (2006).

[125] J. C. Moon, E. Reed, M. N. Sheppard, A. G. Elkington, S. Ho, M. Burke, M. Petrou, and D. J. Pennell, *The histologic basis of late gadolinium enhancement cardiovascular magnetic resonance in hypertrophic cardiomyopathy* Journal of the American College of Cardiology **43**, 2260 (2004).

[126] R. Querejeta, B. López, A. González, E. Sánchez, M. Larman, J. L. Martínez Ubago, and J. Díez, *Increased Collagen Type I Synthesis in Patients With Heart Failure of Hypertensive Origin: Relation to Myocardial Fibrosis* Circulation **110**, 1263 (2004).

[127] H. P. Krayenbuehl, O. M. Hess, E. S. Monrad, J. Schneider, G. Mall, and M. Turina, *Left ventricular myocardial structure in aortic valve disease before, intermediate, and late after aortic valve replacement.* Circulation **79**, 744 (1989).

[128] B. Benito, G. Gay-Jordi, A. Serrano-Mollar, E. Guasch, Y. Shi, J.-C. Tardif, J. Brugada, S. Nattel, and L. Mont, *Cardiac Arrhythmogenic Remodeling in a Rat Model of Long-Term Intensive Exercise Training* Circulation **123**, 13 (2011).

[129] S. de Jong, T. Veen, J. Bakker, and H. Rijen, *Monitoring cardiac fibrosis: a technical challenge* Netherlands Heart Journal **20**, 44 (2012).

[130] V. M. Almaas, K. H. Haugaa, E. H. Strøm, H. Scott, C. P. Dahl, T. P. Leren, O. R. Geiran, K. Endresen, T. Edvardsen, S. Aakhus, et al., *Increased amount of interstitial fibrosis predicts ventricular arrhythmias, and is associated with reduced myocardial septal function in patients with obstructive hypertrophic cardiomyopathy* Europace **15**, 1319 (2013).

[131] H. Puchtler and H. Isler, *The effect of phosphomolybdic acid on the stainability of connective tissue by various dyes* Journal of Histochemistry & Cytochemistry **6**, 265 (1958).

[132] F. Sweat, H. Puchtler, and S. I. Rosenthal, *Sirius red F3BA as a stain for connective tissue* Archives of pathology **78**, 69 (1964).

[133] H. Puchtler, F. S. Waldrop, and L. S. Valentine, *Polarization Microscopic Studies of Connective Tissue Stained with Picro-Sirius Red {FBA}* Beiträge zur Pathologie **150**, 174 (1973).

[134] L. Junqueira, G. Bignolas, and R. Brentani, *Picrosirius staining plus polarization microscopy, a specific method for collagen detection in tissue sections* The Histochemical Journal **11**, 447 (1979).

[135] P. Whittaker, R. Kloner, D. Boughner, and J. Pickering, *Quantitative assessment of myocardial collagen with picrosirius red staining and circularly polarized light* Basic Research in Cardiology **89**, 397 (1994).

[136] L. Rich and P. Whittaker, *Collagen and picrosirius red staining: a polarized light assessment of fibrillar hue and spatial distribution* Braz J Morphol Sci **22**, 97 (2005).

[137] D. Daunoravicius, J. Besusparis, E. Zurauskas, A. Laurinaviciene, D. Bironaite, S. Pankuweit, B. Plancoulaine, P. Herlin, J. Bogomolovas, V. Grabauskiene, et al., *Quantification of myocardial fibrosis by digital image analysis and interactive stereology* Diagnostic Pathology **9**, 114 (2014).

[138] R. A. Berg and D. J. Prockop, *The thermal transition of a non-hydroxylated form of collagen. Evidence for a role for hydroxyproline in stabilizing the triple-helix of collagen* Biochemical and Biophysical Research Communications **52**, 115 (1973).

[139] E. J. Miller, *Structural studies on cartilage collagen employing limited cleavage and solubilization with pepsin* Biochemistry **11**, 4903 (1972).

[140] K. N. Krahn, C. V. Bouten, S. van Tuijl, M. A. van Zandvoort, and M. Merkx, *Fluorescently labeled collagen binding proteins allow specific visualization of collagen in tissues and live cell culture* Analytical Biochemistry **350**, 177 (2006).

[141] S. de Jong, T. A. van Veen, J. M. de Bakker, M. A. Vos, and H. V. van Rijen, *Biomarkers of myocardial fibrosis* Journal of cardiovascular pharmacology **57**, 522 (2011).

[142] C. Prinz, M. Farr, K. T. Laser, H. Esdorn, C. Piper, D. Horstkotte, and L. Faber, *Determining the role of fibrosis in hypertrophic cardiomyopathy* pp. 495–504 (2013).

[143] T. Treibel, S. White, and J. Moon, *Myocardial Tissue Characterization: Histological and Pathophysiological Correlation* Current Cardiovascular Imaging Reports **7**, 1 (2014).

[144] A. S. Flett, J. Hasleton, C. Cook, D. Hausenloy, G. Quarta, C. Ariti, V. Muthurangu, and J. C. Moon, *Evaluation of techniques for the quantification of myocardial scar of differing etiology using cardiac magnetic resonance* JACC: cardiovascular imaging **4**, 150 (2011).

[145] S. de Jong, J. J. Zwanenburg, F. Visser, R. van der Nagel, H. V. van Rijen, M. A. Vos, J. M. de Bakker, and P. R. Luijten, *Direct detection of myocardial fibrosis by {MRI}* Journal of Molecular and Cellular Cardiology **51**, 974 (2011).

[146] M. Pop, N. R. Ghugre, V. Ramanan, L. Morikawa, G. Stanisz, A. J. Dick, and G. A. Wright, *Quantification of fibrosis in infarcted swine hearts by ex vivo late gadolinium-enhancement and diffusion-weighted MRI methods* Physics in Medicine and Biology **58**, 5009 (2013).

[147] R. Fernández-Jiménez, L. Fernández-Friera, J. Sánchez-González, and B. Ibáñez, *Animal Models of Tissue Characterization of Area at Risk, Edema and Fibrosis* Current Cardiovascular Imaging Reports **7**, 1 (2014).

[148] T. Stanton, R. Leano, and T. H. Marwick, *Prediction of All-Cause Mortality From Global Longitudinal Speckle Strain: Comparison With Ejection Fraction and Wall Motion Scoring* Circulation: Cardiovascular Imaging **2**, 356 (2009).

[149] M. Ersbøll, N. Valeur, U. M. Mogensen, M. J. Andersen, J. E. Møller, E. J. Velazquez, C. Hassager, P. Søgaard, and L. Køber, *Prediction of all-cause mortality and heart failure admissions from global left ventricular longitudinal strain in patients with acute myocardial infarction and preserved left ventricular ejection fraction* Journal of the American College of Cardiology **61**, 2365 (2013).

[150] B. A. Popescu and M. Roşca, *Imaging of myocardial fibrosis in hypertrophic cardiomyopathy: what is the gold standard?* Heart **100**, 605 (2014).

[151] M. Mayrhofer-Reinhartshuber, P. Kainz, D. Sanchez-Quintana, Y. Macias, E. Hofer, and H. Ahammer, *Semi-Automated Detection and Fractal Characterization of Myocardial Fibrosis in Histological Images* Biomedizinische Technik/Biomedical Engineering **59**, S616 (2014).

[152] K. Krippendorff, *Estimating the Reliability, Systematic Error and Random Error of Interval Data* Educational and Psychological Measurement **30**, 61 (1970).

[153] A. F. Hayes and K. Krippendorff, *Answering the call for a standard reliability measure for coding data* Communication Methods and Measures **1**, 77 (2007).

[154] K. Krippendorff, *Computing Krippendorff's alpha reliability* Departmental papers (ASC) p. 43 (2011), retrieved from `http://repository.upenn.edu/asc_papers/43`.

[155] A. M. Hadi, K. T. Mouchaers, I. Schalij, K. Grunberg, G. A. Meijer, A. Vonk-Noordegraaf, W. J. Laarse, and J. Beliën, *Rapid quantification of myocardial fibrosis: a new macro-based automated analysis* Cellular Oncology **34**, 343 (2011).

[156] F. Grizzi, C. Russo, B. Franceschini, M. Di Rocco, V. Torri, E. Morenghi, L. R. Fassati, and N. Dioguardi, *Sampling variability of computer-aided fractal-corrected measures of liver fibrosis in needle biopsy specimens* World J Gastroenterol **12**, 7660 (2006).

[157] J. Coulton, *Where Tradition Meets Tomorrow* (EP, 2004), chap. Mandelbrot Set.

Appendix

A.1. Staining Protocols

A.1.1. Sirius Red Staining Protocol

- Deparaffinize and rehydrate
- Wash in distilled water
- Stain with solution of Celestine Blue - 7 min
  Celestine Blue: 50 ml of 5% alum feather + 0.25 g Celestine Blue:
  cook 3 min, then filter and add 7 ml glycerol
- Transfer sections directly into Haematoxylin (German: *Hämalaun*) - 7 min
- Differentiate shortly inhydrochloric acid
- Blueing - 5-10 min
- Stain with Picrosirius Red (0.1% Siriusred (*Siriusrot F3BA Chroma 1 A 280*) in saturated picric acid (15 g picric acid + 950 ml distilled water)) - 30 min
- Dehydrate in three changes of 100% ethanol
- Clear in xylene and mount in a resinous medium

A.1.2. Gieson's Trichrome Staining Protocol

- Deparaffinize and rehydrate
- Wash in distilled water
- Stain with Gieson's dye - 2 min
- Blueing with hot water - 5 min
- 0.5% - 1% acetic acid - 1 min
- Blueing with hot water - 5 min
- Stain with trichrome solution (1 part solution A + 3 parts solution B)- 5 min
  solution A: 1 g Fuchsine acid + 0.5 ml acetic acid + 100 ml distilled water
  solution B: 1 g Ponceau de Xylidine + 1 ml acetic acid + 100 ml distilled water
- Rinse shortly in distilled water
- Drop phosphomolybdic acid on the sections - 1 min
- Physically remove liquid, no rinsing
- Drop Aniline Blue acid on the sections - 1 min
  Aniline Blue acid: 0.5 g Anilin Blue + 2.5 ml acetic acid + 100 ml dist. water
- Rinse in distilled water
- Dehydrate through alcohol with increasing concentration
- Mount in a resinous medium

A.2. Evaluation of Fractal Algorithms

In the following Tables A.1-A.19 the results of the grey value image fractal dimension D estimation methods are given for the three best, individually optimized scale-ranges. Optimization was performed by minimizing the root-mean-square deviation (RMSD) of the estimated and theoretically known D-values of the artificially created images over all three generators (Midpoint Displacement (MD), Fourier Filtering (FFT), Takagi Surfaces (Takagi)), separately for each image size. The quality of fit of the linear regression model (see section 4.1.1) is given as the coefficient of determination R^2. For each method exemplary log-log plots are shown (Figures A.1-A.19). In these figures, measures obtained for three different images (theoretical D-values: 2.1, 2.5, and 2.9, created with MD, 2048×2048 pixels) are given together with the over all generators and image sizes optimized scale-ranges and the corresponding linear regressions.

A.2.1. Box-Counting Methods

Table A.1.: RMSD and R^2 fit for the three best scale ranges obtained with the standard DBCM for each image size separately given for each generator (MD, FFT, Takagi). The scale values are given as exponents of 2, i.e. scales$= 4-8 \rightarrow s = 2^4 - 2^8$.

		MD		FFT		Takagi	
image size	scales	RMSD	R^2 fit	RMSD	R^2 fit	RSMD	R^2 fit
512×512	$4-8$	0.16	0.99 ± 0.01	0.16	0.99 ± 0.01	0.14	0.99
	$3-8$	0.17	0.99 ± 0.01	0.15	0.99 ± 0.01	0.15	0.99
	$5-8$	0.15	0.99 ± 0.01	0.18	0.99 ± 0.01	0.14	0.99
1024×1024	$4-9$	0.14	0.99 ± 0.01	0.15	0.99 ± 0.01	0.13	0.99
	$5-8$	0.15	0.99 ± 0.01	0.14	0.99 ± 0.01	0.13	0.99
	$5-9$	0.14	0.99 ± 0.01	0.16	0.99 ± 0.01	0.13	0.99
2048×2048	$5-8$	0.13	0.99 ± 0.01	0.12	0.99 ± 0.01	0.11	0.99
	$4-10$	0.13	0.99 ± 0.01	0.13	0.99 ± 0.01	0.12	0.99
	$5-9$	0.14	0.99 ± 0.01	0.13	0.99 ± 0.01	0.12	0.99
4096×4096	$5-8$	0.11	0.99 ± 0.01	0.11	0.99 ± 0.01	0.11	0.99
	$5-9$	0.12	0.99 ± 0.01	0.11	0.99 ± 0.01	0.10	0.99
	$6-9$	0.12	0.99 ± 0.01	0.12	0.99 ± 0.01	0.10	0.99

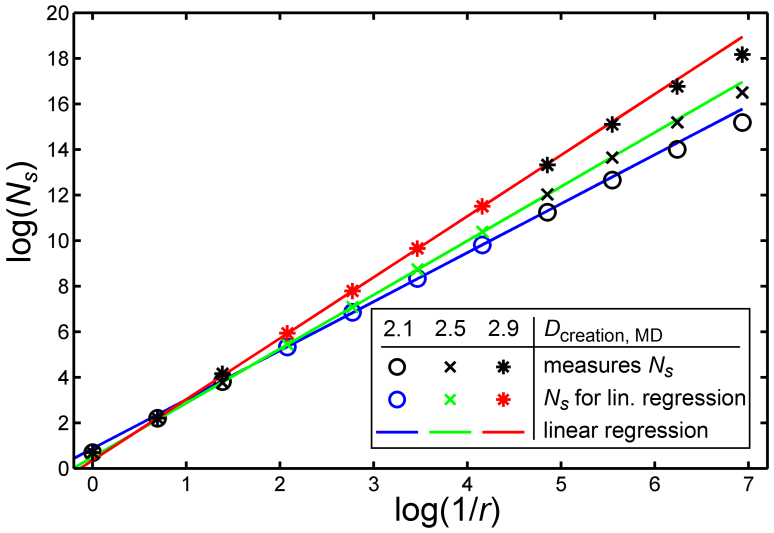

Figure A.1.: Exemplary log-log plot showing measures (N_s, scaling variable r) obtained with the standard DBCM for three different images (theoretical D-values: 2.1 (circles), 2.5 (crosses), and 2.9 (stars), created with MD, 2048×2048 pixels). Coloured markers indicate optimized scale-ranges that were used for fitting linear regressions (solid lines).

Table A.2.: RMSD and R^2 fit for the three best scale ranges obtained with the improved DBCM for each image size separately given for each generator (MD, FFT, Takagi). The scale values are given as exponents of 2, i.e. scales= $4-8 \rightarrow s = 2^4 - 2^8$.

		MD		FFT		Takagi	
image size	scales	RMSD	R^2 fit	RMSD	R^2 fit	RSMD	R^2 fit
512×512	$4-7$	0.11	0.99 ± 0.01	0.16	0.99 ± 0.01	0.11	0.99
	$3-8$	0.12	0.99 ± 0.01	0.16	0.99 ± 0.01	0.11	0.99
	$4-8$	0.10	0.99 ± 0.01	0.18	0.99 ± 0.01	0.11	0.99
1024×1024	$4-8$	0.10	0.99 ± 0.01	0.14	0.99 ± 0.01	0.10	0.99
	$4-7$	0.10	0.99 ± 0.01	0.13	0.99 ± 0.01	0.11	0.99
	$5-8$	0.08	0.99 ± 0.01	0.16	0.99 ± 0.01	0.09	0.99
2048×2048	$5-8$	0.08	0.99 ± 0.01	0.13	0.99 ± 0.01	0.09	0.99
	$4-9$	0.09	0.99 ± 0.01	0.13	0.99 ± 0.01	0.09	0.99
	$5-9$	0.08	0.99 ± 0.01	0.14	0.99 ± 0.01	0.09	0.99
4096×4096	$5-9$	0.07	0.99 ± 0.01	0.12	0.99 ± 0.01	0.08	0.99
	$5-8$	0.08	0.99 ± 0.01	0.11	0.99 ± 0.01	0.09	0.99
	$6-9$	0.07	0.99 ± 0.01	0.13	0.99 ± 0.01	0.07	0.99

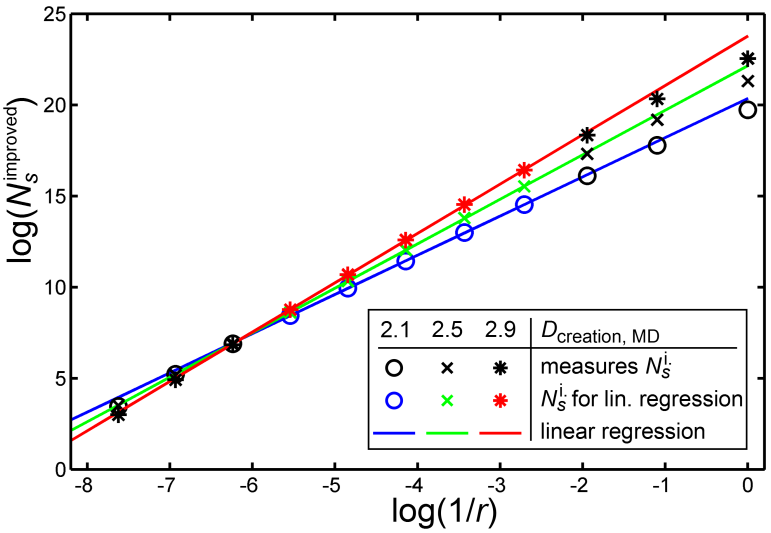

Figure A.2.: Exemplary log-log plot showing measures (N_s^{improved}, scaling variable r) obtained with the improved DBCM for three different images (theoretical D-values: 2.1 (circles), 2.5 (crosses), and 2.9 (stars), created with MD, 2048×2048 pixels). Coloured markers indicate optimized scale-ranges that were used for fitting linear regressions (solid lines).

A.2.2. Fourier Method

Table A.3.: RMSD and R^2 fit for each image size separately given for each generator (MD, FFT, Takagi). Power spectrum values of the lowest $n_{\Delta k}$ distance values in **k**-space were used for estimation of D.

		MD		FFT		Takagi	
image size	$n_{\Delta k}$	RMSD	R^2 fit	RMSD	R^2 fit	RSMD	R^2 fit
512×512	1000	0.12	0.54 ± 0.03	0.14	0.43 ± 0.03	1.26	0.30
1024×1024	1000	0.12	0.54 ± 0.03	0.14	0.43 ± 0.03	1.39	0.29
2048×2048	1000	0.12	0.54 ± 0.03	0.14	0.43 ± 0.03	1.56	0.28
4096×4096	1000	0.12	0.54 ± 0.03	0.14	0.43 ± 0.03	1.60	0.26

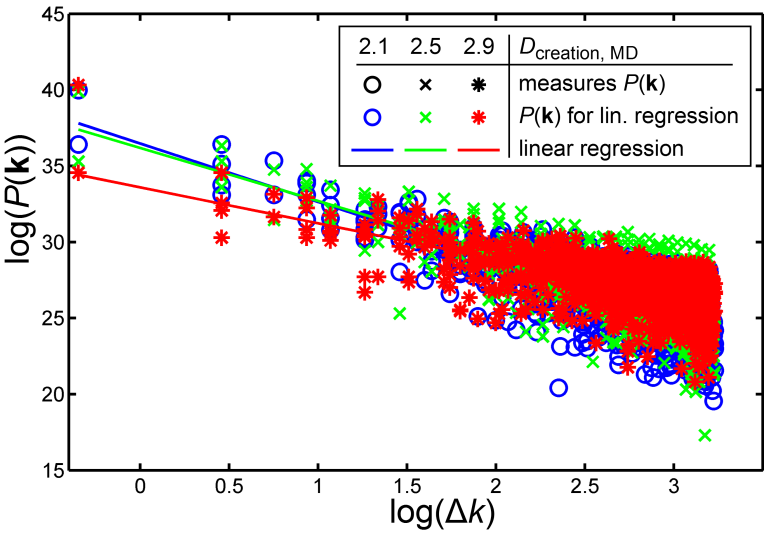

Figure A.3.: Exemplary log-log plot showing measures ($P(\mathbf{k})$, scaling variable Δk) obtained with the Fourier Method for three different images (theoretical D-values: 2.1 (circles), 2.5 (crosses), and 2.9 (stars), created with MD, 2048×2048 pixels). Coloured markers indicate optimized scale-ranges that were used for fitting linear regressions (solid lines).

A.2.3. 2D Higuchi Method

Table A.4.: RMSD and R^2 fit for the three best scale ranges k obtained with the 2D Higuchi Method for each image size separately given for each generator (MD, FFT, Takagi).

		MD		FFT		Takagi	
image size	k	RMSD	R^2 fit	RMSD	R^2 fit	RSMD	R^2 fit
512×512	$4-8$	0.06	0.99 ± 0.01	0.10	0.99 ± 0.01	0.04	0.99
	$3-8$	0.06	0.99 ± 0.01	0.10	0.99 ± 0.01	0.04	0.99
	$3-9$	0.06	0.99 ± 0.01	0.10	0.99 ± 0.01	0.04	0.99
1024×1024	$4-8$	0.05	0.99 ± 0.01	0.08	0.99 ± 0.01	0.03	0.99
	$5-10$	0.05	0.99 ± 0.01	0.09	0.99 ± 0.01	0.03	0.99
	$3-9$	0.06	0.99 ± 0.01	0.08	0.99 ± 0.01	0.03	0.99
2048×2048	$5-10$	0.05	0.99 ± 0.01	0.07	0.99 ± 0.01	0.03	0.99
	$5-12$	0.04	0.99 ± 0.01	0.07	0.99 ± 0.01	0.03	0.99
	$6-16$	0.04	0.99 ± 0.01	0.07	0.99 ± 0.01	0.03	0.99
4096×4096	$7-16$	0.04	0.99 ± 0.01	0.06	0.99 ± 0.01	0.02	0.99
	$7-17$	0.03	0.99 ± 0.01	0.06	0.99 ± 0.01	0.02	0.99
	$8-16$	0.03	0.99 ± 0.01	0.06	0.99 ± 0.01	0.03	0.99

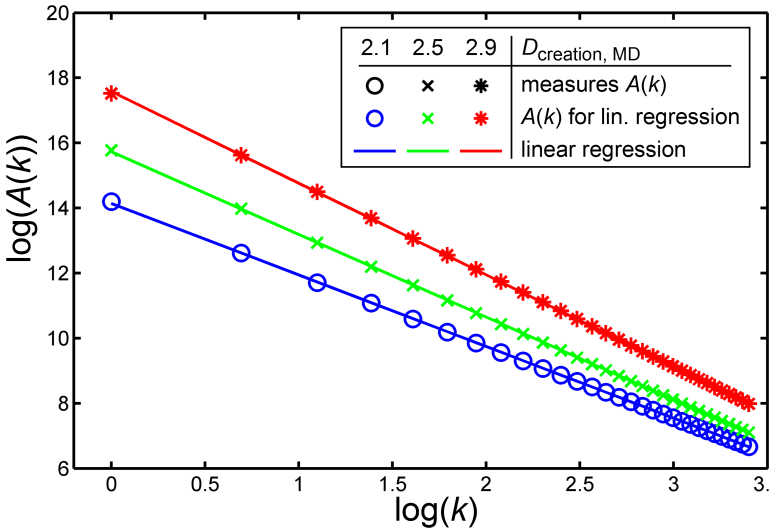

Figure A.4.: Exemplary log-log plot showing measures ($A(k)$, scaling variable k) obtained with the 2D Higuchi Method for three different images (theoretical D-values: 2.1 (circles), 2.5 (crosses), and 2.9 (stars), created with MD, 2048×2048 pixels). Coloured markers indicate optimized scale-ranges that were used for fitting linear regressions (solid lines).

A.2.4. Minkowski Blanket Method

Table A.5.: RMSD and R^2 fit for the three best numbers of blankets δ obtained with the Minkowski Blanket Method (Peleg) for each image size separately given for each generator (MD, FFT, Takagi).

		MD		FFT		Takagi	
image size	δ	RMSD	R^2 fit	RMSD	R^2 fit	RSMD	R^2 fit
512×512	$1-5$	0.04	0.99 ± 0.01	0.08	0.99 ± 0.01	0.03	0.99
	$1-6$	0.05	0.99 ± 0.01	0.08	0.99 ± 0.01	0.03	0.99
	$1-4$	0.04	0.99 ± 0.01	0.08	0.99 ± 0.01	0.04	0.99
1024×1024	$1-4$	0.08	0.99 ± 0.01	0.09	0.99 ± 0.01	0.03	0.99
	$1-5$	0.08	0.98 ± 0.01	0.08	0.99 ± 0.01	0.02	0.99
	$1-6$	0.09	0.98 ± 0.01	0.08	0.99 ± 0.01	0.02	0.99
2048×2048	$1-4$	0.12	0.98 ± 0.02	0.10	0.99 ± 0.01	0.06	0.99
	$1-5$	0.13	0.97 ± 0.02	0.10	0.99 ± 0.01	0.06	0.99
	$1-6$	0.14	0.97 ± 0.02	0.10	0.99 ± 0.01	0.07	0.99
4096×4096	$1-4$	0.16	0.95 ± 0.03	0.14	0.99 ± 0.01	0.12	0.99
	$1-5$	0.17	0.95 ± 0.03	0.14	0.99 ± 0.01	0.12	0.99
	$1-6$	0.18	0.94 ± 0.03	0.14	0.99 ± 0.01	0.13	0.99

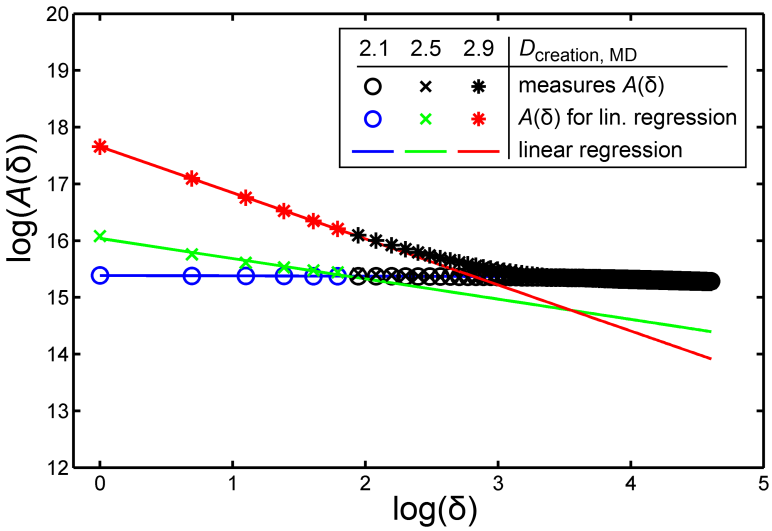

Figure A.5.: Exemplary log-log plot showing measures ($A(\delta)$, scaling variable δ) obtained with the Minkowski Blanket Method (Peleg) for three different images (theoretical D-values: 2.1 (circles), 2.5 (crosses), and 2.9 (stars), created with MD, 2048×2048 pixels). Coloured markers indicate optimized scale-ranges that were used for fitting linear regressions (solid lines).

Table A.6.: RMSD and R^2 fit for the three best numbers of blankets n obtained with the Minkowski Blanket Method (Dubuc) for each image size separately given for each generator (MD, FFT, Takagi).

		MD		FFT		Takagi	
image size	n	RMSD	R^2 fit	RMSD	R^2 fit	RSMD	R^2 fit
512×512	$1-100$	0.17	0.99 ± 0.01	0.17	0.99 ± 0.01	0.14	0.99
	$1-99$	0.17	0.99 ± 0.01	0.17	0.99 ± 0.01	0.14	0.99
	$1-98$	0.18	0.99 ± 0.01	0.17	0.99 ± 0.01	0.14	0.99
1024×1024	$1-100$	0.16	0.99 ± 0.01	0.15	0.99 ± 0.01	0.13	0.99
	$1-99$	0.16	0.99 ± 0.01	0.15	0.99 ± 0.01	0.13	0.99
	$1-98$	0.16	0.99 ± 0.01	0.15	0.99 ± 0.01	0.13	0.99
2048×2048	$1-100$	0.15	0.99 ± 0.01	0.15	0.99 ± 0.01	0.12	0.99
	$1-99$	0.15	0.99 ± 0.01	0.15	0.99 ± 0.01	0.12	0.99
	$1-98$	0.15	0.99 ± 0.01	0.15	0.99 ± 0.01	0.12	0.99
4096×4096	$1-100$	0.14	0.99 ± 0.01	0.15	0.99 ± 0.01	0.12	0.99
	$1-99$	0.14	0.99 ± 0.01	0.15	0.99 ± 0.01	0.12	0.99
	$1-98$	0.14	0.99 ± 0.01	0.15	0.99 ± 0.01	0.12	0.99

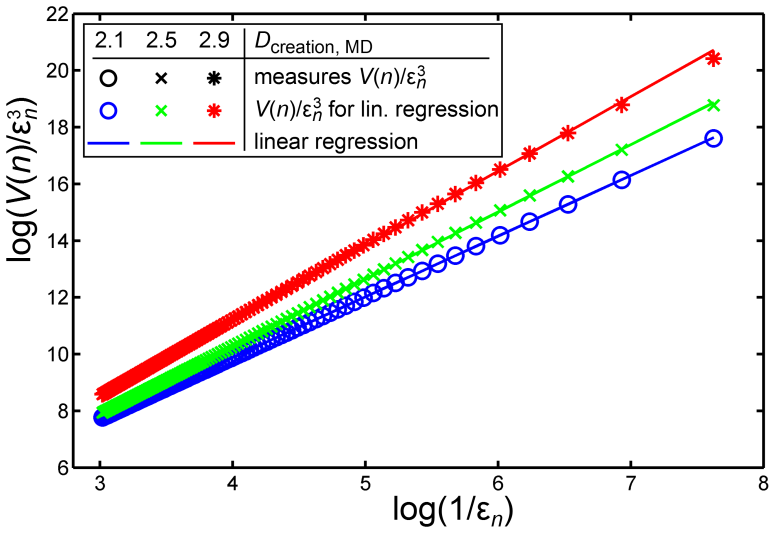

Figure A.6.: Exemplary log-log plot showing measures ($V(n)$, scaling variable ϵ_n) obtained with the Minkowski Blanket Method (Dubuc) for three different images (theoretical D-values: 2.1 (circles), 2.5 (crosses), and 2.9 (stars), created with MD, 2048×2048 pixels). Coloured markers indicate optimized scale-ranges that were used for fitting linear regressions (solid lines).

A.2.5. Triangular Prism Method

Table A.7.: RMSD and R^2 fit for the three best scale ranges obtained with the TPM for each image size separately given for each generator (MD, FFT, Takagi). The scale values are given as exponents of 2, i.e. scales$= 0-5 \rightarrow s = 2^0 - 2^5$.

		MD		FFT		Takagi	
image size	scales	RMSD	R^2 fit	RMSD	R^2 fit	RSMD	R^2 fit
512×512	$0-5$	0.07	0.99 ± 0.01	0.11	0.99 ± 0.01	0.10	0.99
	$0-4$	0.05	0.99 ± 0.01	0.10	0.99 ± 0.01	0.12	0.99
	$0-6$	0.08	0.99 ± 0.01	0.12	0.99 ± 0.01	0.09	0.98
1024×1024	$0-3$	0.08	0.99 ± 0.01	0.10	0.99 ± 0.01	0.15	0.98
	$0-4$	0.10	0.99 ± 0.01	0.10	0.99 ± 0.01	0.15	0.99
	$0-5$	0.13	0.99 ± 0.01	0.10	0.99 ± 0.01	0.14	0.99
2048×2048	$0-3$	0.12	0.98 ± 0.01	0.12	0.99 ± 0.01	0.17	0.97
	$0-4$	0.14	0.97 ± 0.01	0.13	0.99 ± 0.01	0.17	0.98
	$0-5$	0.18	0.97 ± 0.01	0.14	0.99 ± 0.01	0.18	0.99
4096×4096	$0-3$	0.16	0.97 ± 0.01	0.16	0.99 ± 0.01	0.19	0.96
	$0-4$	0.19	0.95 ± 0.01	0.17	0.99 ± 0.01	0.20	0.96
	$0-5$	0.22	0.94 ± 0.01	0.19	0.99 ± 0.01	0.21	0.97

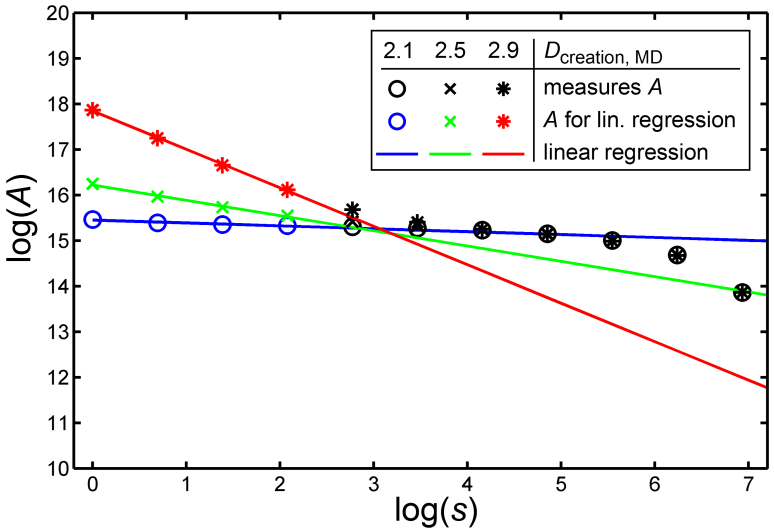

Figure A.7.: Exemplary log-log plot showing measures (A, scaling variable s) obtained with the TPM for three different images (theoretical D-values: 2.1 (circles), 2.5 (crosses), and 2.9 (stars), created with MD, 2048×2048 pixels). Coloured markers indicate optimized scale-ranges that were used for fitting linear regressions (solid lines).

A.2.6. Pyramid Triangular Prism Method

Table A.8.: RMSD and R^2 fit for the three best scale-down factor ranges obtained with the PTPM (bicubic interpolation) for each image size separately given for each generator (MD, FFT, Takagi). The scale-down factor ranges (scales) are given as exponents of 2, i.e. scales$= 0-5 \rightarrow s_n = 2^0 - 2^5$.

		MD		FFT		Takagi	
image size	scales	RMSD	R^2 fit	RMSD	R^2 fit	RSMD	R^2 fit
512×512	$0-4$	0.02	0.95 ± 0.01	0.11	0.99 ± 0.01	0.05	0.99
	$0-5$	0.05	0.95 ± 0.01	0.12	0.99 ± 0.01	0.04	0.99
	$1-4$	0.09	0.99 ± 0.01	0.11	0.99 ± 0.01	0.04	0.99
1024×1024	$0-4$	0.07	0.91 ± 0.02	0.04	0.99 ± 0.01	0.03	0.98
	$0-3$	0.07	0.92 ± 0.02	0.05	0.99 ± 0.01	0.08	0.98
	$0-5$	0.12	0.91 ± 0.02	0.07	0.99 ± 0.01	0.05	0.97
2048×2048	$0-3$	0.09	0.89 ± 0.02	0.03	0.99 ± 0.01	0.08	0.96
	$0-4$	0.12	0.87 ± 0.02	0.06	0.99 ± 0.01	0.07	0.96
	$0-5$	0.18	0.86 ± 0.02	0.11	0.98 ± 0.01	0.11	0.95
4096×4096	$0-3$	0.13	0.87 ± 0.02	0.08	0.97 ± 0.01	0.1	0.93
	$0-4$	0.17	0.84 ± 0.02	0.12	0.96 ± 0.01	0.12	0.91
	$0-5$	0.23	0.81 ± 0.02	0.17	0.95 ± 0.01	0.17	0.9

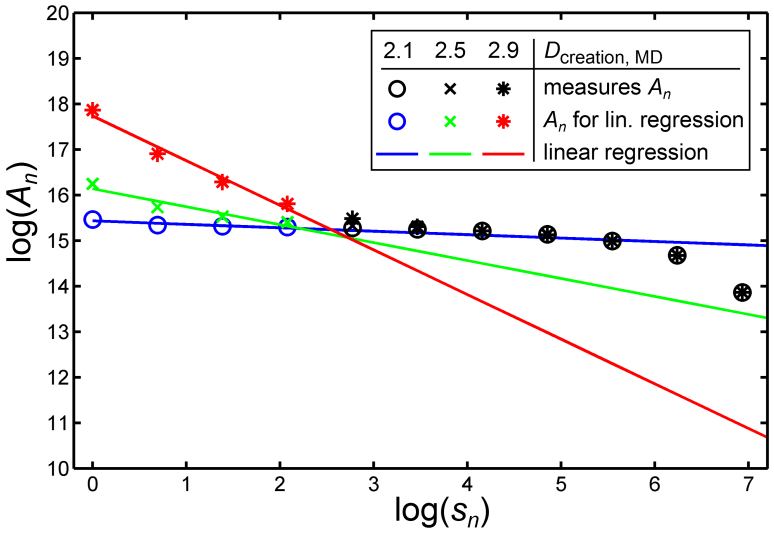

Figure A.8.: Exemplary log-log plot showing measures (A_n, scaling variable s_n) obtained with the PTPM (bicubic interpolation) for three different images (theoretical D-values: 2.1 (circles), 2.5 (crosses), and 2.9 (stars), created with MD, 2048×2048 pixels). Coloured markers indicate optimized scale-ranges that were used for fitting linear regressions (solid lines).

Table A.9.: RMSD and R^2 fit for the three best scale-down factor ranges obtained with the PTPM (bilinear interpolation) for each image size separately given for each generator (MD, FFT, Takagi). The scale-down factor ranges (scales) are given as exponents of 2, i.e. scales$= 0-5 \rightarrow s_n = 2^0 - 2^5$.

		MD		FFT		Takagi	
image size	scales	RMSD	R^2 fit	RMSD	R^2 fit	RSMD	R^2 fit
512×512	$0-5$	0.05	0.92 ± 0.02	0.13	0.99 ± 0.01	0.04	0.98
	$0-4$	0.04	0.92 ± 0.02	0.15	0.99 ± 0.01	0.08	0.98
	$1-4$	0.12	0.99 ± 0.01	0.12	0.99 ± 0.01	0.05	0.99
1024×1024	$0-4$	0.07	0.88 ± 0.02	0.06	0.98 ± 0.01	0.04	0.96
	$0-5$	0.12	0.87 ± 0.02	0.07	0.97 ± 0.01	0.05	0.96
	$0-3$	0.11	0.90 ± 0.02	0.11	0.98 ± 0.01	0.11	0.97
2048×2048	$0-4$	0.12	0.83 ± 0.02	0.04	0.96 ± 0.01	0.07	0.93
	$0-3$	0.11	0.86 ± 0.02	0.05	0.97 ± 0.01	0.10	0.94
	$0-5$	0.18	0.81 ± 0.02	0.11	0.95 ± 0.01	0.11	0.92
4096×4096	$0-3$	0.13	0.84 ± 0.02	0.06	0.94 ± 0.01	0.11	0.91
	$0-4$	0.17	0.79 ± 0.02	0.11	0.93 ± 0.01	0.12	0.89
	$0-5$	0.23	0.76 ± 0.02	0.17	0.91 ± 0.01	0.17	0.87

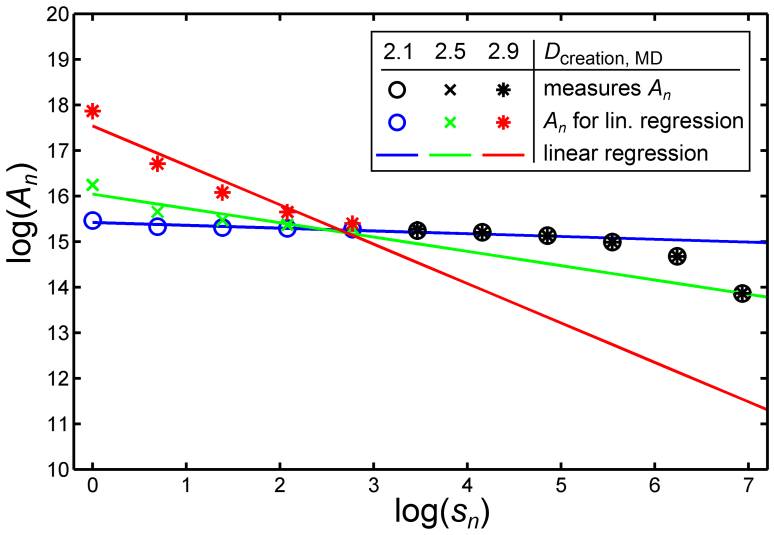

Figure A.9.: Exemplary log-log plot showing measures (A_n, scaling variable s_n) obtained with the PTPM (bilinear interpolation) for three different images (theoretical D-values: 2.1 (circles), 2.5 (crosses), and 2.9 (stars), created with MD, 2048×2048 pixels). Coloured markers indicate optimized scale-ranges that were used for fitting linear regressions (solid lines).

Table A.10.: RMSD and R^2 fit for the three best scale-down factor ranges obtained with the PTPM (nearest neighbour interpolation) for each image size separately given for each generator (MD, FFT, Takagi). The scale-down factor ranges (scales) are given as exponents of 2, i.e. scales$= 0-5 \rightarrow s_n = 2^0 - 2^5$.

		MD		FFT		Takagi	
image size	scales	RMSD	R^2 fit	RMSD	R^2 fit	RSMD	R^2 fit
512×512	$0-5$	0.07	0.98 ± 0.01	0.10	0.99 ± 0.01	0.10	0.99
	$0-4$	0.05	0.98 ± 0.01	0.10	0.99 ± 0.01	0.12	0.99
	$0-3$	0.04	0.98 ± 0.01	0.10	0.99 ± 0.01	0.14	0.99
1024×1024	$0-3$	0.08	0.97 ± 0.01	0.10	0.99 ± 0.01	0.15	0.98
	$0-4$	0.10	0.96 ± 0.01	0.10	0.99 ± 0.01	0.15	0.99
	$0-5$	0.13	0.96 ± 0.01	0.10	0.99 ± 0.01	0.14	0.99
2048×2048	$0-3$	0.12	0.95 ± 0.01	0.13	0.99 ± 0.01	0.17	0.97
	$0-4$	0.15	0.94 ± 0.01	0.13	0.99 ± 0.01	0.17	0.98
	$0-5$	0.18	0.93 ± 0.01	0.14	0.99 ± 0.01	0.18	0.99
4096×4096	$0-3$	0.16	0.95 ± 0.01	0.16	0.99 ± 0.01	0.19	0.96
	$0-4$	0.19	0.92 ± 0.01	0.17	0.99 ± 0.01	0.2	0.96
	$0-5$	0.22	0.91 ± 0.02	0.19	0.99 ± 0.01	0.21	0.97

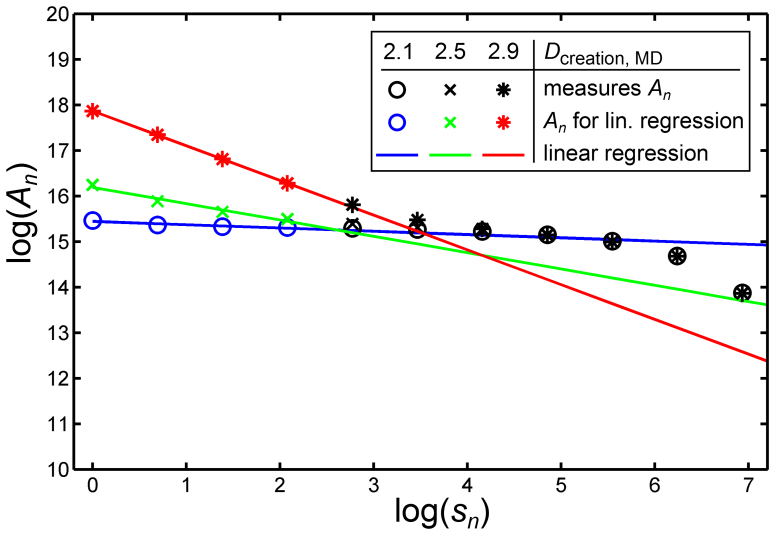

Figure A.10.: Exemplary log-log plot showing measures (A_n, scaling variable s_n) obtained with the PTPM (nearest neighbour interpolation) for three different images (theoretical D-values: 2.1 (circles), 2.5 (crosses), and 2.9 (stars), created with MD, 2048×2048 pixels). Coloured markers indicate optimized scale-ranges that were used for fitting linear regressions (solid lines).

A.2.7. Pyramid Gradient Method

Table A.11.: RMSD and R^2 fit for the three best scale-down factor ranges obtained with the PGM (simple kernel, bicubic interpolation) for each image size separately given for each generator (MD, FFT, Takagi). The scale-down factor ranges (scales) are given as exponents of 2, i.e. scales$= 0-5 \rightarrow s_n = 2^0 - 2^5$.

		MD		FFT		Takagi	
image size	scales	RMSD	R^2 fit	RMSD	R^2 fit	RSMD	R^2 fit
512×512	$0-3$	0.07	0.99 ± 0.01	0.07	0.99 ± 0.01	0.05	0.99
	$0-4$	0.13	0.99 ± 0.01	0.09	0.99 ± 0.01	0.09	0.99
	$0-5$	0.18	0.99 ± 0.01	0.12	0.99 ± 0.01	0.13	0.99
1024×1024	$0-3$	0.11	0.99 ± 0.01	0.04	0.99 ± 0.01	0.07	0.99
	$0-4$	0.16	0.99 ± 0.01	0.08	0.99 ± 0.01	0.11	0.99
	$0-5$	0.21	0.99 ± 0.01	0.13	0.99 ± 0.01	0.15	0.99
2048×2048	$0-3$	0.15	0.99 ± 0.01	0.08	0.99 ± 0.01	0.11	0.99
	$0-4$	0.2	0.99 ± 0.01	0.12	0.99 ± 0.01	0.15	0.99
	$0-5$	0.25	0.99 ± 0.01	0.17	0.99 ± 0.01	0.19	0.99
4096×4096	$0-3$	0.19	0.99 ± 0.01	0.13	0.99 ± 0.01	0.16	0.99
	$0-4$	0.24	0.99 ± 0.01	0.17	0.99 ± 0.01	0.2	0.99
	$0-5$	0.29	0.99 ± 0.01	0.22	0.99 ± 0.01	0.24	0.99

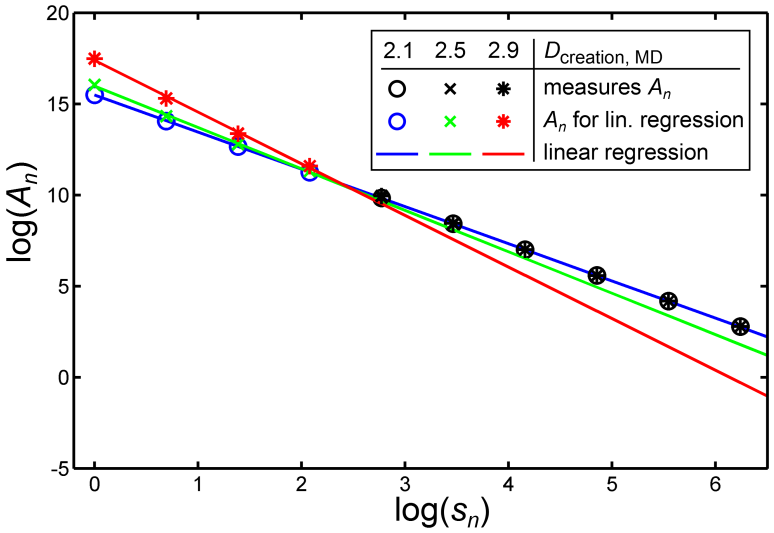

Figure A.11.: Exemplary log-log plot showing measures (A_n, scaling variable s_n) obtained with the PGM (simple, bicubic interpolation) for three different images (theoretical D-values: 2.1 (circles), 2.5 (crosses), and 2.9 (stars), created with MD, 2048×2048 pixels). Coloured markers indicate optimized scale-ranges that were used for fitting linear regressions (solid lines).

Table A.12.: RMSD and R^2 fit for the three best scale-down factor ranges obtained with the PGM (simple kernel, bilinear interpolation) for each image size separately given for each generator (MD, FFT, Takagi). The scale-down factor ranges (scales) are given as exponents of 2, i.e. scales$= 0-5 \rightarrow s_n = 2^0 - 2^5$.

		MD		FFT		Takagi	
image size	scales	RMSD	R^2 fit	RMSD	R^2 fit	RSMD	R^2 fit
512×512	$0-3$	0.05	0.99 ± 0.01	0.09	0.99 ± 0.01	0.03	0.99
	$0-4$	0.12	0.99 ± 0.01	0.09	0.99 ± 0.01	0.07	0.99
	$0-5$	0.18	0.99 ± 0.01	0.13	0.99 ± 0.01	0.13	0.99
1024×1024	$0-3$	0.10	0.99 ± 0.01	0.03	0.99 ± 0.01	0.04	0.99
	$0-4$	0.16	0.99 ± 0.01	0.07	0.99 ± 0.01	0.10	0.99
	$0-5$	0.22	0.99 ± 0.01	0.13	0.99 ± 0.01	0.15	0.99
2048×2048	$0-3$	0.14	0.99 ± 0.01	0.05	0.99 ± 0.01	0.09	0.99
	$0-4$	0.20	0.99 ± 0.01	0.11	0.99 ± 0.01	0.14	0.99
	$0-5$	0.26	0.99 ± 0.01	0.17	0.99 ± 0.01	0.19	0.99
4096×4096	$0-3$	0.18	0.99 ± 0.01	0.11	0.99 ± 0.01	0.14	0.99
	$0-4$	0.24	0.99 ± 0.01	0.17	0.99 ± 0.01	0.19	0.99
	$0-5$	0.30	0.99 ± 0.01	0.22	0.99 ± 0.01	0.24	0.99

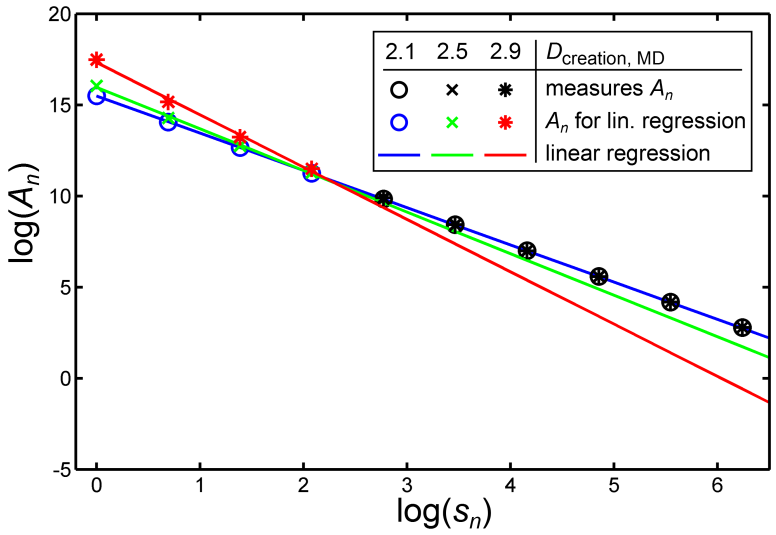

Figure A.12.: Exemplary log-log plot showing measures (A_n, scaling variable s_n) obtained with the PGM (simple, bilinear interpolation) for three different images (theoretical D-values: 2.1 (circles), 2.5 (crosses), and 2.9 (stars), created with MD, 2048×2048 pixels). Coloured markers indicate optimized scale-ranges that were used for fitting linear regressions (solid lines).

Table A.13.: RMSD and R^2 fit for the three best scale-down factor ranges obtained with the PGM (simple kernel, nearest neighbour interpolation) for each image size separately given for each generator (MD, FFT, Takagi). The scale-down factor ranges (scales) are given as exponents of 2, i.e. scales$= 0-5 \rightarrow s_n = 2^0 - 2^5$.

		MD		FFT		Takagi	
image size	scales	RMSD	R^2 fit	RMSD	R^2 fit	RSMD	R^2 fit
512×512	$0-3$	0.12	0.99 ± 0.01	0.10	0.99 ± 0.01	0.08	0.99
	$0-4$	0.15	0.99 ± 0.01	0.11	0.99 ± 0.01	0.10	0.99
	$1-4$	0.18	0.99 ± 0.01	0.12	0.99 ± 0.01	0.12	0.99
1024×1024	$0-3$	0.14	0.99 ± 0.01	0.10	0.99 ± 0.01	0.10	0.99
	$0-4$	0.18	0.99 ± 0.01	0.12	0.99 ± 0.01	0.13	0.99
	$1-4$	0.22	0.99 ± 0.01	0.13	0.99 ± 0.01	0.15	0.99
2048×2048	$0-3$	0.18	0.99 ± 0.01	0.13	0.99 ± 0.01	0.13	0.99
	$0-4$	0.21	0.99 ± 0.01	0.15	0.99 ± 0.01	0.16	0.99
	$1-4$	0.25	0.99 ± 0.01	0.16	0.99 ± 0.01	0.20	0.99
4096×4096	$0-3$	0.21	0.99 ± 0.01	0.17	0.99 ± 0.01	0.18	0.99
	$0-4$	0.25	0.99 ± 0.01	0.19	0.99 ± 0.01	0.21	0.99
	$1-4$	0.29	0.99 ± 0.01	0.21	0.99 ± 0.01	0.25	0.99

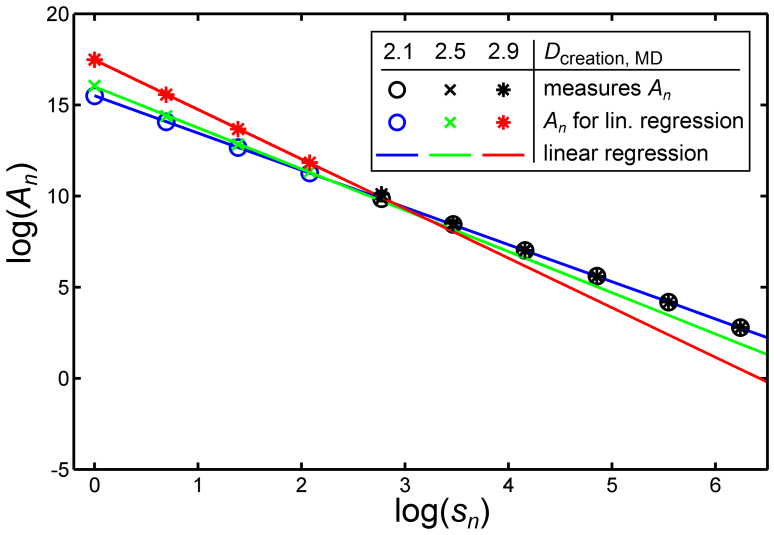

Figure A.13.: Exemplary log-log plot showing measures (A_n, scaling variable s_n) obtained with the PGM (simple kernel, nearest neighbour interpolation) for three different images (theoretical D-values: 2.1 (circles), 2.5 (crosses), and 2.9 (stars), created with MD, 2048×2048 pixels). Coloured markers indicate optimized scale-ranges that were used for fitting linear regressions (solid lines).

Table A.14.: RMSD and R^2 fit for the three best scale-down factor ranges obtained with the PGM (Sobel kernel, bicubic interpolation) for each image size separately given for each generator (MD, FFT, Takagi). The scale-down factor ranges (scales) are given as exponents of 2, i.e. scales$= 0-5 \rightarrow s_n = 2^0 - 2^5$.

		MD		FFT		Takagi	
image size	scales	RMSD	R^2 fit	RMSD	R^2 fit	RSMD	R^2 fit
512×512	$0-3$	0.12	0.99 ± 0.01	0.08	0.99 ± 0.01	0.06	0.99
	$0-4$	0.17	0.99 ± 0.01	0.11	0.99 ± 0.01	0.09	0.99
	$0-5$	0.21	0.99 ± 0.01	0.15	0.99 ± 0.01	0.14	0.99
1024×1024	$0-3$	0.16	0.99 ± 0.01	0.07	0.99 ± 0.01	0.08	0.99
	$0-4$	0.21	0.99 ± 0.01	0.11	0.99 ± 0.01	0.12	0.99
	$0-5$	0.25	0.99 ± 0.01	0.16	0.99 ± 0.01	0.16	0.99
2048×2048	$0-3$	0.20	0.99 ± 0.01	0.10	0.99 ± 0.01	0.12	0.99
	$0-4$	0.25	0.99 ± 0.01	0.15	0.99 ± 0.01	0.16	0.99
	$0-5$	0.29	0.99 ± 0.01	0.20	0.99 ± 0.01	0.20	0.99
4096×4096	$0-3$	0.24	0.99 ± 0.01	0.15	0.99 ± 0.01	0.17	0.99
	$0-4$	0.28	0.99 ± 0.01	0.20	0.99 ± 0.01	0.21	0.99
	$0-5$	0.33	0.99 ± 0.01	0.25	0.99 ± 0.01	0.25	0.99

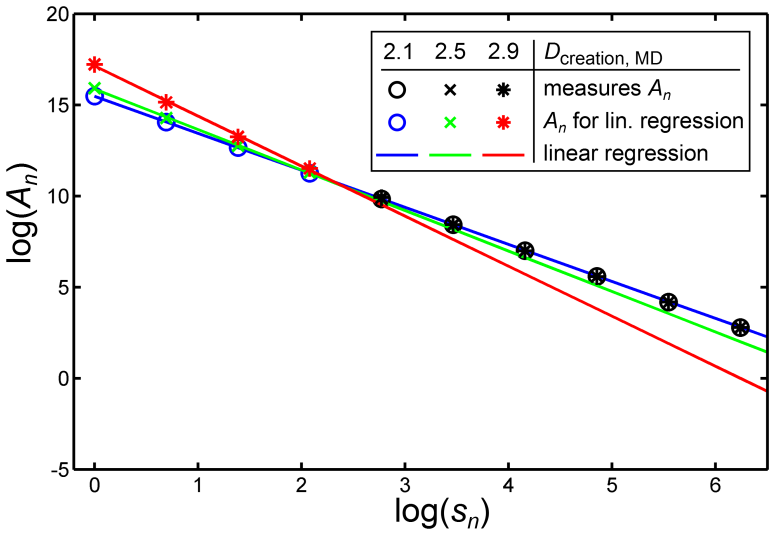

Figure A.14.: Exemplary log-log plot showing measures (A_n, scaling variable s_n) obtained with the PGM (sobel, bicubic interpolation) for three different images (theoretical D-values: 2.1 (circles), 2.5 (crosses), and 2.9 (stars), created with MD, 2048×2048 pixels). Coloured markers indicate optimized scale-ranges that were used for fitting linear regressions (solid lines).

Table A.15.: RMSD and R^2 fit for the three best scale-down factor ranges obtained with the PGM (Sobel kernel, bilinear interpolation) for each image size separately given for each generator (MD, FFT, Takagi). The scale-down factor ranges (scales) are given as exponents of 2, i.e. scales$= 0-5 \rightarrow s_n = 2^0 - 2^5$.

		MD		FFT		Takagi	
image size	scales	RMSD	R^2 fit	RMSD	R^2 fit	RSMD	R^2 fit
512×512	$0-3$	0.11	0.99 ± 0.01	0.08	0.99 ± 0.01	0.04	0.99
	$0-4$	0.17	0.99 ± 0.01	0.11	0.99 ± 0.01	0.08	0.99
	$0-5$	0.22	0.99 ± 0.01	0.15	0.99 ± 0.01	0.14	0.99
1024×1024	$0-3$	0.15	0.99 ± 0.01	0.05	0.99 ± 0.01	0.05	0.99
	$0-4$	0.20	0.99 ± 0.01	0.10	0.99 ± 0.01	0.11	0.99
	$0-5$	0.25	0.99 ± 0.01	0.16	0.99 ± 0.01	0.16	0.99
2048×2048	$0-3$	0.19	0.99 ± 0.01	0.08	0.99 ± 0.01	0.10	0.99
	$0-4$	0.24	0.99 ± 0.01	0.14	0.99 ± 0.01	0.15	0.99
	$0-5$	0.29	0.99 ± 0.01	0.20	0.99 ± 0.01	0.20	0.99
4096×4096	$0-3$	0.23	0.99 ± 0.01	0.14	0.99 ± 0.01	0.15	0.99
	$0-4$	0.28	0.99 ± 0.01	0.20	0.99 ± 0.01	0.20	0.99
	$0-5$	0.33	0.99 ± 0.01	0.25	0.99 ± 0.01	0.25	0.99

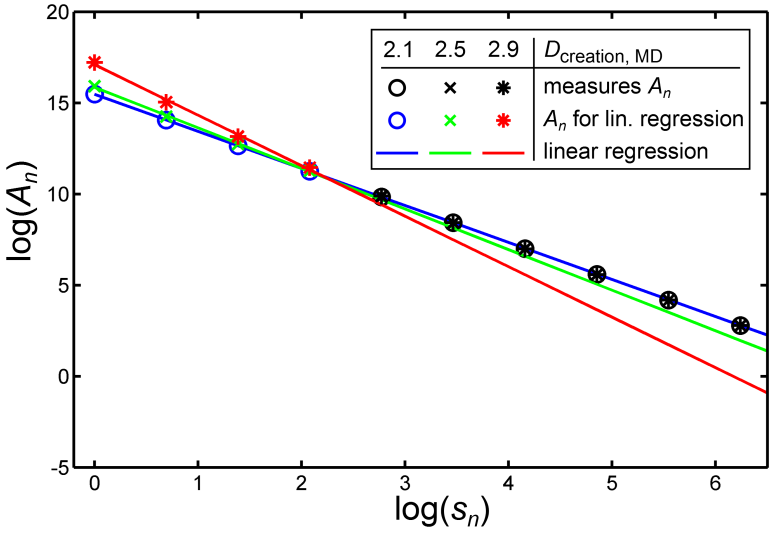

Figure A.15.: Exemplary log-log plot showing measures (A_n, scaling variable s_n) obtained with the PGM (sobel, bilinear interpolation) for three different images (theoretical D-values: 2.1 (circles), 2.5 (crosses), and 2.9 (stars), created with MD, 2048×2048 pixels). Coloured markers indicate optimized scale-ranges that were used for fitting linear regressions (solid lines).

Table A.16.: RMSD and R^2 fit for the three best scale-down factor ranges obtained with the PGM (Sobel kernel, nearest neighbour interpolation) for each image size separately given for each generator (MD, FFT, Takagi). The scale-down factor ranges (scales) are given as exponents of 2, i.e. scales$= 0-5 \rightarrow s_n = 2^0 - 2^5$.

		MD		FFT		Takagi	
image size	scales	RMSD	R^2 fit	RMSD	R^2 fit	RSMD	R^2 fit
512×512	$0-3$	0.15	0.99 ± 0.01	0.10	0.99 ± 0.01	0.08	0.99
	$0-4$	0.18	0.99 ± 0.01	0.12	0.99 ± 0.01	0.10	0.99
	$1-4$	0.22	0.99 ± 0.01	0.14	0.99 ± 0.01	0.12	0.99
1024×1024	$0-3$	0.18	0.99 ± 0.01	0.10	0.99 ± 0.01	0.10	0.99
	$0-4$	0.21	0.99 ± 0.01	0.13	0.99 ± 0.01	0.13	0.99
	$1-4$	0.26	0.99 ± 0.01	0.15	0.99 ± 0.01	0.16	0.99
2048×2048	$0-3$	0.21	0.99 ± 0.01	0.13	0.99 ± 0.01	0.14	0.99
	$0-4$	0.25	0.99 ± 0.01	0.16	0.99 ± 0.01	0.17	0.99
	$1-4$	0.29	0.99 ± 0.01	0.19	0.99 ± 0.01	0.20	0.99
4096×4096	$0-3$	0.25	0.99 ± 0.01	0.17	0.99 ± 0.01	0.18	0.99
	$0-4$	0.29	0.99 ± 0.01	0.21	0.99 ± 0.01	0.22	0.99
	$1-4$	0.33	0.99 ± 0.01	0.24	0.99 ± 0.01	0.25	0.99

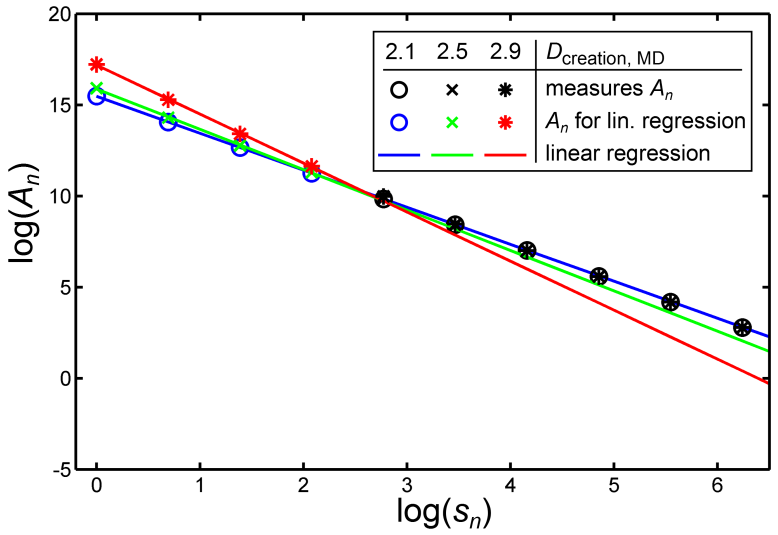

Figure A.16.: Exemplary log-log plot showing measures (A_n, scaling variable s_n) obtained with the PGM (sobel kernel, nearest neighbour interpolation) for three different images (theoretical D-values: 2.1 (circles), 2.5 (crosses), and 2.9 (stars), created with MD, 2048×2048 pixels). Coloured markers indicate optimized scale-ranges that were used for fitting linear regressions (solid lines).

A.2.8. Pyramid Differences Method

Table A.17.: RMSD and R^2 fit for the three best scale-down factor ranges obtained with the PDM (bicubic interpolation) for each image size separately given for each generator (MD, FFT, Takagi). The scale-down factor ranges (scales) are given as exponents of 2, i.e. scales$= 0-5 \rightarrow s_n = 2^0 - 2^5$.

		MD		FFT		Takagi	
image size	scales	RMSD	R^2 fit	RMSD	R^2 fit	RSMD	R^2 fit
512×512	$1-4$	0.08	0.99 ± 0.01	0.19	0.99 ± 0.01	0.07	0.99
	$1-5$	0.09	0.99 ± 0.01	0.24	0.99 ± 0.01	0.09	0.99
	$0-4$	0.17	0.99 ± 0.01	0.18	0.99 ± 0.01	0.13	0.99
1024×1024	$1-4$	0.06	0.99 ± 0.01	0.12	0.99 ± 0.01	0.05	0.99
	$1-5$	0.06	0.99 ± 0.01	0.15	0.99 ± 0.01	0.06	0.99
	$2-5$	0.05	0.99 ± 0.01	0.18	0.99 ± 0.01	0.06	0.99
2048×2048	$1-4$	0.05	0.99 ± 0.01	0.08	0.99 ± 0.01	0.05	0.99
	$1-5$	0.05	0.99 ± 0.01	0.1	0.99 ± 0.01	0.05	0.99
	$2-5$	0.04	0.99 ± 0.01	0.12	0.99 ± 0.01	0.04	0.99
4096×4096	$2-5$	0.03	0.99 ± 0.01	0.08	0.99 ± 0.01	0.03	0.99
	$1-4$	0.05	0.99 ± 0.01	0.06	0.99 ± 0.01	0.04	0.99
	$1-5$	0.05	0.99 ± 0.01	0.07	0.99 ± 0.01	0.04	0.99

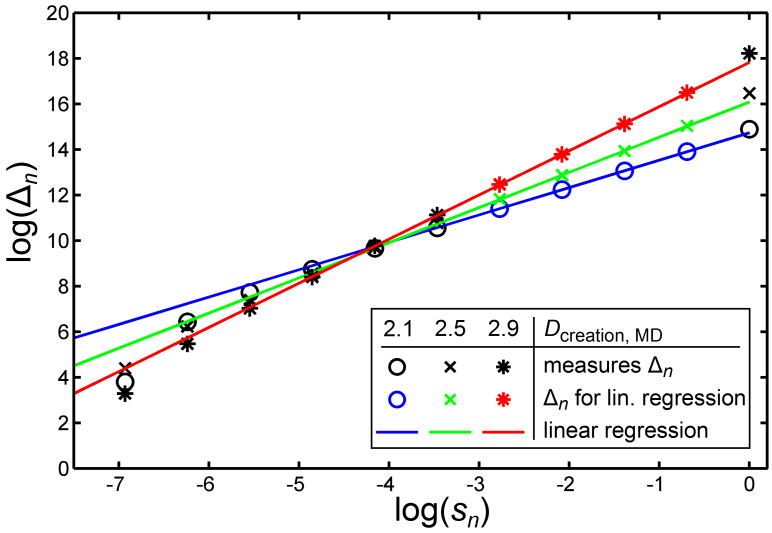

Figure A.17.: Exemplary log-log plot showing measures (Δ_n, scaling variable s_n) obtained with the PDM (bicubic interpolation) for three different images (theoretical D-values: 2.1 (circles), 2.5 (crosses), and 2.9 (stars), created with MD, 2048×2048 pixels). Coloured markers indicate optimized scale-ranges that were used for fitting linear regressions (solid lines).

Table A.18.: RMSD and R^2 fit for the three best scale-down factor ranges obtained with the PDM (bilinear interpolation) for each image size separately given for each generator (MD, FFT, Takagi). The scale-down factor ranges (scales) are given as exponents of 2, i.e. scales$= 0-5 \rightarrow s_n = 2^0 - 2^5$.

		MD		FFT		Takagi	
image size	scales	RMSD	R^2 fit	RMSD	R^2 fit	RSMD	R^2 fit
512×512	$1-4$	0.09	0.99 ± 0.01	0.24	0.99 ± 0.01	0.08	0.99
	$1-5$	0.10	0.99 ± 0.01	0.29	0.99 ± 0.01	0.10	0.99
	$2-5$	0.10	0.99 ± 0.01	0.33	0.99 ± 0.01	0.11	0.99
1024×1024	$1-4$	0.07	0.99 ± 0.01	0.16	0.99 ± 0.01	0.06	0.99
	$1-5$	0.07	0.99 ± 0.01	0.19	0.99 ± 0.01	0.07	0.99
	$2-5$	0.06	0.99 ± 0.01	0.22	0.99 ± 0.01	0.07	0.99
2048×2048	$1-4$	0.07	0.99 ± 0.01	0.11	0.99 ± 0.01	0.05	0.99
	$1-5$	0.06	0.99 ± 0.01	0.13	0.99 ± 0.01	0.05	0.99
	$2-5$	0.04	0.99 ± 0.01	0.14	0.99 ± 0.01	0.05	0.99
4096×4096	$2-5$	0.03	0.99 ± 0.01	0.10	0.99 ± 0.01	0.03	0.99
	$1-4$	0.06	0.99 ± 0.01	0.08	0.99 ± 0.01	0.05	0.99
	$1-5$	0.05	0.99 ± 0.01	0.09	0.99 ± 0.01	0.04	0.99

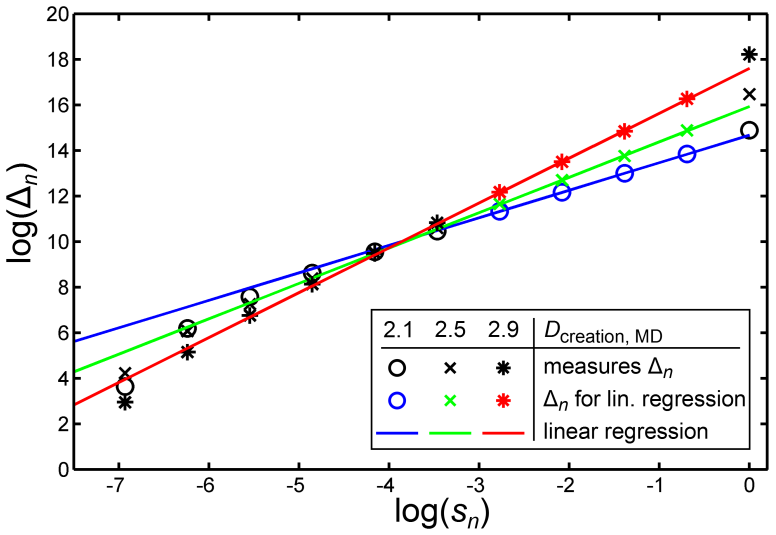

Figure A.18.: Exemplary log-log plot showing measures (Δ_n, scaling variable s_n) obtained with the PDM (bilinear interpolation) for three different images (theoretical D-values: 2.1 (circles), 2.5 (crosses), and 2.9 (stars), created with MD, 2048×2048 pixels). Coloured markers indicate optimized scale-ranges that were used for fitting linear regressions (solid lines).

Table A.19.: RMSD and R^2 fit for the three best scale-down factor ranges obtained with the PDM (nearest neighbour interpolation) for each image size separately given for each generator (MD, FFT, Takagi). The scale-down factor ranges (scales) are given as exponents of 2, i.e. scales$= 0-5 \rightarrow s_n = 2^0 - 2^5$.

		MD		FFT		Takagi	
image size	scales	RMSD	R^2 fit	RMSD	R^2 fit	RSMD	R^2 fit
512×512	$0-5$	0.05	0.99 ± 0.01	0.13	0.99 ± 0.01	0.10	0.99
	$0-4$	0.06	0.99 ± 0.01	0.10	0.99 ± 0.01	0.13	0.99
	$1-5$	0.03	0.99 ± 0.01	0.16	0.99 ± 0.01	0.09	0.99
1024×1024	$2-5$	0.02	0.99 ± 0.01	0.12	0.99 ± 0.01	0.07	0.99
	$0-6$	0.04	0.99 ± 0.01	0.11	0.99 ± 0.01	0.08	0.99
	$0-5$	0.04	0.99 ± 0.01	0.09	0.99 ± 0.01	0.12	0.99
2048×2048	$2-6$	0.02	0.99 ± 0.01	0.11	0.99 ± 0.01	0.05	0.99
	$2-5$	0.02	0.99 ± 0.01	0.09	0.99 ± 0.01	0.08	0.99
	$0-7$	0.03	0.99 ± 0.01	0.10	0.99 ± 0.01	0.07	0.99
4096×4096	$3-6$	0.02	0.99 ± 0.01	0.09	0.99 ± 0.01	0.04	0.99
	$2-6$	0.02	0.99 ± 0.01	0.07	0.99 ± 0.01	0.07	0.99
	$2-7$	0.02	0.99 ± 0.01	0.09	0.99 ± 0.01	0.04	0.99

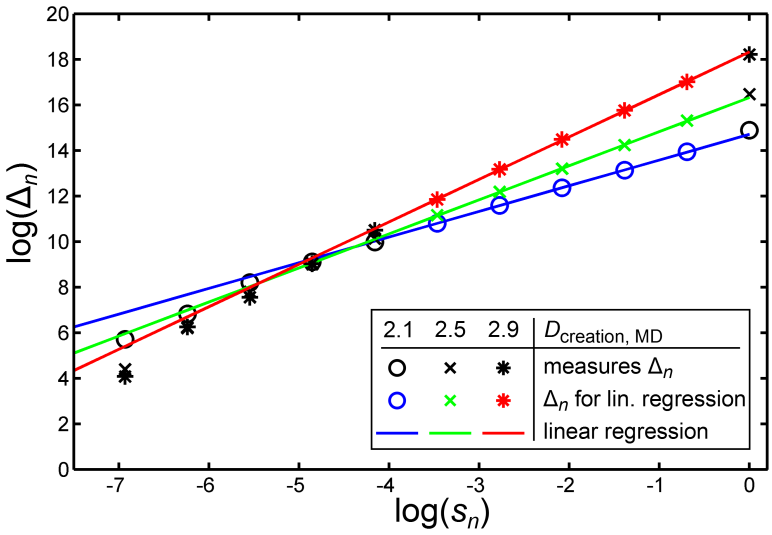

Figure A.19.: Exemplary log-log plot showing measures (Δ_n, scaling variable s_n) obtained with the PDM (nearest neighbour interpolation) for three different images (theoretical D-values: 2.1 (circles), 2.5 (crosses), and 2.9 (stars), created with MD, 2048×2048 pixels). Coloured markers indicate optimized scale-ranges that were used for fitting linear regressions (solid lines).

A.3. Comparison of Diagnoses

The following Tables A.20-A.28 show the correlations of the diagnoses between the human experts and the best automated methods for image sets IIa and IIb.

A.3.1. Image Set IIa

Table A.20.: Correlation of diagnoses of the 70 images of image set IIa showing different types of myocardial fibrosis, human expert 1 vs. human expert 2.

	Human Expert 1				
Human Expert 2	no fibrosis	interstitial	compact	diffuse	patchy
no fibrosis	9	1	0	1	0
interstitial	1	15	0	1	1
compact	0	0	13	0	0
diffuse	0	1	0	11	1
patchy	0	0	0	0	15

Table A.21.: Correlation of diagnoses of the 70 images of image set IIa showing different types of myocardial fibrosis, human expert 1 vs. automated classification (PDM,r_3,lin.thresholds).

Automated	Human Expert 1				
Diagnosis	no fibrosis	interstitial	compact	diffuse	patchy
no fibrosis	8	1	0	1	0
interstitial	2	10	0	0	0
compact	0	0	12	1	4
diffuse	0	3	0	7	0
patchy	0	3	1	4	13

Table A.22.: Correlation of diagnoses of the 70 images of image set IIa showing different types of myocardial fibrosis, human expert 2 vs. automated classification (PDM,r_3,lin.thresholds).

Automated	Human Expert 2				
Diagnosis	no fibrosis	interstitial	compact	diffuse	patchy
no fibrosis	10	0	0	0	0
interstitial	1	11	0	0	0
compact	0	0	12	1	4
diffuse	0	3	0	7	1
patchy	0	4	1	5	11

A.3.2. Image Set IIb

Table A.23.: Correlation of diagnoses of the 110 images of image set IIb showing different types of myocardial fibrosis, human expert 1 vs. human expert 2.

	Human Expert 1				
Human Expert 2	no fibrosis	interstitial	compact	diffuse	patchy
no fibrosis	13	3	0	0	2
interstitial	1	20	0	5	3
compact	0	0	25	0	0
diffuse	0	2	0	11	1
patchy	0	0	4	0	20

Table A.24.: Correlation of diagnoses of the 110 images of image set IIb showing different types of myocardial fibrosis, human expert 1 vs. human expert 3.

	Human Expert 1				
Human Expert 3	no fibrosis	interstitial	compact	diffuse	patchy
no fibrosis	8	0	0	0	0
interstitial	5	20	0	1	1
compact	0	0	28	0	2
diffuse	1	3	0	14	2
patchy	0	2	1	1	21

Table A.25.: Correlation of diagnoses of the 110 images of image set IIb showing different types of myocardial fibrosis, human expert 2 vs. human expert 3.

	Human Expert 2				
Human Expert 3	no fibrosis	interstitial	compact	diffuse	patchy
no fibrosis	8	0	0	0	0
interstitial	9	15	0	3	0
compact	0	0	24	0	6
diffuse	0	8	0	10	2
patchy	1	6	1	1	16

Table A.26.: Correlation of diagnoses of the 110 images of image set IIb showing different types of myocardial fibrosis, human expert 1 vs. automated classification (PGM,r_4,lin.thresholds).

Automated	Human Expert 1				
Diagnosis	no fibrosis	interstitial	compact	diffuse	patchy
no fibrosis	7	0	0	0	0
interstitial	6	21	0	2	4
compact	0	0	19	0	1
diffuse	1	2	2	11	3
patchy	0	2	8	3	18

Table A.27.: Correlation of diagnoses of the 110 images of image set IIb showing different types of myocardial fibrosis, human expert 2 vs. automated classification (PGM,r_4,lin.thresholds).

Automated	Human Expert 2				
Diagnosis	no fibrosis	interstitial	compact	diffuse	patchy
no fibrosis	7	0	0	0	0
interstitial	11	18	0	3	1
compact	0	0	19	0	1
diffuse	0	7	1	8	3
patchy	0	4	5	3	19

Table A.28.: Correlation of diagnoses of the 110 images of image set IIb showing different types of myocardial fibrosis, human expert 3 vs. automated classification (PGM,r_4,lin.thresholds).

Automated	Human Expert 3				
Diagnosis	no fibrosis	interstitial	compact	diffuse	patchy
no fibrosis	5	2	0	0	0
interstitial	3	23	0	4	3
compact	0	0	19	0	1
diffuse	0	1	2	13	3
patchy	0	1	9	3	18

"Pathological monsters! cried the terrified mathematician
Every one of them a splinter in my eye
I hate the Peano Space and the Koch Curve
I fear the Cantor Ternary Set
The Sierpinski Gasket makes me wanna cry
And a million miles away a butterfly flapped its wings
On a cold November day a man named Benoit Mandelbrot was born.
...
Mandelbrot Set, you're a Rorschach Test on fire
You're a day-glo pterodactyl
You're a heart-shaped box of springs and wire
You're one badass fucking fractal
And you're just in time to save the day
Sweeping all our fears away
You can change the world in a tiny way."

JONATHAN COULTON[157]